DETERMINATION OF FLAME CHARACTERISTICS IN A LOW SWIRL BURNER AT GAS TURBINE CONDITIONS THROUGH REACTION ZONE IMAGING

A Dissertation
Presented to
The Academic Faculty

by

Karthik Periagaram

In Partial Fulfillment
of the Requirements for the Degree
Doctor of Philosophy in the
School of Aerospace Engineering

Georgia Institute of Technology
December 2012

Determination of Flame Characteristics in a Low Swirl Burner at Gas Turbine Conditions through Reaction Zone Imaging

Approved by:

Dr. Jerry Seitzman, Advisor
School of Aerospace Engineering
Georgia Institute of Technology

Dr. Tim Lieuwen
School of Aerospace Engineering
Georgia Institute of Technology

Dr. Jeff Jagoda
School of Aerospace Engineering
Georgia Institute of Technology

Dr. Suresh Menon
School of Aerospace Engineering
Georgia Institute of Technology

Dr. Caroline Genzale
School of Mechanical Engineering
Georgia Institute of Technology

Date Approved: August 24, 2012

ACKNOWLEDGEMENTS

I acknowledge everyone's help. Thanks all.

TABLE OF CONTENTS

LIST OF FIGURES

LIST OF TABLES

LIST OF SYMBOLS

$\bar{c}$ Average velocity

$\bar{R}$ Universal gas constant

$\dot{m}$ Mass flow rate

A_{ij} Einstein coefficient for spontaneous emission from level i to level j

B_{ij} Einstein coefficient for stimulated absorption from level i to level j

c Speed of light in vacuum

d_s Outer diameter of the swirler

E_r Rotational energy

E_v Vibrational energy

f_i Boltzmann fraction of the population at energy level i

I Intensity of the laser beam

I_ν Spectral intensity of the laser beam

J Rotational quantum number

K Linearity constant in the turbulent flame speed model

k Boltzmann constant

L Integral length scale

Le Lewis number

M Mass flow ratio of the inner and outer regions of the swirler

m Mass

N'' Total rotational quantum number (of the lower level)

N Number of fluorescence emitters

n Number density of molecules

N_A Avogadro's number

P Power of the laser beam

p Combustor pressure

Q_{ij} Rate of collisional quenching of excited molecules from level i to level j

R Diameter ratio of the inner and outer sections of the swirler

Re Reynolds number

S Theoretical swirl number

S_L Laminar flame speed

S_T Turbulent flame speed

T Preheat temperature

U Mean local axial velocity of the reactants

u rms of the local axial velocity of the reactants

U_0 Reference velocity

V Volume

v Vibrational quantum number

W_{ij} Rate of pumping of molecules from level i to level j

X_0 Location of the virtual origin measured from the inlet

X_f Location of the flame standoff point measured from the inlet

X_i Mole fraction of species i

Y Fluorescence yield

α Swirler vane angle

$\Delta\nu_a$ Full Width at Half Max of the broadened absorption line

$\Delta\nu_c$ Collisionally-broadened Full Width at Half Max

$\Delta\nu_d$ Doppler-broadened Full Width at Half Max

$\Delta\nu_l$ Full Width at Half Max of the laser profile

δ_f Thickness of the flame

κ Strain rate

λ Wavelength

μ_i Reduced mass of species i

μ_{sig} Mean signal level

ν Wavenumber

ν_a Wavenumber of the absorption line

ν_l Center wavenumber of the laser profile

$\phi(\nu)$ Normalized lineshape of an absorption line

Φ Photon counts per second

ϕ Equivalence ratio

$\psi(\nu)$ Normalized lineshape of the laser beam

ρ Density

σ_a Line width of the broadened absorption line

σ_i Collisional quenching cross-section of species i

σ_l Linewidth of the laser

θ_f Angle of the flame cone measured from the combustor axis

SUMMARY

The Low Swirl Burner (LSB) is a promising combustion technology that is of importance to the gas turbine industry due to its potential for low NO_x emissions and robust flame stabilization. In order to effectively deploy the LSB in existing and future gas turbines, it is important to study its performance at high pressure, high preheat conditions. This thesis aims to quantify and explain the effect of parameters such as the combustor pressure and preheat temperature on the location and shape of the lifted LSB flame. Towards that goal, the work employs LDV for atmospheric pressure velocity field mapping and CH* chemiluminescence for high pressure flame imaging.

Supplementing the scope of chemiluminescence imaging, an improved implementation of CH PLIF has been investigated for studying the structure of hydrocarbon flames. The CH PLIF technique is demonstrated on a laminar Bunsen flame and on the LSB flame at atmospheric conditions. A four-level model of the fluorescing CH system is developed to predict the signal intensity in any hydrocarbon flame, over a wide range of pressures, temperatures and equivalence ratios. The model requires profiles of species concentrations and temperature across a flame to calculate the signal. This information is obtained from Chemkin simulations using the San Diego mechanism to solve for conditions across the flame surface. The results from imaging the atmospheric pressure laminar flame are used to validate the behavior of the signal intensity as predicted by the model. The model is further extended to explore the feasibility of using CH PLIF in several reacting mixtures, including ethane-air, propane-air and syngas-alkane-air mixtures.

The results from the LSB flame investigation reveal that combustor provides reasonably robust flame stabilization at low and moderate values of combustor pressure

and reference velocities. However, at very high velocities and pressures, the balance between the reactant velocity and the turbulent flame speed shifts in favor of the former resulting in the flame moving downstream. The extent of this movement is small, but indicates a tendency towards blow off at higher pressures and velocities that may be encountered in real world gas turbine applications. Another interesting observation from the experiments points to the increased tendency of relatively fuel-rich flames to behave like attached flames at high pressure. This is due to the enhanced strength of the outer/toroidal recirculation zone which enhances feedback of heat and reactants to the base of the flame at these conditions. These results raise interesting questions about turbulent combustion at high pressure as well as provide usable data to gas turbine combustor designers by highlighting potential problems.

The CH LIF model calculations show that the fluorescence signal is greatly reduced at high pressure due to the decreased number density of CH molecules and the increased collisional quenching rate. This restricts the use of this technique to increasingly narrow equivalence ratio ranges at high pressures. The limitation is somewhat alleviated by increasing the preheat temperature of the reactant mixture which enhances the CH concentration in the flame. The signal levels from methane-air flames are found to be comparable other alkane air flames. When applied to syngas-alkane-air mixtures, the signal levels from high hydrogen-content syngas mixtures doped with methane are found to be high enough to make CH PLIF a feasible diagnostic to study such flames. Finally, the model predicts that signal levels are unlikely to be significantly affected by the presence of strain in the flow field, as long as the flames are not close to extinction.

CHAPTER 1

INTRODUCTION

The need to reduce pollutant emissions, particularly the oxides of nitrogen, NO_x, is driven by increasing ecological awareness and stringent government regulations. This spurs efforts in the gas turbine industry to seek cleaner, more environment-friendly combustion concepts. Several mechanisms have been identified to explain the production of NO_x in hydrocarbon-air combustion systems. Of these, the thermal NO_x mechanism discovered by Zel'dovich, is a prominent source of NO_x production at the high temperature conditions encountered in typical combustors. The amount of thermal NO_x produced scales exponentially with the adiabatic flame temperature.

Efforts to reduce the flame temperature have led low NO_x gas turbine manufacturers to adopt one of two options—Lean Premixed (LP) operation, or Rich-Quench-Lean (RQL) operation. Of these, ground-based gas turbines used in power generation have tended to favor LP operation as it is conceptually simpler and avoids issues resulting from inhomogeneous mixing of fuel and air. Further, the ultra-lean operating conditions reduce flame temperature and minimize NO_x production.

In practice, 1800 K is considered a limiting value for the flame temperature, ensuring that the thermal NO_x production is constrained to a minimum.[1] Operating a combustor at such lean conditions results in weaker combustion processes that are highly susceptible to perturbations and results in combustor instabilities or even flame blow off. This highlights the requirement for robust flame stabilization techniques that can sustain combustion at ultra-lean conditions. In their most basic form, flame stabilization techniques work by making the local reactant velocity and the local flame speed equal. In the context of lean flames, the risk is of the slowly propagating flames to be blown off by the high velocity reactant stream. Consequently, flame

stabilization in gas turbine combustion is brought about either by reducing the local reactant velocity (e.g. by using bluff body flame holders), by boosting the local flame velocity (e.g. by enhancing product recirculation), or by providing continual ignition to the flame (e.g. by using pilot flames).

Swirl-stabilized combustion is a widely used flame stabilization technique in gas turbine applications.[2, 3] It primarily functions by inducing recirculation zones in the flow field that transport heat and radicals from the products into the reactants. This enhances the flame propagation velocity by increasing reaction rates within the flame, resulting in robust flame stabilization. However, the recirculation zones are associated with high peak residence times for hot combustion products and are sites of thermal NO_x production in the combustor. Nevertheless, swirl-stabilized combustors are ubiquitously employed today in land-based gas turbines used for power generation.

More recent research[4] on the Low Swirl Burner (LSB) has identified a potential solution for this problem. The LSB anchors a lifted flame, reducing the need for high swirl in the flow field. The lifted, V-shaped flame is stabilized by aerodynamic means which allows for robust operation even at low equivalence ratios. This weakens the recirculation zones and eliminates pockets of high residence times, resulting in the potential for significantly reduced NO_x emissions compared to a similar high-swirl design.

1.1 Motivation

By comparison to atmospheric pressure experiments, high pressure experimental testing of combustion systems is fraught with difficulties. This is reflected in the comparatively smaller subset of publications that report experimental results from high pressure tests. The primary source of these difficulties stems from the need for complicated testing facilities to reach and maintain high pressures. The inherently limited access afforded by pressure vessels makes intrusive methods of data gathering nearly

impossible. As a result, any need for spatially resolved data other than temperature and pressure measurements has to be met by optical diagnostics.

In the context of LSB research, these difficulties have confined much of the published experimental results to ambient conditions. The eventual application of this technology in gas turbine engines requires high quality data acquired at high pressure conditions. Ideally, such data will map the velocity field and heat release in the LSB and study their variation with flow conditions. Since the LSB relies on the velocity field to stabilize its flame, its flame characteristics hold information pertinent to both the velocity field and the heat release distribution within the combustor. This allows a passive diagnostic such as recording the flame chemiluminescence to be used even at high pressure conditions to observe and record usable data about the LSB flame characteristics. Such data, acquired at conditions closer to real world gas turbine combustor operating conditions is of particular interest to the gas turbine industry as it can be used for designing better, more robust combustors with low NO_x emissions.

The primary flame characteristic of interest is the flame standoff distance, defined as the distance from the flame stabilization point to the inlet of the LSB. This metric is useful is gauging the stability of the flame and the need for control systems to closely monitor its tendency to flashback or blow off. The standoff distance also relates to the heat load experienced by the injector and consequently affects how often the mechanical components of the LSB will require to be replaced in operation. Finally, a systemic variation in the location of the flame over a range of flow parameters may indicate potential problems operating the combustor at previously untested conditions.

Quantifying the shape of the flame can complement the information gleaned from the flame standoff measurements. In case of the V-shaped LSB flame, this can be conveniently obtained by measuring the angle of the flame cone. Changes in the flame angle affect the length of the flame, which is a design consideration for sizing LSB

combustors in gas turbines.

The profile of the flame chemiluminescence along the length of the combustion zone is representative of the local heat release at those locations. A uniform heat release profile is preferred so as to avoid thermally stressing the combustor at the hot spots. Further, since NO_x production rates are so strongly dependent on temperature, the heat release profile can help forecast emissions performance issues of the combustor, particularly when augmented by knowledge of the local flow velocity (and hence, residence time). Finally, the heat release map could be incorporated into n-τ models to predict the onset of thermo-acoustic instabilities in the combustor.

The primary goal of this research work is to study the flame characteristics of the LSB, such as its location and shape, as a means to learn more about the combustor operation at high pressure conditions.

In case of lean hydrocarbon flames, the primary sources of flame chemiluminescence are OH* ($A^2\Sigma^+ \to X^2\Pi$ bands, 310 nm), CH* ($A^2\Delta \to X^2\Pi$ bands, 430 nm, $B^2\Sigma^- \to X^2\Pi$ bands, 390 nm), C_2* ($d^3\Pi \to a^3\Pi$ Swan bands, 470 nm, 550 nm) and the CO_2* (band continuum, 320–500 nm). Of these, CH* chemiluminescence has several advantages that make it suitable for this particular study. First, collection of CH* chemiluminescence is less affected by blackbody radiation from the walls of the combustor, compared to longer wavelength emissions from a species like C_2*. Its narrow bandwidth allows one to use a bandpass filter to collect signals from only the wavelengths of interest, further minimizing interference from other light sources. Using such a narrow bandpass filter for a broad band emitter like CO_2* would result in rejecting most of the available signal. CH* chemiluminescence occurs in the visible wavelengths and does not require expensive UV lenses or imaging systems with high quantum efficiencies in UV to record it—as would be needed to image OH* chemiluminescence, for instance. In typical LSB operation, where the flame is not expected to operate near extinction, CH* chemiluminescence can serve as a reliable indicator

of heat release in the combustor. For all these reasons, CH* chemiluminescence is a suitable technique to image the LSB flame.

Ultimately, the amount of information that can be gathered by imaging the flame chemiluminescence is limited by its spatial resolution. Since chemiluminescence imaging is integrated over the line of sight, studying the flame brush or the flame structure is beyond its capabilities. A planar imaging technique such as Planar Laser-Induced Fluorescence (PLIF) is better suited for such applications.

In hydrocarbon flames, species accessible to PLIF are generally minor species in the flame. PLIF studies of hydrocarbon flames have hitherto focused on the hydroxyl, OH, radical. However, OH is produced in the flame zone and destroyed by relatively slow three-body reactions, causing it to persist and be transported away from the flame and into the product zone.[5] As a result, it does not serve as a direct marker of the flame front. Instead, the location of the flame is inferred from the sharp gradient in the OH signal as the reactants are converted into products.

The persistence of OH in the products makes OH PLIF somewhat less suited to studying flames in flows with high product recirculation. In such flows, the presence of OH in both the reactants and the products weakens the gradient at the flame. Further, since OH radicals could be transported transverse to the flame, its presence or absence serves as an unreliable indicator of local flame extinctions. Nevertheless, researchers have been able to use OH PLIF successfully[6, 7] to study such flames, particularly when the images are enhanced by nonlinear filtering techniques.[8, 9]

This study utilizes CH PLIF as the flame visualization technique. CH is produced and destroyed rapidly by fast two-body reactions, confining it to the thin heat release zone of the flame. This makes it suitable for use as a marker species for the flame front.[10] CH is formed during the breakup of hydrocarbon fuel molecules[11] and is also known to play an important role in the production of prompt NO_x.[12] Hence, it is a minor species of considerable importance to combustion research. This leads us

to the second motivation for this study—to examine the use of CH PLIF as a flame imaging technique in combustion systems and further, to use it to image and study the LSB flame.

The use of CH PLIF to study lean hydrocarbon flames has been difficult in the past due to several issues. First, the concentration of the CH species in hydrocarbon flames rapidly declines with equivalence ratio, making high quality imaging of the flame front at lean conditions challenging. Further, the implementation techniques in the past have suffered from a host of problems ranging from elastic scattering interference to saturation issues leading to diminished signal-to-noise ratios. However, a recent implementation by Li et al.[13] has managed to overcome these issues and has been demonstrated to image moderately lean flames with good fidelity.

Recent studies[14] have indicated that the formyl species, HCO, is a superior indicator of heat release in hydrocarbon flames when compared to CH or OH. The HCO LIF signal has been demonstrated to correlate well with the heat release rate, with little dependence on equivalence ratio or strain rate. The last factor, in particular, has been shown to quench the CH PLIF signal[15] in highly strained flames, even when the flame itself is not extinguished. Unfortunately, the signal levels from HCO LIF are very poor[14, 16] and are unsuitable for single-shot investigation of hydrocarbon flames. To overcome this, one study[16] proposed a simultaneous LIF investigation of formaldehyde, CH_2O, and OH with the reasoning that the formation rate of HCO is governed directly by the product of the concentration of these two intermediates. This method has been used in a number of investigations,[17] despite being experimentally cumbersome. A more recent implementation[18], published after the initiation of the present effort, has demonstrated single-shot HCO PLIF with moderate signal-to-noise ratios by utilizing a novel excitation scheme. Follow up studies applying this technique in other hydrocarbon flames are awaited. The current work, however, concerns itself primarily with the implementation of CH PLIF.

1.2 Literature Review

1.2.1 Low Swirl Burner

The LSB is a relatively new combustion technology and as such has a brief history. Initial interest in low swirl combustion was primarily motivated by its ability to stabilize a freely propagating turbulent flame.[19] As a result, initial designs of the LSB (which at the time used tangential jets to produce swirl) were pursued by Bédat and Cheng[4, 20] as test beds for studying 1-D, planar turbulent flames. Several subsequent studies[21–27] utilized this behavior and investigated fundamental turbulent flame structure and propagation in the jet LSB. Simultaneously, the discovery of its ability to achieve low NO_x emissions prompted interest in commercial applications of the LSB, such as in industrial furnaces and boilers.[28–30]

The current form of the LSB (as used in this thesis) using vanes to generate swirl was originally modified from a typical production swirl injector used in gas turbine combustors. The results of testing this new design were published by Johnson et al.[31] The design elements of the new injector—now called the Low Swirl Injector (LSI)—were tuned in an atmospheric pressure test rig using LBO and flame location as the criteria. The atmospheric tests were conducted with preheated reactants at up to 650 K. The more interesting results from the work came from high pressure, high preheat tests (15 atm, 700 K) in a test rig with limited optical access. The researchers measured a dramatic (50%) reduction in the NO_x emissions by switching from the original ("High" Swirl Injector) to the new low swirl design. The emissions performance was also noted by Nazeer et al.[32]

Subsequent studies by Cheng et al.[33,34] explored the characteristic velocity field in the LSB using PIV and discovered self-similar behavior that implied that the flame location was unaffected by the mass flow rate of the reactants. This led to further insights into the flame stabilization mechanism used by the LSB. These results will

be revisited in Chapter 2 in greater detail.

The effects of using an enclosure to contain the combustion zone were explored by Cheng et al.[35] who found scaling criteria for minimizing the effect of the enclosure on the flame stabilization location. More recent work has tended to focus on the use of various fuels such as hydrogen mixtures[36] with and without dilution[37], landfill gas[34, 38] and syngas[39].

Relatively little research has focused on the flame location and other characteristics and studied their variation at gas turbine relevant conditions. Plessing et al.[21] and Petersson et al.[40] have presented planar images of the LSB flame, but have been confined working with non-preheated, atmospheric flames at low flow rates. Of these, Plessing et al. used a jet-LSB design and imaged the resulting flame with OH Laser-Induced Pre-dissociative Fluorescence (LIPF) to calculate turbulent burning velocities. Petersson et al. studied a vane-LSB design that is slightly modified from the one tested by Cheng and co-workers and used a bevy of techniques, including OH PLIF to study the turbulent flame. The OH PLIF images were used to extract mean reaction progress variable contours for comparison to and validation of LES models. Although their test conditions and burner geometry were different, their results were consistent with the ones published by Cheng et al. These are notable for being some of the few works that afford us a look at the flame structure in the LSB with good spatial resolution.

1.2.2 CH PLIF Implementations

Historically, CH was the first species to be detected using LIF in a flame.[41] Early attempts[42, 43] to excite the CH layer used variations of short-pulsed, YAG-pumped dye laser output targeting transitions in one branch of the $A^2\Delta \leftarrow X^2\Pi$ (0,0) band and observing resulting fluorescence in the same band, but at a different rotational branch. These methods relied on the strong absorption of the $A-X$ bands to generate

high signal values, but suffered from interference from elastic scattering. Further, the short pulsewidth and narrow spectral bandwidths of the excitation sources quickly saturated the transition being pumped, limiting the amount of LIF signal measured.

Namazian et al.[44] and Schefer et al.[45] had better success at overcoming interference issues by exciting the $A - X$ (0,0) band, but observing fluorescence from the (0,1) band. Another similarly non-resonant technique was proposed by Paul et al.[46] who excited the $A^2\Delta \leftarrow X^2\Pi$ (1,0) band and observed resulting fluorescence from the (1,1) and (0,0) bands. These approaches provide good separation between the excitation and emission wavelengths, but are hampered by the spectroscopic properties of the CH system—which will be explored further in Section 2.2.2—which disfavor radiative transitions in the non-diagonal (0,1) or (1,0) bands. Further, Namazian et al.'s scheme suffers from interference due to Raman scattering of the excitation beam by the fuel species, which overlaps the (0,1) band fluorescence.

Carter and several others[47–55] pumped the $B^2\Sigma^- \leftarrow X^2\Pi$ (0,0) band and utilized fast electronic transfer from the $B^2\Sigma^-$, $v = 0$ to populate the $A^2\Delta$, $v = 0, 1$ levels. This way, they could observe the strong emission from $A^2\Delta \rightarrow X^2\Pi$ (1,1) and (0,0) bands. This method overcame the interference issues by providing sufficient spacing between the excitation and emission wavelengths, but suffered from saturation issues due to the short pulsewidth of the excitation sources. Further, at high laser irradiance, the group recorded noticeable interference from fuel LIF.

Li et al.[13, 56, 57] investigated the use of an alexandrite laser[58] to improve upon the previous excitation scheme by targeting the R-bandhead of the $B^2\Sigma^- \leftarrow X^2\Pi$ (0,0) transition with an excitation beam having a much longer pulse duration than Nd:YAG pumped dye lasers. This excitation scheme offers several advantages over previous implementations. First, it inherits the large spacing between the excitation and emission wavelengths and reduced interference issues from Carter et al.'s implementation. Next, by using a long pulsed laser beam, it overcomes saturation issues.

In fact, the researchers note that the pulsewidth is long enough to allow the same CH molecule to go through the excitation-deexcitation sequence several times, boosting signal output. This aspect of the implementation is further enhanced if the laser is operated in multi-mode, with a large spectral bandwidth, allowing the laser to target several lines near the R-bandhead. The resultant improvement in signal-to-noise makes this technique suitable to study even low equivalence ratio hydrocarbon flames. This is the excitation scheme that is used in this study.

1.3 Objectives and Overview

The main objectives of this thesis are summarized below.

1. The behavior of the LSB flame at gas turbine-like conditions will be investigated by studying its characteristics. The characteristics of interest include the flame location, shape and structure.

2. The LSB flame characteristics will be quantified and their dependence on flow parameters—combustor pressure, preheat temperature, reference velocity, equivalence ratio, and swirl—will be explored.

3. Models describing the flame stabilization processes in the LSB, derived based on earlier atmospheric pressure work, will be reexamined in the light of the above results.

4. Parallel to this, the development of a CH PLIF imaging system will be detailed. The CH PLIF imaging system is intended to be used to study the structure of lean hydrocarbon flames in preheated combustors, benefiting from the significantly improved spatial and temporal resolution capabilities of the technique as compared to chemiluminescence imaging.

5. The CH PLIF imaging system will be demonstrated on a laminar flame set up, as well as on the LSB.

6. The intensity of the CH LIF signal will be modeled to predict its variation with pressure, temperature, and reactant composition.

7. While the thesis retains its focus on methane-air combustion, the model will also be applied to mixtures of alkanes and syngases to examine the feasibility of studying such flames with CH PLIF.

The LSB investigation will extend our understanding of the physical processes responsible for LSB flame stabilization, while also aiding gas turbine combustor designers in designing more robust LSB configurations for use in future gas turbine engines. Simultaneously, the CH PLIF model developed in this thesis makes it possible to anticipate the CH LIF signal at various operating conditions, predicting the feasibility of using the technique to image the reaction zones at such conditions.

The first half of Chapter 2 provides a brief background discussing previously reported results from LSB investigations conducted by other researchers. The second half of the chapter discusses the CH PLIF process and explores simple and complex models for CH PLIF intensity. Details of the experimental facility and apparatus used to study the LSB and develop the CH PLIF imaging system are presented in Chapter 3. Chapter 4 presents the results and validation of the CH PLIF signal models developed in this theis. Chapter 5 presents results and discussion of the flame characteristics of the LSB acquired at high pressure conditions, along with flame structure images acquired at atmospheric conditions using CH PLIF. Finally, conclusions drawn from the discussions in Chapters 4–5 and suggestions for future work are presented in Chapter 6.

CHAPTER 2

BACKGROUND

This is a two-part chapter. The first section focuses on the LSB and discusses the current understanding of factors affecting the LSB reacting flow field. The second section explores efforts to model the CH PLIF signal intensity as a function of local composition and thermodynamic conditions in a flame.

2.1 LSB Reacting Flow Field

This section describes the salient features of the LSB flow field that will play an important part in the discussions to follow in this thesis. As discussed in Section 1.2.1, there have been multiple variations of the LSB design used by researchers in the past. Broadly, they can be classified into jet-LSB and vane-LSB, based on the means used to produce the weak swirl in the flow field. This thesis, and thus the following background material, focuses on the vane-LSB design.

The vane-LSB—or simply *LSB* from here on—uses a vaned swirler with a central open section. A typical design of such a swirler is shown in Figure 2.1. The swirler splits the flow into two streams, imparting swirl only to the outer annular flow. A perforated plate covers the open central section of the swirler and controls the relative mass flow split between the central unswirled flow and the annular swirling flow. The swirled flow and the central flow are allowed to mix after passing the swirler in a constant area nozzle. The length of this constant area nozzle is called the swirler recess length and is typically about one or two swirler (outer) diameters. The flow leaves the constant area nozzle and abruptly expands into the combustion zone.
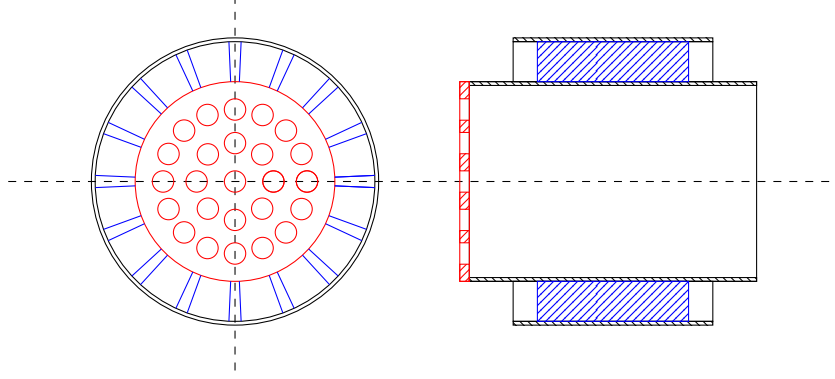
Figure 2.1: *The figure shows a bottom and side cross-sectional view of the vaned swirler design used in this study. The perforated plate used to control the relative mass flow split is highlighted in red, while the vanes used to generate swirl are highlighted in blue. The direction of flow in the side view is from the left to the right.*

2.1.1 Role of Swirl and Recirculation Zones

The amount of swirl present in the resulting flow is characterized by a theoretical swirl number, S, which represents the ratio of angular momentum to axial momentum in the flow field. Cheng et al.[29] and later, Littlejohn et al.[30] reduced this to the following equation.

$$S = \frac{2}{3} \tan \alpha \frac{1 - R^3}{1 - R^2 + \left[M^2 \left(\frac{1}{R^2} - 1 \right)^2 \right] R^2} \tag{2.1}$$

In Equation 2.1, R is the ratio of the diameter of the central section to the outer diameter of the swirler. Similarly, M is the ratio of the mass flow rate through the central portion to the mass flow rate through the outer (vaned) portion of the swirler. Finally, α is the angle of the vanes of the swirler.

Along with the recess length of the swirler, the theoretical swirl number was identified to be a key parameter that determines the LSB operating regime.[30] Typical values of S in low swirl combustion range from 0.4–0.6.

Figure 2.2 shows the locations of the notable recirculation zones in the LSB flow field. The toroidal recirculation zone (TRZ) forms near the inlet, while the central
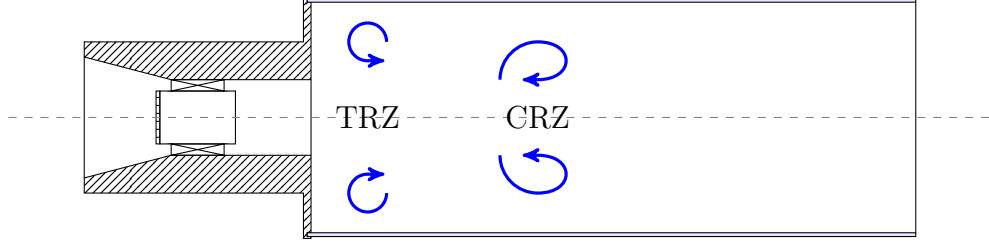
Figure 2.2: *The figure shows the locations of the recirculation zones in the LSB flow field. The Toroidal Recirculation Zone (TRZ) forms near the abrupt area expansion. The Central Recirculation Zone (CRZ) forms within a recirculation bubble along the centerline of the combustor.*

recirculation zone (CRZ) forms within a recirculation bubble along the centerline. In conventional swirl combustion, the function of the swirl is to induce these recirculation zones that help stabilize the flame by causing a feedback of heat and radicals from the products into the reactants. In particular, the toroidal recirculation zone traps hot combustion products and continually ignites the reactants at the base of the flame.[31]

In the LSB flow field, these recirculation zones are not only much weaker, but also, are not intended to play any part in the stabilization of the flame. Instead, the LSB flame is a freely propagating turbulent flame that is stabilized by the divergent flow coming from the inlet nozzle. The function of the swirl in the LSB flow field is merely to enhance this divergence. This purely aerodynamic means of stabilizing the flame differentiates the LSB regime from conventional swirl combustion.

2.1.2 Axial Velocity Profile and Self-Similarity

The mean axial velocity profile along the centerline of the LSB has been found[33, 34] to exhibit a characteristic linear profile in the near field of the inlet. Two parameters can be used to characterize this linear profile. First, extrapolating the velocity profile to the point upstream where the axial velocity equals the reference velocity, one can obtain the location of the virtual origin. The virtual origin represents the point upstream from which the divergence seemingly originates. The second parameter is the axial stretch rate, which is the slope of the linear region of the axial velocity

14

profile.

Cheng et al.[33,34] investigated these two parameters using a non-preheated setup at atmospheric pressure. They found that the virtual origin for reacting LSB flow fields asymptotically translates upstream at low/moderate Reynolds numbers, while the mean axial stretch rate, when normalized by the reference velocity, is nearly independent of the same parameter. This means that at moderately increasing Reynolds numbers, the divergent flow structure shifts upstream into the injector. This upstream shift ceases for high Reynolds numbers (above 70,000).

Since this shift does not affect the slope of the velocity profile, the researchers plotted the mean axial velocity profiles for different operating conditions, shifted to have a common virtual origin. Further, the velocity profiles were normalized by the mass-averaged inlet velocity (called the reference velocity). The resultant plot showed that the linear section of the divergent flow was self-similar at all the velocities tested. This self-similarity of the mean axial velocity profile was used to explain other observations regarding the flame characteristics, as described in the following sections.

2.1.3 Flame Stabilization Mechanism

The flame stabilization mechanism in the LSB is purely aerodynamic. The turbulent flame is not anchored in the sense of an attached flame, but freely propagates into the reactants. Conventionally, attached flames are preferred in combustion systems as lifted flames are associated with unstable/undesirable characteristics like blow off. However, previous studies[31] indicate the LSB flame is robustly stabilized and not prone to blow off.

The location where the LSB flame is stabilized is found from the equilibrium condition for flame stabilization—the local reactant velocity, U equals the local turbulent flame propagation velocity, S_T. In the LSB, the decrease in the local reactant velocity along the centerline of the combustor is accompanied by an increase in the local
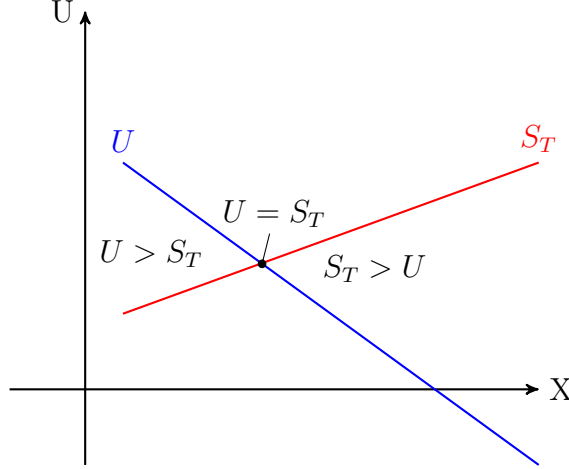
Figure 2.3: *The figure above illustrates the robustness of the LSB flame stabilization mechanism. The flame is stabilized at the point where the reactant velocity, U, and the turbulent flame speed, S_T, are equal. Perturbations to the flame standoff distance to the left or the right are counteracted by either U or S_T respectively making this a stable equilibrium.*

turbulence level. In other words, along the axis of the combustor, at the location where the flame is stabilized, the reactant velocity is decreasing, while the turbulent flame propagation velocity (which scales with the local turbulence) is increasing.

This sets up a stable equilibrium for the flame as shown in Figure 2.3. Small perturbations causing the flame to move upstream are offset by the increased reactant velocity, while similar perturbations downstream are counteracted by the increased turbulent flame speed. This is the mechanism behind the robust stabilization of the LSB flame.

2.1.4 Effect of Flow Parameters on Flame Characteristics

The operating conditions of the LSB combustor are fully described by four fundamental flow parameters; the combustor pressure, p, the combustor temperature, T, the mixture equivalence ratio, ϕ, and the reference velocity, U_0. The reference velocity represents the mass-averaged velocity of the reactants entering the LSB and is defined after Cheng et al.[29] as a function of several variables such as the mass flow rates of the air and fuel, $\dot{m}$, their densities at the swirler, ρ and the area of the swirler

calculated from its outer diameter, d_s.

$$U_0 = \frac{\left(\dfrac{\dot{m}_{air}}{\rho_{air}}\right) + \left(\dfrac{\dot{m}_{fuel}}{\rho_{fuel}}\right)}{\dfrac{\pi d_s^2}{4}} \qquad (2.2)$$

In this section, we will briefly discuss the effect of flow parameters have on the flame characteristics of interest. By way of an example, and as a means to introduce a few basic concepts, the following discussion will examine the effect of increasing the reference velocity on the flame location, shape and structure. In-depth discussion of the dependence of each flame characteristic on all the flow parameters of interest will be deferred until Chapter 5.

2.1.4.1 Effect on Flame Standoff Distance

As described earlier in Section 2.1.3, the LSB flame is stabilized where the local reactant velocity and turbulent flame speed are equal. Unlike the laminar flame speed, S_L, the turbulent flame speed is not uniquely determined by the reactant composition and thermodynamic conditions. Instead, it is a function of the flow characteristics and the burner geometry.

A simple model proposed by Damköhler[59] treats the turbulent flame as a wrinkled laminar flame. The presence of these wrinkles vastly increases the surface area of the flame, increasing the rate at which the reactants can be consumed through the flame. The size of these wrinkles can be related to the rms of the local reactant velocity, u. Expressed mathematically, this leads to Equation 2.3.

$$\frac{S_T}{S_L} = 1 + \frac{u}{S_L} \qquad (2.3)$$

Cheng et al.[23, 38, 39] observed that the slope of this linear relationship was dependent on the fuel mixture being used. This idea is encapsulated in Equation 2.4

that presents a modified version of Equation 2.3.

$$\frac{S_T}{S_L} = 1 + K\frac{u}{S_L} \tag{2.4}$$

The constant K has a value of around 1.73 for methane-air mixtures and a somewhat higher value—3.15—for hydrogen-air mixtures,[38] suggesting that the turbulent flame speed is affected strongly by the thermo-diffusive properties of the fuel.

In order to predict the expected effect of increasing the reference velocity, consider the following analysis at the flame standoff location where $U=S_T$.

$$\frac{S_T}{S_L} = 1 + K\frac{u}{S_L}$$

$$S_T = S_L + Ku$$

$$\implies U = S_L + Ku$$

$$U_0 - \frac{dU}{dx}(X_f - X_0) = S_L + Ku$$

$$\therefore X_f = X_0 + \frac{1 - \left(\dfrac{S_L}{U_0} + K\dfrac{u}{U_0}\right)}{\dfrac{1}{U_0}\dfrac{dU}{dx}} \tag{2.5}$$

Consider the terms on the RHS of Equation 2.5. As described in Section 2.1.2, the virtual origin location is invariant for moderate to high values of reference velocity. In the same section, the normalized slope of the velocity profile, $\frac{1}{U_0}\frac{dU}{dx}$, was also noted as being invariant with reference velocity. In the numerator of the second term, the local turbulence intensity, $\frac{u}{U_0}$, can also be expected to be a constant, since u should scale with the reference velocity in the same manner as long as the burner geometry does not change. The turbulence intensity, $\frac{u}{U_0}$ in the LSB increases from the inlet along the centerline reaching values on the order of 0.1–1.0 near the flame standoff location.[34] That leaves only the term $\frac{S_L}{U_0}$ as a function of U_0. Typically, the laminar

18

flame speeds are at least an order of magnitude, if not more, lower ($\approx O(0.1)$ m/s) than the reference velocities at which the LSBs are operated ($\approx O(10)$ m/s). Only at high values of preheat does the laminar flame speed for methane-air mixtures reach $O(1)$ m/s. Over most of the operating conditions, this term and any variation in its value are a vanishingly small portion of the sum, leaving the entire RHS independent of U_0. In other words, the flame location, X_f is expected to be invariant with the reference velocity at which the LSB is operated.

2.1.4.2 Effect on Flame Shape

Now, consider the effect of increasing the reference velocity on the angle of the flame cone. Again, the stabilization condition is equality between the local velocity and the turbulent flame speed. However, along the flame cone, the reactant velocities are much higher and the flame propagation can only occur at an angle to the reactant velocity. Increasing the reference velocity does not affect any of these factors and thus, the flame angle can also be expected to be unchanged at higher reference velocities.

2.1.4.3 Effect on Flame Structure

Finally, the effect of the reference velocity on the structure of the turbulent flame should be considered. Depending on the characteristics of the flame structure, the operation point can be placed on a Borghi diagram, as shown in Figure 2.4. The Borghi diagram[60] is a phase diagram used to classify and delineate regimes of pre-mixed turbulent combustion. The double-log plot is drawn using properties of the reacting mixture and its turbulence-related quantities. It is partitioned into various regimes by different straight lines representing the locus of non-dimensional parameters. It is useful to examine the effect of various parameters on the flame structure by examining the tendency of the operating point to shift on the Borghi diagram.

Several versions of the Borghi diagram exist that use different variables to plot
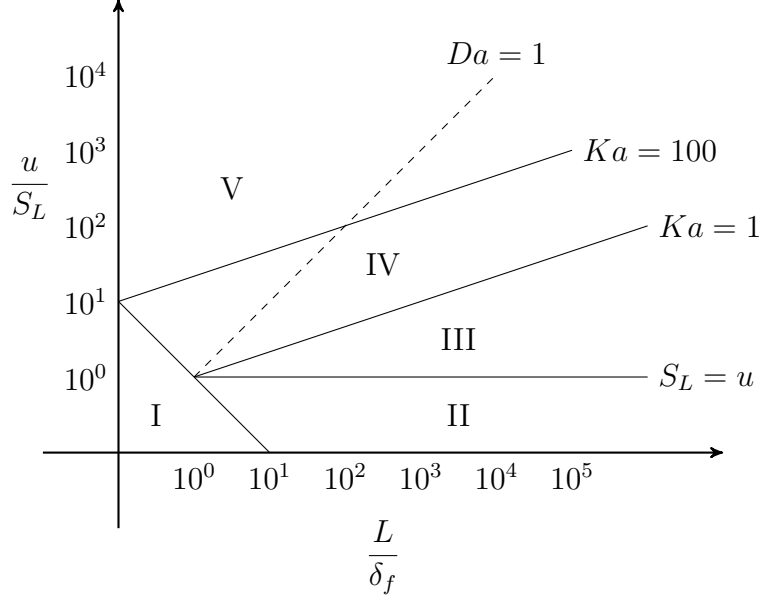
Figure 2.4: *The figure shows the Borghi diagram marking the various regimes of premixed turbulent combustion—I. laminar flames, II. wrinkled flamelets, III. corrugated flamelets, IV. thin flame zones, and V. broken reaction zones—separated by contours of Karlovitz number.*

the combustion regimes. In the current study, we use a diagram based on $\dfrac{u}{S_L}$ and $\dfrac{L}{\delta_f}$. The key parameters to be considered here are the rms velocity, u, the laminar flame speed, S_L, the integral length scale of the flow, L, and the flame thickness, δ_f.

Increasing the reference velocity will be accompanied with a concomitant increase in the level of turbulence in the flow, but it changes none of the other parameters. As a result, the operating point will traverse vertically on the Borghi diagram. If the LSB operates in the wrinkled flamelets regime to begin with, at very high reference velocities, it may be expected to cross over into the corrugated flamelets regime. This will be marked by the formation of holes and pockets in the flame sheet.

2.2 CH PLIF Signal Modeling

While the intent and scope of this work is to use CH PLIF as a visualization technique to image the flame front with high fidelity, it would be extremely useful to be able

to predict the CH PLIF signal intensity for different reactant mixtures and initial conditions as a means to gauge the feasibility of applying the technique to acquire high fidelity images of the flame at those conditions. To that end, this discussion will attempt to develop a mathematical model to calculate, in a semi-quantitative manner, the rate of CH PLIF photons emitted by the illuminated reaction zone. The following discussion introduces important concepts in LIF signal intensity calculation using a simple two-level model and then proceeds to apply these concepts to model the more complicated physical processes in the CH system.

2.2.1 Basic Model

In its most basic form, the rate at which fluorescence photons are generated in a system, Φ is the product of the number of emitters, N and the Einstein coefficient for spontaneous emission, A.

$$\Phi = N \times A \tag{2.6}$$

The fluorescence photons produced are radiated in all directions and only a fraction of these can be recorded by a collection system in an experiment. This fraction is determined by the experimental set up, the collection angle, and the efficiency of the optics and the detector used to record the signal. For this analysis, however, this fraction is omitted to reduce complexity.

In a simple two-level model for the fluorescing system, as shown in Figure 2.5, Equation 2.6 may be expanded in terms of the number density of the emitters, n, and the volume in which the fluorescence occurs, V.

$$\Phi = n_1 V A_{10} \tag{2.7}$$

The population of the upper state, n_1 can be solved for by rate analysis. The

21
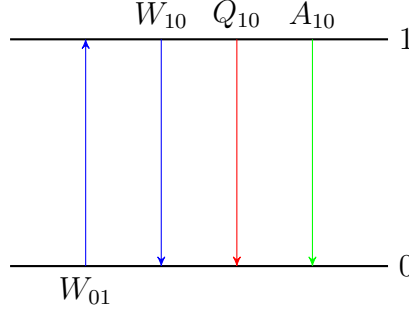
Figure 2.5: *The figure shows energy levels and transitions between two levels, labeled 0 and 1, in a basic model of laser-induced fluorescence. Stimulated absorption and emission are shown in blue, collisional quenching is shown in red and spontaneous emission is shown in green.*

mathematical treatment is not particularly complicated and is covered in detail by various textbooks and review papers.[61, 62] Here, we shall merely remark that the functional form of the solution has two limiting cases. The limits are decided by the relative magnitudes of the pumping rate, W_{01}, which depends on the laser intensity and the radiative transition probability, and the relaxation rate in the absence of an external field, which is given by the sum of the spontaneous emission and collisional quenching rate, $A_{10} + Q_{10}$. The pumping rate is the rate at which the upper energy level is populated through stimulated absorption from the lower level. The relaxation of the molecules to the lower energy state occurs either through spontaneous emission of a photon or energy transfer to other molecules through inelastic collisions.

When the pumping rate is far lower compared to the relaxation processes ($W_{01} \ll A_{10} + Q_{10}$), the solution tends to the weak excitation limit. In this limit, the functional form of the solution is shown in Equation 2.8

$$\Phi = n_0 V W_{01} \overbrace{\frac{A_{10}}{A_{10} + Q_{10}}}^{\text{Fluorescence Yield}} \tag{2.8}$$

The $n_0 V W_{01}$ term in Equation 2.8 represents the number of molecules that are excited to the upper state per second, while the fluorescence yield represents the fraction of these molecules that will produce a LIF signal. In typical combustion

22

environments, the fluorescence yield is usually small, since the collisional quenching rate dominates the spontaneous emission rate. The rate of collisional quenching of the fluorescing species by another species in the flame is proportional to the frequency of collisions between the two. Further, the effectiveness of such collisions is decided by a collision cross-section, σ, which is often a function of the temperature. Equation 2.9 presents the calculation of the collisional quenching rate by summation over all the species, i, in the flame.

$$
\begin{aligned}
Q_{10} &= \sum_i n_i \times \sigma_i \times \bar{c}_i \\
&= \sum_i n_i \sigma_i \sqrt{\frac{8kT}{\pi \mu_i}} \\
&= \sqrt{\frac{8kT}{\pi}} \sum_i \frac{n_i \sigma_i}{\sqrt{\mu_i}}
\end{aligned}
\tag{2.9}
$$

In Equation 2.9, k is the Boltzmann constant, T is the local temperature, n_i is the number density of species i and μ_i represents the reduced mass of the colliding molecules, given by Equation 2.10.

$$
\mu_i = \frac{m_i m}{m_i + m}
\tag{2.10}
$$

In Equation 2.10, m is the mass of the marker species, while m_i are the masses of the colliding species. Since LIF in combustion primarily targets minor species, by probability, these collisions will almost always occur with major species in the system. As a result, the summation in Equation 2.9 need only be carried out over the major species in the flame. The values of the local number densities of the major species can be measured by techniques like Raman scattering, or can be obtained from solving chemical kinetics models.

2.2.1.1 Absorption Integral Calculation

Let us now briefly examine the first term in Equation 2.8 in further detail. Let $\phi(\nu)$ represent the normalized lineshape of the absorption line being excited, such that $\int \phi(\nu)d\nu = 1$. If B_{01} is the Einstein coefficient for absorption for the line being excited, the term $B_{01}\phi(\nu)$ represents the spectral absorptivity of the line at ν. B_{01} is usually presented in m^2/Js for LIF applications. Similarly, let I_ν be the spectral intensity of the incident radiation, which is the intensity (power per area) of the laser beam per spectral interval. Let $\psi(\nu)$ be the normalized spectral profile of the laser lineshape, such that $I_\nu = I\psi(\nu)$ and $\int \psi(\nu)d\nu = 1$. I_ν is usually given in $W/cm^2/cm^{-1}$ for ease of use in laser applications.

The product of the spectral absorptivity and the spectral intensity integrated over the spectrum, gives the pumping rate, W_{01}, as shown in Equation 2.11. The factor c is the speed of light, which brings the units of W_{01} to s^{-1}.

$$W_{01} = \frac{I}{c} \int \psi(\nu)B_{01}\phi(\nu)d\nu \tag{2.11}$$

2.2.1.2 Population Distribution

Once again, consider Equation 2.8, this time focusing on the term n_0, the number density of the marker species in the lower energy state that are available for excitation to the upper state. In reality, this comprises only a small subset of all the available molecules of the marker species in the system.

$$n_0 = nf_0 \tag{2.12}$$

In Equation 2.12, n is the number density of all marker species over all the energy levels, while the fraction, f_0, represents the proportion of the marker species that populates the lower energy level.

2.2.1.3 Solution

Substituting Equations 2.11 and 2.12 into 2.8, and noting that the signal produced is actually integrated over a volume,

$$\Phi = \int_V \frac{nA_{10}}{A_{10}+Q_{10}} \frac{I}{c} f_0 B_{01} \int_\nu \psi(\nu)\phi_j(\nu)d\nu dV \qquad (2.13)$$

In Equation 2.13, the absorption integral from Equation 2.11 is highlighted in red. The outer integral is performed in space, over the portion of the flame illuminated by the laser sheet. Under the assumption that the laser intensity is uniformly distributed over the sheet thickness, it is possible to rewrite the outer integral as a 1-D integral over the thickness of the flame by replacing the laser intensity, I with the laser power, P. Strictly speaking, this is not the flame thickness, but the thickness of the fluorescing CH layer in the flame.

$$\Phi = \frac{P}{c} \int_x \frac{nA_{10}}{A_{10}+Q_{10}} f_0 B_{01} \int_\nu \psi(\nu)\phi_j(\nu)d\nu dx \qquad (2.14)$$

Equation 2.14 is thus, the solution to the two-level model in the weak excitation limit. Note that the LIF signal varies linearly as the incident laser power (or intensity). Consequently, the weak excitation limit is also referred to as the linear regime.

For the sake of completion, we will briefly mention the other limit of the two-level model solution that occurs when the rate of pumping far exceeds the relaxation rate ($W_{01} \gg A_{10} + Q_{10}$). This is called the saturated limit and in this limit, the fluorescence signal ceases to change with the intensity of the incident laser beam. Operating in this regime has one major advantage for quantitative LIF measurements; the measured fluorescence signal is nearly independent of the collisional quenching rate, a parameter that can change significantly throughout the combustion. However, there are several drawbacks to operating in this regime. First, the magnitude of the LIF signal per unit incident laser intensity tends to be the maximum in the linear regime.

Once the variation ceases to be linear (even before nearing the saturation limit), we get diminishing returns for increasing the laser power. For measurements with low signal-to-noise ratio, which is often the case for PLIF imaging, this is a significant drawback. Further, the saturation criterion (maintaining a high laser intensity) is difficult to satisfy simultaneously in the spatial, temporal and spectral domains. For these reasons, we will restrict our discussion hence forward the linear regime only.

2.2.2 CH PLIF Process

In this section, we will examine the limitations of trying to apply the two-level model to describe the CH PLIF process.

Laser-Induced Fluorescence is a multi-step process. First, the marker species absorbs a photon and transitions from a lower energy state to a higher one. This is followed by several physical processes, of which only one pathway leads to the spontaneous de-excitation of the excited molecule, accompanied by the release of a photon. The de-excitation can—but does not need to—take the molecule back to the original state. If the molecule does return to its original state, the fluorescence is said to be resonant. Due to the difficulty of measuring fluorescence signals at the same wavelength as the excitation beam, most practical applications of LIF tend to be non-resonant. The choice of the spectral and temporal properties of the excitation laser source, and of the detected fluorescence emission, constitute the excitation and detection schemes.

The excitation scheme chosen for this study follows the work done by Li et al.[13] who used a ring-cavity, pulsed alexandrite laser to provide excitation in the vicinity of the R-bandhead of the CH $B^2\Sigma^- \leftarrow X^2\Pi$ (0,0) system. This bandhead, shown in Figure 2.6, is found at a frequency of about 25824 cm^{-1} (or a wavelength of about 387.2 nm) and represents transitions from a ground state rotational quantum number of $N'' = 7$. When operated in multimode, alexandrite lasers have relatively large
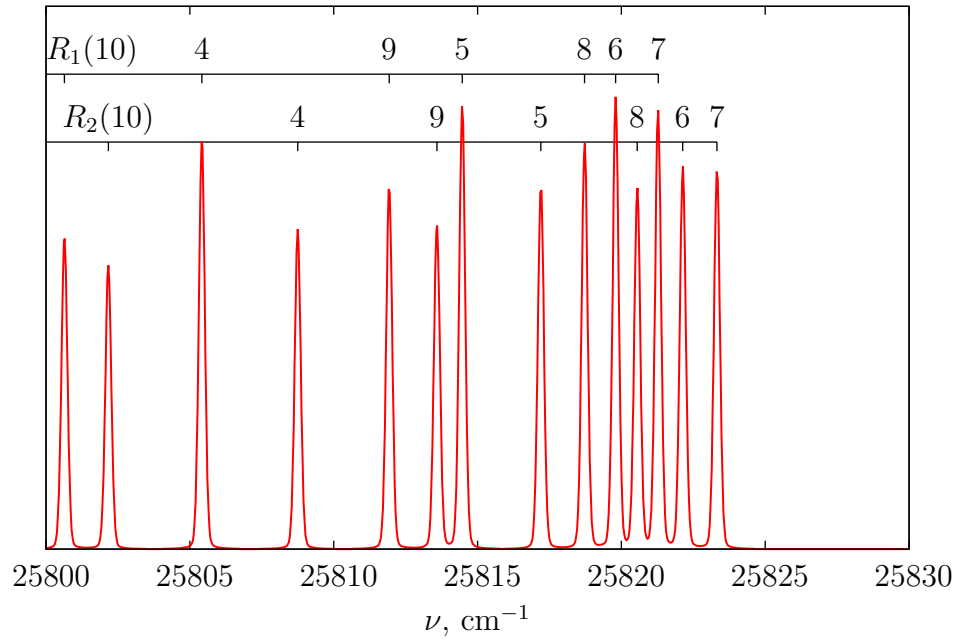
Figure 2.6: *The figure shows the frequencies of the absorption lines near the R-bandhead of the CH $B^2\Sigma^- \leftarrow X^2\Pi$ (0,0) band. The individual lines are labeled with corresponding N'' quantum number.*

bandwidths (a few cm^{-1} is not uncommon) and hence make it possible to excite several of the neighboring transitions near the bandhead.

Upon excitation, these molecules transition to the second electronically excited $B^2\Sigma^-$ state and populate the lowest vibrational level, ($v' = 0$). At this point, the following possibilities exist for the excited molecule:

1. The molecule can undergo inelastic collisions with other molecules, resulting in relaxation in the rotational, vibrational or electronic manifolds.

2. The molecule can spontaneously emit a photon and return to any of the lower energy states.

3. The molecule can experience stimulated emission in the presence of another photon of the appropriate frequency and return to any of the lower energy states.

4. The molecule can experience further excitation either by absorbing a photon or through collisional means and can react chemically.

Now, let us examine these potential pathways in greater detail. The first pathway pertains to relaxation. The excitation and subsequent population of a higher energy state causes the CH population distribution to deviate from the equilibrium Boltzmann distribution. The degree of relaxation possible is limited by the lifetime of the energy level the excited species occupy. The maximum time possible for relaxation is given by the collision-free, radiative lifetime of the B electronic state, which is about 300 ns[63]—long enough for sufficient rotational relaxation to occur, but too short for complete vibrational relaxation. Based on experiments conducted by Garland et al.[64], it is estimated that the vibrational energy transfer between the two bound states available to the $B^2\Sigma^-$ state is about two orders of magnitude slower than the rotational energy transfer. As a result, we may suppose that the vibrational manifold remains relatively unaffected, while the rotational manifold can partially relax toward an equilibrium distribution. The question of the electronic relaxation will be addressed later in this discussion.

The second option available for the excited CH molecule is to spontaneously emit a photon and return to a lower energy state. Spontaneous de-excitation to the ground state primarily follows the diagonal $B^2\Sigma^- \rightarrow X^2\Pi$ (0,0) band. The rate of such spontaneous emission between two states is given by the Einstein emission coefficient for the transition. Once again, we will defer discussion of the $B - A$ transition until later in this discussion.

The third option is for the CH molecule to experience stimulated emission in the presence of a photon of an appropriate frequency. It is highly unlikely that the apposite photon would have a frequency other than the excitation laser. The rate of stimulated emission induced by the excitation laser beam is proportional to the Einstein absorption coefficient for the transition. Other photons that can induce

stimulated emission could originate from spontaneous emission or CH* chemilumi-nescence, however they would be negligible in intensity compared to the laser.

The fourth option is for the molecule to experience further excitation by absorbing multiple photons or through collisions with other energetic molecules in the system. Since most available photons do not match any transitions from the $B^2\Sigma^-$, $v = 0$ state, it is unlikely to experience multi-photon excitation. However, collisional removal of CH molecules from the B state is certainly possible.

Having listed all the options, let us resume the discussion on the possibility of electronic energy transfer from the excited $B^2\Sigma^-$, $v' = 0$ state. The spacing of the energy levels in the CH system, shown in Figure 2.7, is such that the $B^2\Sigma^-$, $v' = 0$ state is found to be near-degenerate with the $A^2\Delta$, $v = 1$ energy level. Consequently, the $B^2\Sigma^- \leftrightarrow A^2\Delta$ (0,1) transition is reversible. Due to this, collisional population of the $A^2\Delta$ $v = 0, 1$ states from the $B^2\Sigma^-$ $v = 0$ state occurs rapidly. Garland et al.[64] measured that these transfers account for almost a quarter of all collisional depletion of the $B^2\Sigma^-$, $v = 0$ level. Theoretical calculations using overlap integrals between the involved energy levels predict that a majority of these transfers will be along the diagonal (0,0) transition.[65]. Instead, experimental data indicates that the number is closer to a fifth, with almost 80% of the transfers following the near-degenerate (0,1) pathway.

It is this electronic energy transfer mechanism that enables our excitation scheme to record high quality CH PLIF images. Having now populated the $A^2\Delta$ states, the resulting spontaneous emission from the $A^2\Delta \rightarrow X^2\Pi$ (0,0) and (1,1) transitions can be easily observed between 420–440 nm. A small portion of the fluorescence in this wavelength range also occurs from the $B^2\Sigma^- \rightarrow X^2\Pi$, (0,1) transition. Since these emission wavelengths are located far from the excitation wavelength, a simple glass filter is sufficient to suppress any elastic scattering from the laser beam.
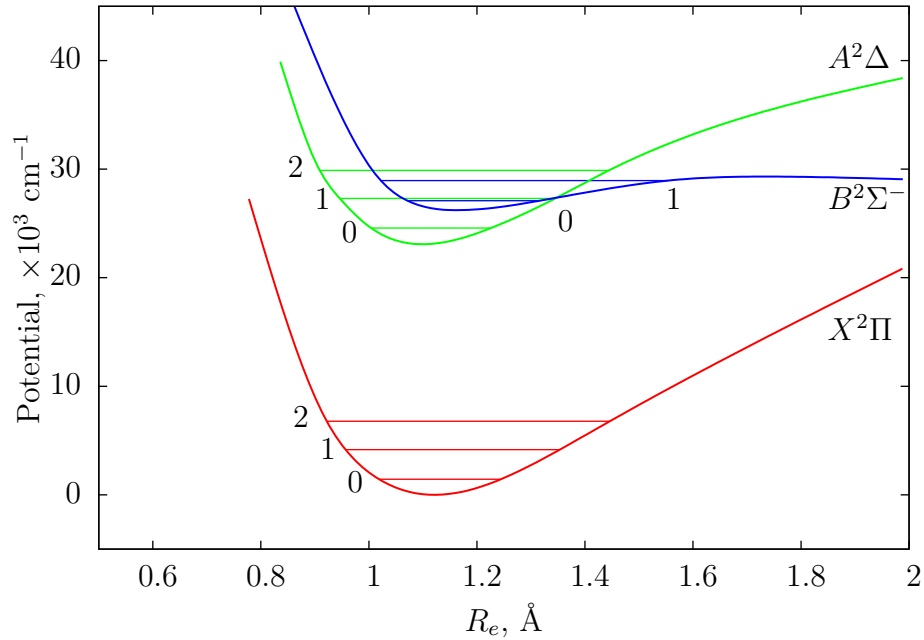
Figure 2.7: *The figure shows the RKR potential curves for the $X^2\Pi$, $A^2\Delta$ and $B^2\Sigma^-$ energy levels in the CH system. A few vibrational levels are indicated for the $X^2\Pi$ and $A^2\Delta$ states. The $B^2\Sigma^-$ state has only two bound vibrational levels. The diagram is reproduced from Richmond et al.[66] who based it on* ab initio *calculations by van Dishoeck[67]*

2.2.3 Improved Model

While the two-level model is conceptually simple, applying it to describe the complicated physical process of CH PLIF is challenging. Daily[62] notes, for example, that significant errors can result from using the two-level model to describe even a three-level system. Hence, it is worthwhile to investigate a more complicated model that can describe the CH system with higher fidelity.

Figure 2.8 shows the relevant pathways that lead to the fluorescence emission as discussed in Section 2.2.2. An accurate model of the CH system should involve at least five energy levels, namely the $B^2\Sigma^-$, $v = 0$, $A^2\Delta$, $v = 0, 1$, and $X^2\Pi$, $v = 0, 1$ levels. The model will need to account for collisional transfers between each of these levels, in addition to spontaneous and stimulated transitions. By limiting the model to five levels, we are assuming that the distributions within the rotational manifolds associated with each vibrational level do not play a significant role in altering the net

Figure 2.8: *Some of the important transitions between energy levels in a CH molecule are shown. The excitation of the CH molecules (blue) is followed by collisional energy transfer processes (red) which populate additional energy levels. Spontaneous emission from some of these energy levels (green) is collected.*

rate of transfer between vibration levels. Even for just five levels, the mathematical solution quickly becomes tedious and complicated. Further, it involves several rate coefficients that have not yet been measured experimentally.

Fortunately, this can be significantly simplified. Previous studies[63, 65] have indicated that the off-diagonal $B \rightarrow X$ (0,1) transition plays a relatively minor role accounting for only 3.5% of the total fluorescence. Further, the radiative $A \rightarrow X$ transitions are known[68] to be strongly diagonal, with little or no interaction[64] between the two states. The net result of these two assertions is that we can treat the two $B \rightarrow A \rightarrow X$ pathways to be disjoint and parallel. The resulting model involving four energy levels is shown in Figure 2.9.

According to this model, the lower state of the CH system is treated as a single pool from which CH molecules are excited from or de-excited to. This not only neglects the rotational manifold, but also the vibrational manifold of the ground state. This assumption would be valid as long as most of the CH molecules occupy the $v = 0$ state and the fraction of molecules in the $v = 1$ state can be safely neglected. At flame temperatures of about 2200 K, this assumption is somewhat questionable as only about 83% of the ground state CH molecules occupy the $v = 0$ level and as much
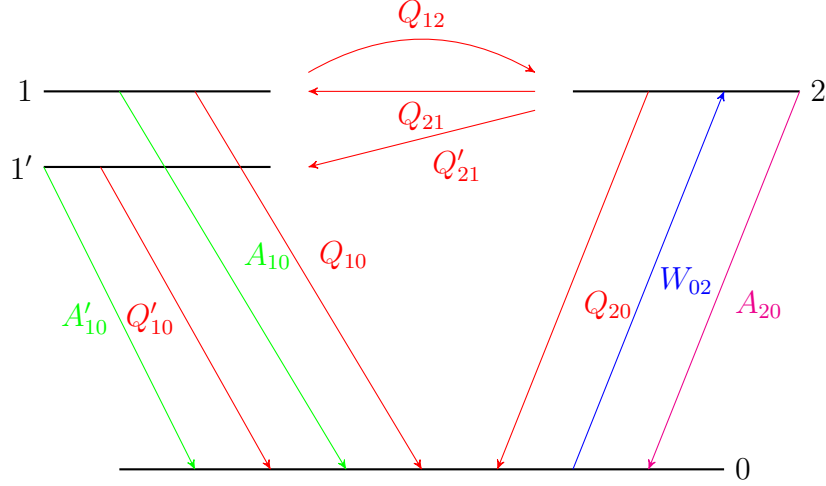
Figure 2.9: *A simplified model of the transitions between the energy levels in a CH system. Excitation (blue) of ground state CH molecules to the upper electronic state is followed by several collisional energy transfer processes (red). A small portion of these molecules spontaneously emit a photon (green) and return to ground state. The spontaneous emission corresponding to resonant PLIF (magenta) is not collected.*

as 14% are found at the $v = 1$ state. However, in light of the simplifications afforded to our semi-quantitative model by this assumption, we retain it.

The rates of the various transition processes are indicated in Figure 2.9. W_{02} is the pumping process that populates the $B(0)$ state. Q_{ij} are collisional energy transfer processes that transfer CH molecules from the i level to the j level. The subscripts 0, 1 and 2 represent the electronic energy levels X, A and B. Processes involving the $A(v = 0)$ state are differentiated from those involving the $A(v = 1)$ state by a prime ($'$). Finally, A_{ij} represents the spontaneous emission coefficients between the i and j levels.

Applying Equation 2.6 to this case, we can write an expression for the LIF signal intensity as follows,

$$\Phi = (n_1 A_{10} + n'_1 A'_{10})V \tag{2.15}$$

Our task is to solve for the values of n_1 and n'_1 in terms of n_0. To do this we need to write rate equations describing the variation of the populations of the three upper

states with time.

$$\frac{dn_1}{dt} = -(A_{10} + Q_{10} + Q_{12})n_1 + Q_{21}n_2 \tag{2.16}$$

$$\frac{dn_1'}{dt} = -(A_{10}' + Q_{10}')n_1' + Q_{21}'n_2 \tag{2.17}$$

$$\frac{dn_2}{dt} = W_{02}n_0 + Q_{12}n_1 - (A_{20} + Q_{20} + Q_{21} + Q_{21}')n_2 \tag{2.18}$$

Under the assumption that the laser excitation time scale is much longer that the collisional time scales, we can set the LHS of Equations 2.16–2.18 to zero. This results in a closed set of linear equations, which can be expressed in matrix form as follows.

$$\begin{bmatrix} A_{10} + Q_{10} + Q_{12} & 0 & -Q_{21} \\ 0 & A_{10}' + Q_{10}' & -Q_{21}' \\ -Q_{12} & 0 & A_{20} + Q_{20} + Q_{21} + Q_{21}' \end{bmatrix} \begin{bmatrix} n_1 \\ n_1' \\ n_2 \end{bmatrix} = \begin{bmatrix} 0 \\ 0 \\ W_{02}n_0 \end{bmatrix} \tag{2.19}$$

>From Equation 2.19, we only need the solutions to n_1 and n_1'. Substituting the solutions directly into Equation 2.15, we can write the solution in the following form to mirror the expression in Equation 2.8.

$$\Phi = n_0 V W_{02}(Y + Y') \tag{2.20}$$

The terms Y and Y' in Equation 2.20 are non-dimensional and represent the fluorescence yields from the two $A^2\Delta$ states. The functional expression for the yields is more complex now, as shown in Equations 2.21–2.22.

$$Y = \frac{Q_{21}A_{10}}{(A_{10} + Q_{10} + Q_{12})(A_{20} + Q_{20} + Q_{21} + Q'_{21}) - Q_{12}Q_{21}} \tag{2.21}$$

$$Y' = \frac{(A_{10} + Q_{10} + Q_{12})Q'_{21}A'_{10}}{(A'_{10} + Q'_{10})((A_{10} + Q_{10} + Q_{12})(A_{20} + Q_{20} + Q_{21} + Q'_{21}) - Q_{12}Q_{21})} \tag{2.22}$$

2.2.3.1 Absorption Integral Calculation

We now focus on the first portion of Equation 2.20 and consider the rate of population of the upper $B^2\Sigma^-$ state. As in case of the simple two-level model, this term involves the computation of the integral of the product of the laser linewidth function, $\psi(\nu)$ and the absorption linewidth function, $\phi(\nu)$. However, since our excitation scheme targets multiple lines in the R-bandhead, we actually have a summation of several absorption lines in this integral.

$$\begin{aligned} W_{02} &= \frac{I}{c} \int \psi(\nu) \sum_j B_j \phi_j(\nu) d\nu \\ &= \frac{I}{c} \sum_j B_j \int \psi(\nu)\phi_j(\nu) d\nu \end{aligned} \tag{2.23}$$

In Equation 2.23, the terms B_j are the absorption coefficients, B_{02}, for each transition being excited, each of which has its own broadened linewidth, $\phi_j(\nu)$ at the local conditions. The discussion of the various sources of line broadening that need to be considered for our case is deferred until Chapter 4.

2.2.3.2 Population Distribution

Equation 2.24 presents the expression for f_j in terms of the vibrational and rotational quantum numbers, (v, J), of the energy level j.

$$f_j(v, J) = \frac{\exp\left(\dfrac{-hcE_v(v)}{kT}\right)(2J+1)\exp\left(\dfrac{-hcE_r(v, J)}{kT}\right)}{Q_{rv}} \qquad (2.24)$$

The vibrational energy, $E_v(v)$ of a level is calculated according to Equation 2.25, while the rotational energy, $E_r(v, J)$ is calculated according to Equation 2.26.

$$E_v(v) = \omega_e\left(v + \frac{1}{2}\right) - \omega_e x_e\left(v + \frac{1}{2}\right)^2 + \omega_e y_e\left(v + \frac{1}{2}\right)^3 - \omega_e z_e\left(v + \frac{1}{2}\right)^4 \qquad (2.25)$$

$$E_r(v, J) = \left\{B_e - \alpha_e\left(v + \frac{1}{2}\right)\right\}J(J+1) - \left\{D_e + \beta_e\left(v + \frac{1}{2}\right)\right\}J^2(J+1)^2 \qquad (2.26)$$

The ground state, $X^2\Pi$, of the CH system is conforms to Hund's Case b[69] and hence, the appropriate rotational quantum number to use is N. For each rotational quantum number N, there are two possible values of J given by $N \pm \frac{1}{2}$. The rovibrational partition function, Q_{rv} is a summation over all available vibrational and rotational levels in the $X^2\Pi$ state. In practice, this summation over the vibrational states may be truncated at $v = 4$ and the summation over the rotational states may be truncated at $N'' = 22$ with negligible loss in accuracy. The values of the various spectroscopic constants in the above equations will be presented in Chapter 4.

2.2.3.3 Solution

The solution for the rate of production of fluorescence photons can be written in the following form that mirrors Equation 2.14.

$$\Phi = \frac{P}{c} \int_x n_{CH}(Y + Y') \sum_j f_j B_j \int_\nu \psi(\nu)\phi_j(\nu)d\nu dx \tag{2.27}$$

The expressions for the fluorescence yields, Y and Y', still have many variables that have not been tabulated conveniently in literature. As a result, further simplifications will need to be made on the basis of reported experimental observations. These simplifications are outside the scope of this chapter and will be introduced in Chapter 4 along with the results of applying this model to various reactant mixtures.

CHAPTER 3

EXPERIMENTAL METHODS AND CONSIDERATIONS

The current chapter describes the experimental apparatus and the diagnostic approaches used in this work. The first section presents a detailed description of the LSB configurations that were tested, along with the testing facilities used for the experimental work. The second section focuses on the selection and implementation of the diagnostic techniques that were used to study flames and flow fields. Data reduction techniques used to process the acquired raw data are also described.

3.1 LSB Configurations

Two configurations of the Low Swirl Burner were tested for this study. These are referred to in what follows as Configurations A and B. Each configuration consists of the reactant flow inlet, the swirler device, the conduit to the combustion zone and the combustion zone itself. Figure 2.1 shows the design of the swirlers used for this study. Each swirler has an outer diameter, d_s, of 38 mm (1.5 in) and divides the flow into a central and annular portion. One of these configurations used swirlers with a perforated plate that had a concentric hole pattern as shown in the figure. The perforated plate induces a blockage in the central channel and controls the relative mass flow split between the two portions of the swirler. The key dimensions of the swirlers tested are presented in Table 3.1.

Each configuration is housed in a high pressure testing facility. The testing facility consists of an air and fuel supply system, a pressure vessel with adequate optical access and an exhaust system for the products. Each testing facility is instrumented to measure temperatures and pressures which are then used to calculate various flow

Table 3.1: *The dimensions of the swirlers used and the respective perforated plates are presented. Each swirler is referred to by its vane angle (as in "$S_{37°}$").*

Geometric parameter	Swirlers		
	Configuration A		Configuration B
	$S_{37°}$	$S_{45°}$	$S_{40°}$
Swirler data			
Outer diameter, d_s, mm	38	38	38
Diameter ratio, $\frac{d_i}{d_s}$	0.66	0.66	0.66
Vane angle, α	37°	45°	40°
Theoretical Swirl Number, S	0.48	0.64	variable
Perforated plate data			
Open area, mm^2	155.97	156.98	N/A
Blockage, %	71.54	71.36	-
Plate thickness, mm	1.27	1.27	-
Hole pattern	1-8-16	1-8-16	-
Hole location (dia), mm	0-10.2-19.1	0-10.2-19.1	-
Hole diameter, mm	2.79-2.79-2.84	2.82-2.82-2.83	-

parameters of interest.

The design of the configurations tested, along with that of their respective test facilities are discussed in detail in this section.

3.1.1 Configuration A

Preliminary experiments involving velocity field mapping and flame imaging were performed using this configuration. The schematic of the high pressure test facility housing this configuration is shown in Figure 3.1, while the configuration itself is shown in greater detail in Figure 3.2.

3.1.1.1 Test Facility

Pressurized air is supplied from external tanks and heated in an indirect, gas-fired heat exchanger to about 500 K. The flowrate of the air is metered using a sub-critical
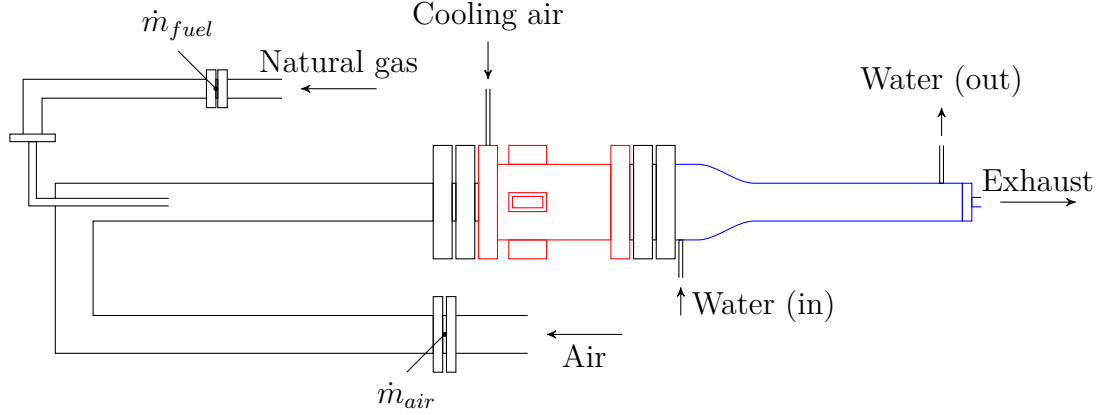
Figure 3.1: *A schematic of the high pressure testing facility where Configuration A is operated is shown. The pressure vessel is outlined in red, while the water-cooled exhaust section is outlined in blue. The locations of the orifice flow meters used to measure the mass flow rates of the preheated air and natural gas fuel are indicated.*

orifice flow meter with a 38 mm (1.5 in) bore diameter Flow-Lin orifice plate capable of metering a maximum flow rate of 2.2 kg/s (1 lb/s). The orifice flow meter is instrumented with an Omega PX725A-1KGI pressure transmitter calibrated to a reduced pressure range of 0–2.758 MPa (0–400 psi), a shielded K-type thermocouple and an Omega PX771A-025GI differential pressure transmitter, calibrated to a reduced differential pressure range of 0–68.948 kPa (0–10 psid). The fuel (natural gas) is metered using a similar set up as the air line, with a sub-critical orifice flow meter. The fuel orifice plate is a Flow-Lin orifice plate with a bore diameter of 13.46 mm (0.53 in), capable of metering a maximum flow rate of 0.22 kg/s (0.1 lb/s). The upstream pressure is measured using an Omega PX725A-1KGI pressure transmitter (same as the air line) and the differential pressure is measured using a PX771A-100WDC differential pressure transmitter with a pressure range of 0–2.489 kPa (100 in H_2O). The temperature of the fuel is assumed to be the same as the nominal room temperature (300 K).

The air enters the inlet nozzle of the LSB through a 1.8 m (6 ft) long, 102 mm (4 in) diameter straight pipe section. The fuel flow is choked prior to mixing with the air flow at the head of the straight pipe section. The straight pipe section allows for the

flow to be fully developed, and fully premixed before the reactants enter the burner. The combustor pressure and temperature are measured at the head of the inlet nozzle. The pressure is measured by an Omega PX181B-500G5V pressure transducer with a pressure range of 0–3.45 MPa (0–500 psi), while the temperature is measured using a K-type thermocouple.

The pressure and temperature measurements are used to calculate the four primary flow parameters (combustor pressure, preheat temperature, reference velocity and equivalence ratio) for the LSB in real time. All measurements are monitored and recorded during the course of the experiment by a LabView VI.

The pressure vessel enclosing the combustor is designed to withstand pressures of up to 30 atm and is insulated from the combustor by a ceramic liner. Cooling for the pressure vessel and the quartz tube is provided by a flow of cold air introduced at the head of the pressure vessel. The cold air is drawn from the same external tanks as the main air line, but bypasses the heating system. The cold air flow is not metered, but its upstream pressure is coupled to the main air line so as to ensure a steady flow of cold air into the pressure vessel at all operating conditions. Optical access to the combustor is provided through four 25 mm (1 in) thick, 150 mm (6 in)×75 mm (3 in) quartz windows located 90° apart azimuthally. The view ports allow the combustor to be imaged from the dump plane to an axial distance of 150 mm (6 in) downstream.

The exhaust from the combustor is cooled by cold water circulated through a water jacket enclosing each section of the exhaust pipe. The length of the exhaust pipe sections is about 1.8 m (6 ft). The exhaust pipe section terminates in an orifice plug that provides back pressure to the combustion chamber. A different diameter orifice is used for each reference velocity condition tested. The exiting products finally pass through the building exhaust system.
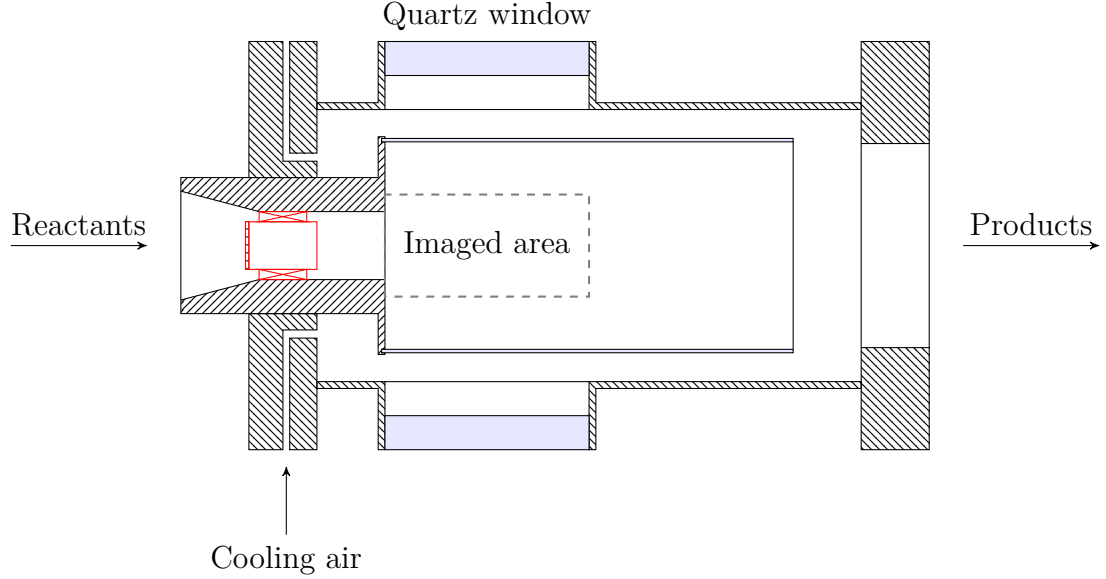
Figure 3.2: *A cross-sectional view of Configuration A in the pressure vessel is shown. The reactants enter from the left. The products mix with the cooling air and leave on the right. The location of the swirler in the inlet nozzle is highlighted in red. Also shown is the region of the combustion zone that can be imaged through the quartz windows.*

3.1.1.2 Low Swirl Burner

A detailed schematic of the LSB configuration is shown in Figure 3.2. The premixed, preheated reactants reach the swirler through a converging nozzle that decreases linearly in diameter from the inlet diameter of 102 mm (4 in) to the outer diameter of the swirler, 38 mm (1.5 in). At the swirler, the flow splits into two streams— one passing through the central section and another picking up swirl by flowing over the vanes in the annular region. The relative flow split between the two streams is controlled by inducing blockage into the central flow by means of a perforated plate. The swirler leads to a constant area nozzle, and is located one diameter upstream of an abrupt area change. At the area change, the reactants expand from the 38 mm (1.5 in) diameter nozzle into a 115 mm (4.5 in) diameter combustion zone. This expansion ratio is chosen so as to avoid confinement effects on the centerline flame flow field.[28]

The main combustion zone begins at the dump plane and is enclosed by a GE

41
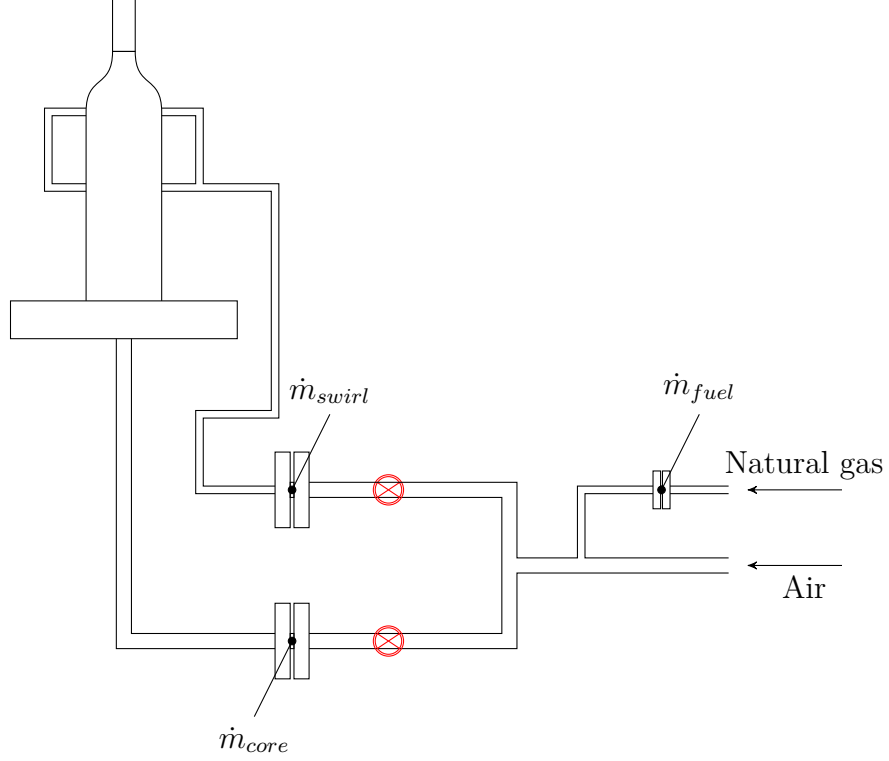
Figure 3.3: *A schematic of the high pressure testing facility where Configuration B is operated is shown. The locations of the orifice flow meters on the reactant streams and fuel lines are shown. Valves (shown in* red*) on the swirl and core flow lines allow for the relative mass flow split to be varied between the two reactant streams. The upstream orifice flow meter on the preheated air line is not shown here. All preheated air lines are insulated.*

214 quartz tube. The quartz tube is 300 mm (12 in) long and 115 mm (4.5 in) in diameter. The thickness of the quartz tube is 2.5 mm (0.1 in).

3.1.2 Configuration B

This configuration is used to image the flame structure of the LSB flame using CH PLIF. A schematic of the flow system of the test facility is shown in Figure 3.3, while the LSB combustor itself is shown in greater detail in Figure 3.4.

3.1.2.1 Test Facility

This test facility shares the upstream supply of preheated air and natural gas with the one used in Configuration A. The flow rate of the preheated air stream is mea-

sured using the same orifice flow meter system used in Configuration A—albeit with a smaller 12.921 mm (0.5087 in) diameter bore Flow-Lin orifice plate. The fuel system pressure is regulated from the building supply pressure to a lower required pressure by an adjustable TESCOM regulator and metered using a critical orifice flow meter. The critical orifice on the fuel line has a bore diameter of 0.8128 mm (0.032 in). The pressure upstream of the critical orifice is measured using an Omegadyne PX409-1.5KGI pressure transmitter with a range of 0–10.34 MPa (0–1500 psig) and the pressure downstream of the critical orifice is measured using a Dwyer 626 series pressure transmitter with a range of 0–3.45 MPa (0–500 psig). The downstream pressure can be used to verify if the critical orifice is choked during operation. The temperature of the fuel is measured upstream by a K-type thermocouple.

The air system is choked with a 5.41 mm (0.213 in) diameter critical orifice before mixing with the fuel. A short distance after mixing, the reactants are split into two separate streams for the central flow and the swirl flow. The central flow rate is measured using a 9.271 mm (0.365 in) diameter sub-critical orifice, instrumented with a Dwyer 626 series pressure transmitter with a range of 0–4.14 MPa (0–600 psig) for measuring the upstream pressure, a K-type thermocouple for measuring the upstream temperature and an Omega PX771-300WCDI differential pressure transducer with a range of 0–74.65 kPa (0–300 in H_2O). The swirl flow rate is measured similarly, using a 11.68 mm (0.46 in) diameter sub-critical orifice, a Dwyer 626 series pressure transmitter with a range of 0–5.52 MPa (0–800 psig), a K-type thermocouple and another Omega PX771A-300WCDI with a differential pressure range of 0–74.65 kPa (0–300 in H_2O). The relative flow split between the two reactant streams is controlled by partially closing gate valves on the two lines. All measurements are monitored and recorded by a LabView VI.

The test rig is designed to be operated with a pressure vessel and is rated for pressures as high as 30 atm. Unfortunately, the rig could not be operated at high

pressure for the experiments performed in this study. The original design of the rig, developed for a separate program of research investigating turbulent flame speeds, was found to be incapable of successful operation at high pressure. As a result, the combustor was operated without a pressure vessel in the present work. The products are vented into the same building exhaust system as Configuration A.

3.1.2.2 Low Swirl Burner

The design of this LSB configuration is presented in Figure 3.4. As described earlier, the reactants reach the LSB swirler device through two separate streams. The core/central stream passes through a plenum chamber that is filled with steel ball bearings before approaching the swirler through a smoothly contoured nozzle with a high contraction ratio. The annular/swirl stream reaches the swirler directly through a separate contoured nozzle. The contraction ratio is chosen to inhibit the formation of thick boundary layers in the reactant streams. The core stream passes through the central portion of the swirler, while the annular stream picks up swirl by passing through the vanes of the swirler. The swirler lacks a perforated plate covering the central region as the primary function of the plate—regulating the relative mass flow split—is performed by the test facility itself.

The swirler device is located at the beginning of a constant area nozzle which is 57.2 mm (2.25 in) in length. Following this, the reactants expand into the combustion zone.

Unlike Configuration A, there is no dump plane or quartz tube to provide confinement to the combustion zone. The co-flow of cold air provides insulation to the walls of the pressure vessel. Also, as mentioned earlier, the relative mass flow split between the central and annular flows can be controlled directly. Finally, the level of turbulence in the central flow can be adjusted by use of a turbulence generator[70] located upstream in the plenum chamber.
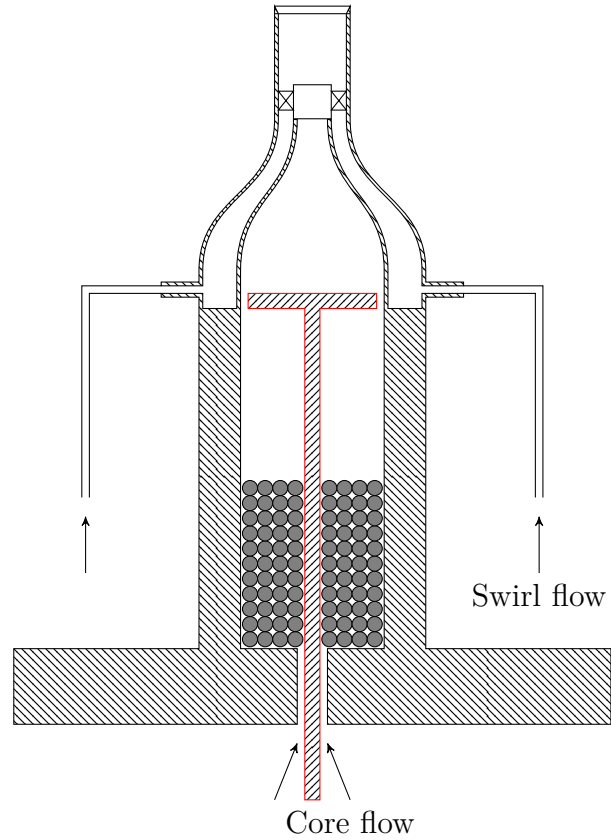
Figure 3.4: *A cross-sectional view of Configuration B is shown. The core flow reactants enter through ports in the base flange. Stainless steel ball bearings partially fill the plenum chamber and render the core flow spatially uniform. The turbulence generator is located within the plenum and is outlined in* red. *The swirl flow reactants enter through separate pipes and are injected into the contoured nozzle through four ports.*

3.2 Diagnostics

3.2.1 Laser Doppler Velocimetry

The velocity field of the LSB is mapped using a TSI 3-component LDV system. Three wavelengths (514 nm, 488 nm and 476 nm) are separated from the output of a 5 W Argon ion laser by an FBL-3 multicolor beam generator. The individual beams are split into two coherent beams, which are then focused to intersect and produce interference fringes within an ellipsoidal measurement volume with dimensions of the order of 100 μm. For this purpose, two transceiver probes are mounted 90° apart about the axis of the LSB. The setup is illustrated in Figure 3.5. One transceiver probe focuses the 514 nm and 488 nm beams in planes perpendicular to each other, while the second probe focuses the 476 nm beams orthogonal to the other two beams. Particles in the flow field crossing the interference fringes scatter the laser light elastically and produce a sinusoidal signal whose frequency is proportional to the velocity of the particle. The transceiver probes collect this scattered light and each wavelength is detected separately by a PDM-1000-3 three-channel photodetector module. The output from the photodetector is processed by an FSA-3500-3 signal processor. The resulting three components of the particle/flow velocity are recorded by the FlowSizer software.

Since the concentration of particulate matter (primarily dust particles) in the airflow is very low, the flow needs to be artificially seeded to facilitate LDV measurements in a reasonable amount of time. The choice of seeding particles to be used and their mean diameter are decided by the characteristics of the flow to be imaged.[71] Since the LSB flow field is a reacting one, the particles need to have high melting points. Further, the particles need to be small enough to follow the flow closely and large enough or reflective enough to scatter light efficiently in the measurement volume. Based on these requirements, commercially available alumina particles with a
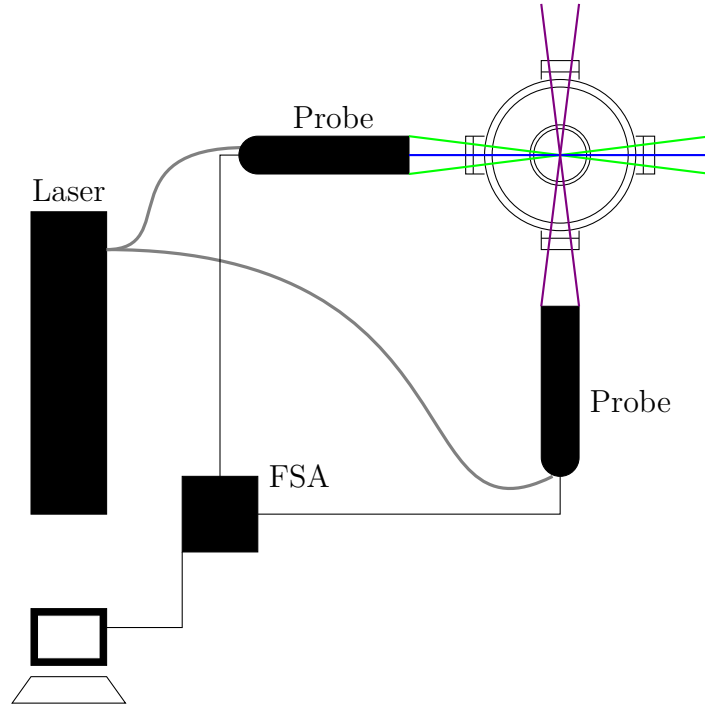
Figure 3.5: *The schematic shows the setup employed to map the velocity field of the LSB combustor using Laser Doppler Velocimetry. Three pairs of orthogonal beams are separated from the Argon Ion Laser output and conveyed by fiber optic cables (gray) to optical probes mounted 90° apart about the axis of the LSB combustor. The green, blue, and violet beams in the schematic represent the 514 nm, 488 nm and 476 nm wavelengths. The signal is collected by the transceiver probes and analyzed by the FSA module. The results are saved for further analysis.*

mean particle diameter of 5 μm were chosen for this study. In order to uniformly seed the flow, a novel seeding generator was designed as described in Appendix A. The seeding particles were introduced slightly upstream of the 1.8 m (6 ft) long straight pipe section in Test Rig A.

LDV data is only acquired at atmospheric pressure conditions. At high pressure conditions, the reacting LSB flow field produces sharp refractive index gradients that rapidly shift in the turbulent flow field. This causes strong beam steering effects making it very difficult for the laser beams to reliably intersect within such a small measurement volume.[72] The long distance traveled by the beams in the test rig further exacerbate this problem, making LDV data nearly impossible to acquire at such conditions.

3.2.2 CH* Chemiluminescence

The LSB flame is imaged using one of two 16-bit intensified CCD cameras—PI Acton 1024×256 or 512×512 pixels—with a 28 mm f/2.8 camera lens. The quantum efficiency of the 18 mm Gen III HB filmless intensifier used by the 512×512 camera is about 45% at 430 nm, while the 25 mm Gen II intensifier used by the 1024×256 camera manages about half that at the same wavelength. CH* chemiluminescence is filtered using a bandpass filter centered on 430 nm with a FWHM of 10 nm. At each operating condition, 100 instantaneous images are acquired with an exposure of 1 ms. An additional 100 instantaneous images are acquired with no flame and averaged to yield the background for correcting the flame images.

3.2.2.1 Image Processing

The acquired flame chemiluminescence images are background-corrected and averaged. The resulting mean is the line-of-sight integrated, time-averaged image of the flame. Strictly speaking, this is not the same as a real average obtained from a long

exposure image as the instantaneous images are obtained through a periodic sampling process and hence, are prone to statistical errors. However, the behaviour of the flame can be assumed to be sufficiently random that the mean obtained is adequately representative of the true average. Figure 3.6a shows a typical mean CH* chemiluminescence image prepared in this manner.

Even when background-corrected, the walls of the combustor are not at zero intensity in the average chemiluminescence image. This is particularly noticeable near the dump plane where there is no flame present and yet the walls are clearly illuminated. The source of this background illumination is mostly the chemiluminescence from the flame scattering off the combustor and pressure vessel walls. The contribution from blackbody radiation from the heated walls is less significant in the narrow wavelength range imaged. This is evident from images acquired immediately after a flame blowout, which show the walls to be nearly dark even though they should still be hot.

The averaged chemiluminescence image allows us to measure the flame standoff distance by following the intensity profile along the centerline of the combustor. The intensity profile rises sharply when passing the flame standoff location. Thus, the flame standoff location can be ascertained by finding the inflection point in the intensity profile.

The profile of the average chemiluminescence intensity along the centerline of the sample case from Figure 3.6a is shown in Figure 3.6b, showing the flame standoff distance. The distance from the dump plane, measured in number of pixels on the image and scaled by the appropriate magnification factor yields the flame standoff distance, X_f. The determination of the flame standoff location by this method provides a suitable and deterministic means to locating the leading edge of the flame front.

The average image can be processed further to yield more spatially resolved in-
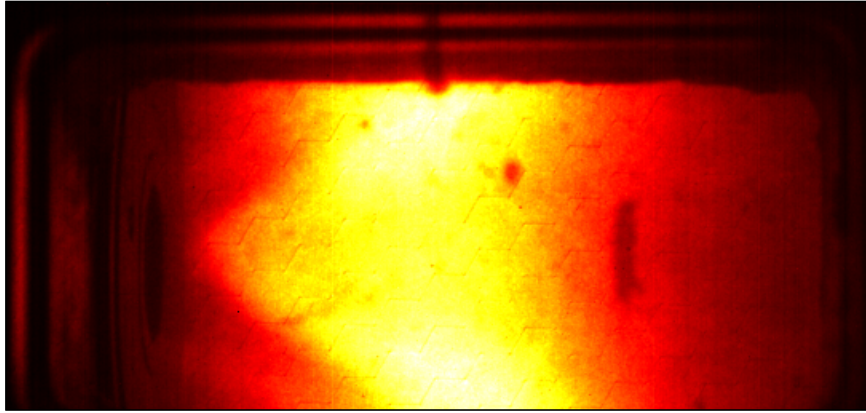
(a) *Average CH* chemiluminescence image*
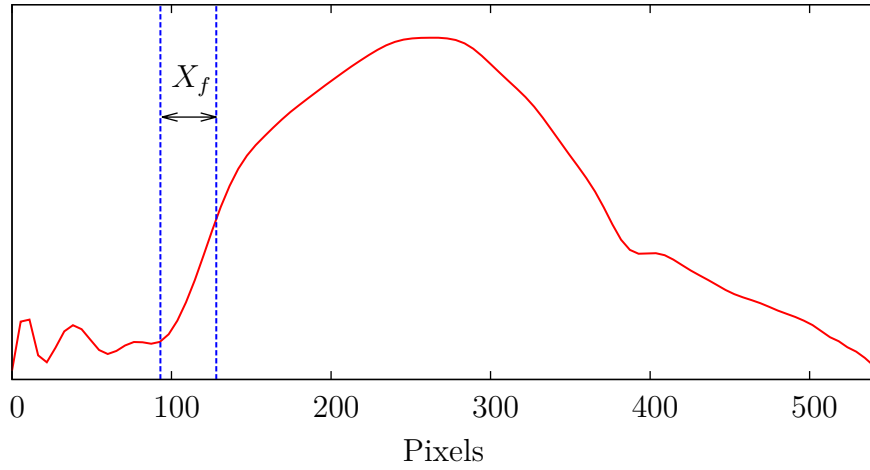
(b) *Centerline CH* chemiluminescence intensity*
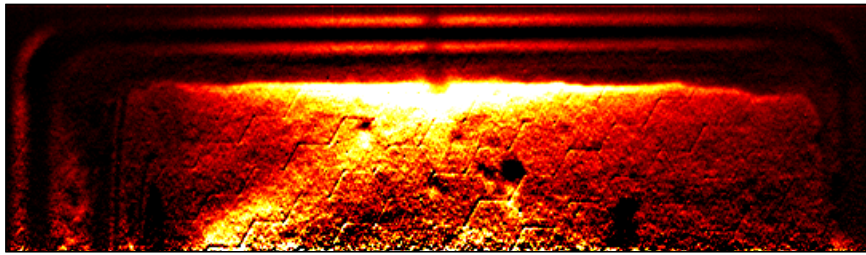
(c) *Abel deconvoluted half-image*

Figure 3.6: *These images illustrate the processing of a typical CH* chemiluminescence dataset. The top image is the mean of 100 frames and shows the LSB flame at 9 atm. The flame standoff distance is calculated by locating the inflection point in the smoothed intensity profile (middle). An Abel deconvolution (bottom) can be used to highlight the flame brush and measure the angle of the flame.*

50

formation about the flame brush. Under the reasonable assumption that the average LSB flame is axially symmetric about the centerline of the combustor, a tomographic deconvolution technique called an Abel deconvolution[73] can be used to convert the line-of-sight integrated image to a radial map of chemiluminescence intensity. In effect, this shows the shape and structure of the average flame brush. The Abel deconvolution of the sample data from Figure 3.6a is shown in Figure 3.6c.

The Abel-deconvoluted image provides a relatively easy means of determining the flame brush angle. A straight line joining two points located at the center of the flame brush intersects the axis of the combustor at this angle. The angle of the flame is denoted by θ_f.

Using the Abel deconvolution to study the flame brush suffers from two main drawbacks. First, the system of equations describing the Abel deconvolution is only valid as long as the entirety of the flame is visible. This is only satisfied in the initial region of the LSB where the diameter of the flame brush is smaller than the height of the optical viewport. At further downstream locations, the flame is not imaged in its entirety. This causes the spurious bright regions near the top of the window in Figure 3.6c. The second limitation of the Abel deconvolution technique stems from the high incidence of errors along the centerline (where $r \to 0$). Due to this, any study of the flame brush thickness at the flame stabilization point—a metric of considerable importance—is all but impossible using this tomographic technique.

3.2.3 CH Planar Laser-Induced Fluorescence

The CH PLIF setup uses the frequency-doubled output of a Light Age PAL 101 alexandrite laser tuned to $\lambda \approx 387.2$ nm. The design of the laser is shown schematically in Figure 3.7. The active medium is a 150 mm (6 in) long, 5 mm (0.197 in) diameter alexandrite rod. The rod is placed between two flashlamps within the resonator cavity formed by two spherical mirrors. A birefringent tuning element is

51
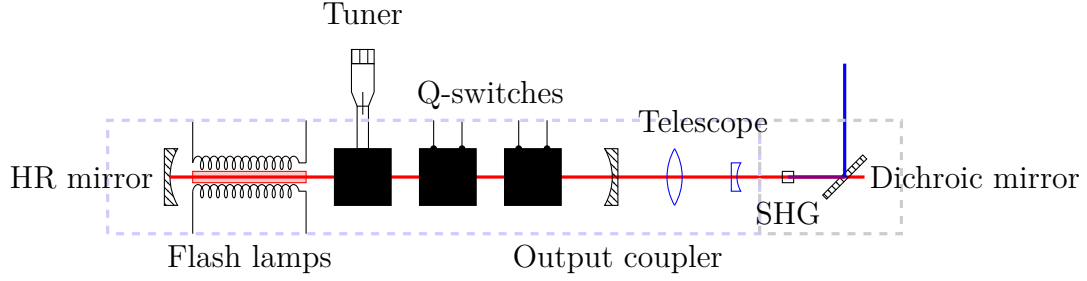
Figure 3.7: *A schematic of the components of the PAL 101 Alexandrite laser is shown. The resonator formed by a High Reflection (HR) mirror and an output coupler is built around an alexandrite rod (red) pumped by flashlamps. The frequency of the output is selected by a tuner mechanism. Only one of the two Q-switches was used for this study. The laser beam is reduced in diameter by a collimating telescope (blue) before passing through the Second Harmonic Generator (SHG). The UV beam is separated from the fundamental by a dichroic mirror and exits the laser. The fundamental beam terminates within the laser in a beam dump.*

placed within the resonator to allow the user to select the frequency of the output beam. The tuning element is coupled to a micrometer whose reading relates linearly to the output wavelength. The birefringent filter allows the fundamental wavelength to be varied between 720–780 nm, with peak gain at about 755 nm. The resonator cavity also contains two Q-switches, which allow the laser to optionally operate in double-pulsed mode. For this study, however, only one Q-switch is used and the laser is operated in single-pulsed mode only.

The diameter of the fundamental beam exiting the output coupler is reduced by a collimating telescope. This is done in order to increase the efficiency of conversion of the frequency-doubling crystal. The second harmonic portion of the beam is separated from the fundamental by a dichroic mirror and exits the laser. The fundamental beam is terminated at a beam dump within the laser. The exit beam diameter is about 1 mm.

The alexandrite laser is capable of operating at frequencies of up to 15 Hz. Laser power is controlled primarily by varying the voltage applied to the flash lamps. When operating with a high flash lamp voltage, it is recommended that the frequency of pulsing be reduced to allow more time to dissipate the heat build up within the

alexandrite rod. All experiments conducted as part of this study operated the laser at 10.0 Hz.

The typical power output of the laser is about 15 mJ/pulse. The pulsewidth of the laser is about 60-80 ns, as measured by a fast photodiode, and the pulsewidth decreases with increasing flash lamp voltage. The linewidth of the fundamental beam, as reported by the manufacturer, is 150 GHz at $\lambda = 775$ nm. Assuming the spectral profile of the laser to be a Gaussian, the linewidth of the frequency-doubled beam can be determined. The Full Width at Half Max (FWHM) of a Gaussian curve scales linearly with the standard deviation of the curve. When convoluted with itself, the new standard deviation is $\sqrt{\sigma^2 + \sigma^2}$ or $\sqrt{2}$ times that of the original curve. Thus, the linewidth of the frequency doubled output is $150 \times \sqrt{2} = 212$ GHz or 7.07 cm^{-1}. In wavelength units, this represents a spread of about 1.06 Å.

3.2.3.1 Imaging System

All of the PLIF imaging is performed with an intensified PI Acton 512×512 camera. The intensified camera is equipped with an 18 mm Gen III HB filmless intensifier with a quantum efficiency of about 45% in the 420–440 nm range. The lens is chosen depending on imaging requirements of each experiment. In all imaging experiments, elastic scattering from the laser beam is attenuated by a 3 mm thick GG 420 Schott Glass filter.

3.2.3.2 Laminar Flame Setup

Preliminary experiments to evaluate the CH PLIF technique are performed on a laminar flame. The choice of a laminar flame as the subject allows us to neglect effects of strain and turbulence on the flame. Further, laminar flames are more readily simulated by reaction kinetics packages like Chemkin with high fidelity, allowing us to model the LIF signal easily.

These experiments are conducted on a laminar, methane-air flame stabilized on an unpiloted Bunsen burner with an inner diameter of 10.16 mm (0.4 in). The air flow rate is measured and regulated using a Dwyer rotameter with a range of 0–20 SCFH calibrated using a Ritter drum-type gas meter. The natural gas flow rate is metered using a Matheson FM 1050 602 rotameter with a range from 0–1230 SCCM. This flowmeter is calibrated using a Sensidyne Gilibrator 2 bubble flow meter system.

3.2.3.3 Laser Wavelength Calibration

As described earlier, the output wavelength of the PAL 101 alexandrite laser is controlled using a micrometer-coupled birefringent tuning mechanism. The wavelength of the laser beam varies linearly with the micrometer reading. Initially, the manufacturer-supplied calibration for the micrometer was found to be inaccurate. This required an experiment to calibrate the laser output wavelength against the micrometer reading in order to determine the slope and offset of the calibration curve accurately.

A schematic of this experiment is shown in Figure 3.8. The laser beam is glanced off a steel optical post and the scattered light is collected using a fiber-optic cable coupled to an Ocean Optics HR 2000 spectrometer. The spectrometer is pre-calibrated using 50 wavelengths in the 400–850 nm range from the output of a neon discharge lamp source. The spectrometer is also intensity-corrected over this range using a black body source. The estimated error in the resolution of the device is about 0.1 nm (1 Å).

The laser micrometer is traversed from 0.600 in to 0.625 in in steps of 0.001 in. The experiment is repeated by traversing the micrometer from 0.625 in back to 0.600 in along the same points to ensure repeatability and estimate the variation due to hysteresis. The calibration is performed using at the fundamental wavelength of the laser as the second harmonic wavelength falls outside the spectrometer's range. Each
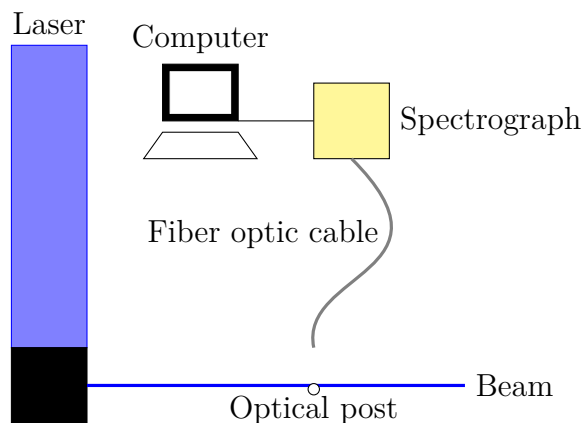
Figure 3.8: *The figure above shows the schematic of the experiment performed to calibrate the wavelength of the laser output. The laser output (containing mostly UV, but also a small portion of the fundamental frequency) is glanced off a steel optical post. The scattered light is gathered by a fiber optic cable (gray) and sent to a spectrometer. The spectrum is analyzed to track the location of the fundamental frequency with tuner position. The UV peak is not tracked as the spectrometer is not calibrated for that wavelength.*

spectrum recorded is integrated over 512 ms and averaged over 10 such acquisitions. The background-corrected peak of the spectrum is then modeled as a Gaussian and the location of the center of the Gaussian waveform is recorded.

The results from this experiment are shown in Figure 3.9. The plot demonstrates that the variation of the second harmonic wavelength (obtained by halving the fundamental wavelength) with the position of the tuner micrometer is linear. Further, there is little difference between the measurements taken while increasing and decreasing the micrometer position. This indicates that any effects of hysteresis in the micrometer position are minimal. The calibration equation relating the micrometer position to the output wavelength is obtained by applying a linear curve fit to the data points on the graph as shown in Figure 3.9.
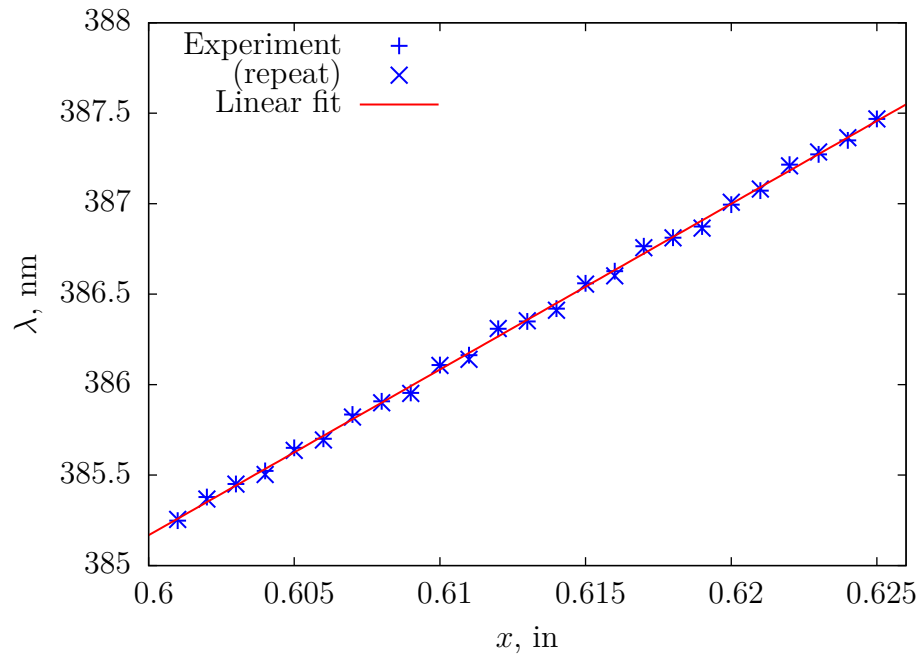
Figure 3.9: *The wavelength of the second harmonic beam of the laser is plotted above against the tuner position(x). The data shows excellent repeatability and falls on a linear trend. The equation for the linear curve fit is $\lambda = 330.213 + 91.5908x$, where the units of λ and x are nm and in, respectively.*

CHAPTER 4
CH PLIF SIGNAL MODELING AND VALIDATION

This chapter deals with the evaluation of CH PLIF as a diagnostic technique. Preliminary experiments to evaluate the optimal use of the CH PLIF imaging system are detailed. This is followed by a discussion of some detailed aspects of modeling the LIF signal. The results of applying the model to a reference laminar flame are compared with experimental results. Finally, the model is used to predict the feasibility of using the developed CH PLIF system to study various hydrocarbon combustion systems, with a focus on flame zone imaging.

4.1 CH PLIF Preliminary Experiments

The CH PLIF imaging system described in Chapter 3 was evaluated for use in imaging hydrocarbon flames by performing three preliminary experiments. First, an excitation scan was performed to confirm the location of the optimal wavelength to excite the CH radicals in a typical hydrocarbon flame. Second, a test of the linearity of the LIF signal with respect to the incident laser intensity was performed. Finally, a spectrum of the LIF emission was recorded and compared to calculations. The setup and results of these experiments are described in the following subsections.

4.1.1 Excitation Scan

An excitation scan is performed by tuning the output of the alexandrite laser from λ = 387.077 nm to 387.260 nm. This serves two purposes. First, it locates the optimal wavelength to excite the CH radicals that results in the highest fluorescence yield. Second, the variation of the signal intensity can be compared with simulated profiles
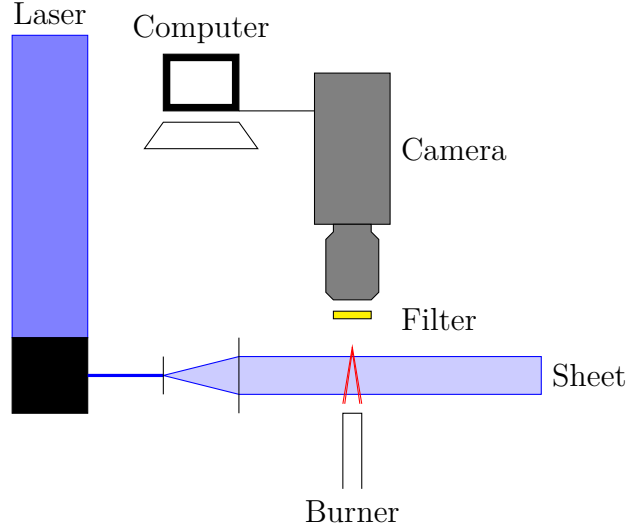
Figure 4.1: *A schematic of the excitation scan experiment is shown. A collimating pair of lenses form the laser beam into a sheet focused over a laminar Bunsen burner. The fluorescence is imaged perpendicularly by an intensified camera synchronized to the laser pulse. A 3 mm GG 420 filter is used to reject elastic scattering.*

from LIFBASE[74] or other spectroscopic calculations and our estimation of the laser linewidth can be validated. The laser linewidth is an integral parameter and appears in the absorption integral used by the models developed in Chapter 2.

A schematic of the excitation scan experiment is shown in Figure 4.1. The intensified PI Acton 512×512 camera described in Section 3.2.2 is used to image a premixed, laminar methane-air flame operating at close to stoichiometric conditions. The laminar flame is stabilized on the Bunsen burner described in Section 3.2.3.2. The alexandrite laser is operated at a power of 16 mJ/pulse in the second harmonic. The sheet forming optics consist of a +50 mm cylindrical lens and a +250 mm spherical lens placed 300 mm apart. The optics form the beam into a collimated sheet about 25 mm (1 in) tall, focused to a thickness on the order of 250 μm at the flame location. The sheet passes through the center of the flame and the edges of the sheet are blocked by razor blades to prevent reflections from the burner from saturating the camera.

The induced fluorescence in the flame sheet is imaged perpendicularly by the in-

tensified camera using an 85 mm f/1.8 Nikon AF Nikkor lens. A 3 mm thick 50 mm×50 mm square GG 420 Schott glass filter is used to reject elastic scattering at the excitation wavelength. This setup gives a magnification of approximately 62 μm/pixel. The camera is triggered by the flash lamp sync signal from the laser system and the intensifier is gated over 300 ns, encompassing the 70 ns laser pulse. The long gate width gives the intensifier enough time to prepare to receive the fluorescence, preventing signal loss due to irising. The gate width is still short enough that minimal flame chemiluminescence or ambient lighting is recorded in the images. 100 instantaneous images are acquired for each excitation wavelength to acquire a good estimate of the mean fluorescence signal, μ_{sig}.

Figure 4.2 shows a sample CH PLIF image from this dataset. The images are background-corrected by subtracting the laser scattering (recorded without the flame). The fluorescence signal is calculated from these images using three alternate approaches.

In Method I, two windows are identified that include the straight sections of the laminar flame. The average fluorescence signal in each frame is calculated by taking the average of all the emitting pixels in the two windows. A pixel is designated as an emitting pixel if its intensity exceeds the standard deviation of a typical background pixel by at least a factor of five. In Method II, the intensity of the pixels is integrated over a straight line connecting the inner and outer edges of the flame. The straight line is chosen along the beam so that the beam intensity does not vary along the integration path. The integration is performed on the left and right arms of the flame, giving two readings per frame. The integral is averaged over all the frames. In Method III, the midpoints of the flame along the straight lines from Method II are located and their intensities are averaged. The regions of interest for each of these methods are highlighted in Figure 4.2.

The result of this investigation is shown in Figure 4.3. The calculated mean
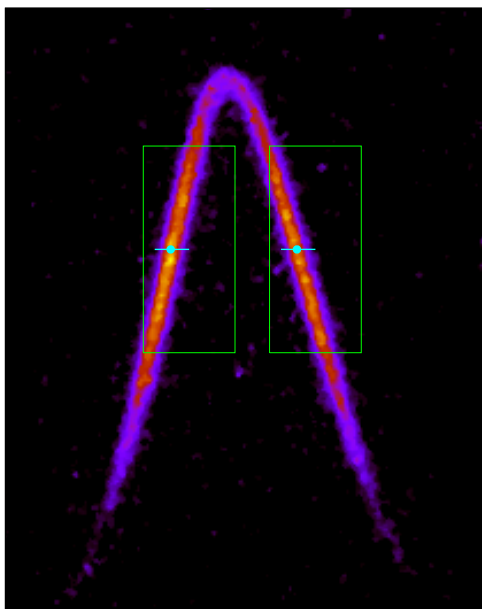
Figure 4.2: *The image shows a typical instantaneous laminar flame from the excitation scan experiment. Regions of interest are identified on the image corresponding to the window method (green) and the line method (cyan). The midpoint of the flame sheet is also indicated on the image.*

fluorescence signals from the three methods are plotted against a LIFBASE simulation of the absorption spectrum of the CH $B-X$ transition. The profiles are appropriately scaled to match the LIFBASE simulation at the maximum value and at the minimum value. The LIFBASE simulation is performed for a thermalized system at 1800 K and at atmospheric pressure. Further, the instrument linewidth is specified to be the same as our estimate of the laser linewidth (1.06 Å).

The line and midpoint methods use fewer pixels to calculate the mean and show minor deviations from the predicted results. The window method uses more pixels and shows much smoother agreement with the simulated profile. In general, the agreement between the measurements and the calculations is excellent. The agreement is in fact so good that a minor adjustment to the calibration of the laser wavelength could be made using these results.

The results indicate that the optimal excitation wavelength, corresponding to the
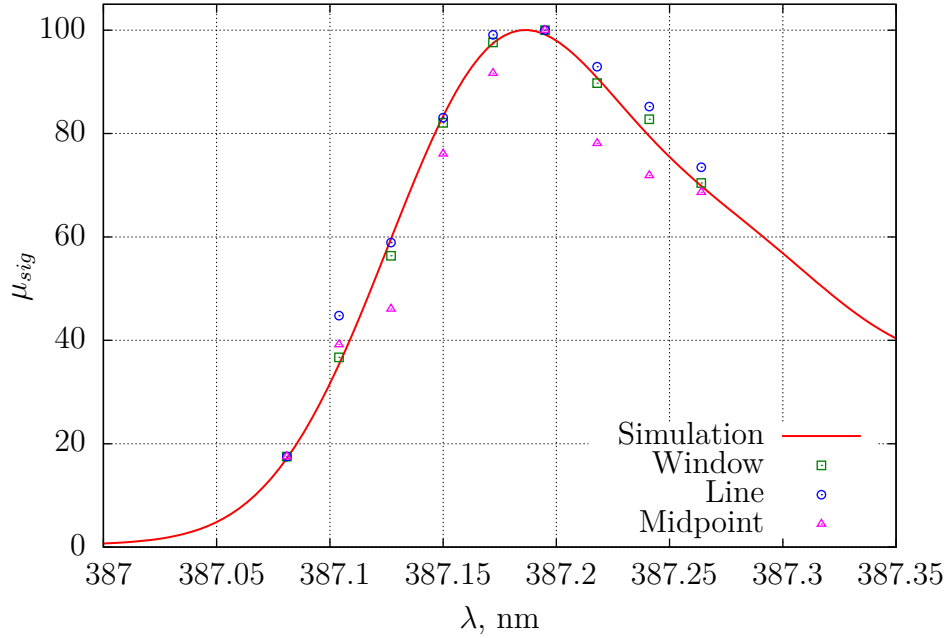
Figure 4.3: *The plot shows the mean signal level of an emitting pixel determined by three separate analysis methods. They are compared to a simulated excitation scan from LIF-BASE.*

highest mean fluorescence signal, is about 387.2 nm. For the rest of the experiments performed in this work, the laser is operated at this wavelength. The results also help fine tune the calibration of the micrometer over this small region of the spectrum. Finally, the results validate that our estimated laser linewidth, 1.06 Å, is accurate. This value is used in subsequent calculations of the LIF signal levels.

4.1.2 Linearity Test

As explained in Chapter 2, the variation of the fluorescence signal with the excitation laser intensity can exhibit a saturation behavior at sufficiently high intensity. For reasons mentioned in that discussion, we prefer to operate in the weak excitation limit where the fluorescence signal scales linearly with the input laser energy. Further, the models developed in Section 2.2 use fluorescence yield expressions that are only valid in the linear regime. Hence, an experiment is performed to verify the linearity of the system response at the intensities at which the flames are imaged for this work.
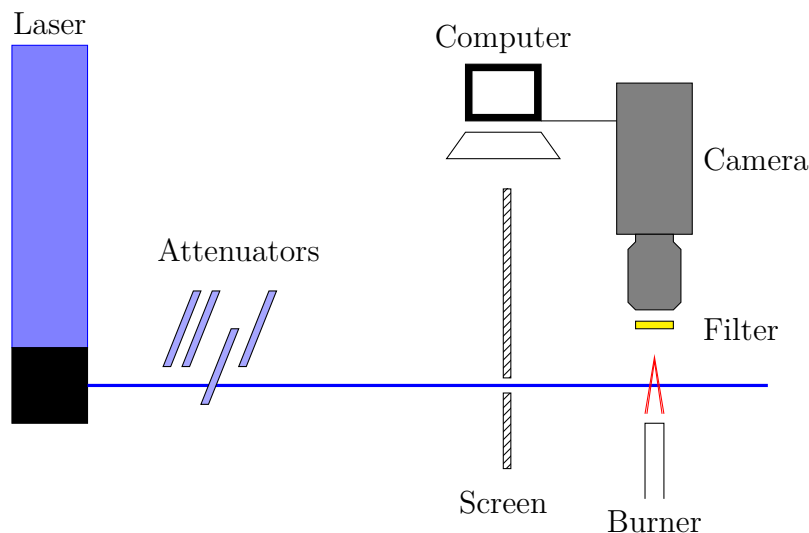
Figure 4.4: *A schematic of the experimental setup used to perform the linearity experiment is shown. An unrefracted beam from the laser is directed at a laminar flame and imaged perpendicularly. The beam energy is progressively attenuated by introducing multiple quartz blocks and disks. The drift in the beam is minimized by using attenuating elements in pairs so that any beam deviation is compensated.*

The schematic of the setup is shown in Figure 4.4. The laser is tuned to the optimal wavelength as determined in Section 4.1.1, and operated at 10 Hz. The frequency-doubled beam is directed at a steady, laminar, methane-air Bunsen flame operating at a slightly rich stoichiometry. The edges of the beam are clipped by an aperture to produce a sharp edge and to avoid unnecessary reflections from the burner. No optics are used to refract the beam in any way.

The flame is imaged by the PI Acton 512×512 intensified camera equipped with a 50 mm, f/1.8 AF Nikkor lens. Elastic scattering is attenuated by a 3 mm thick GG 420 Schott glass filter. The magnification achieved by this set up is about 44 μm/pixel. The LIF signal from the flame is recorded in 300 ns gates and accumulated 150 times before being read out. For each case, a corresponding laser scattering image is also recorded for estimating the background. The flame chemiluminescence and ambient background are also recorded for the same purpose.

For this experiment, varying the intensity of the laser beam by changing the flash lamp voltage or even the Q-switch timing is not preferred as either would alter the
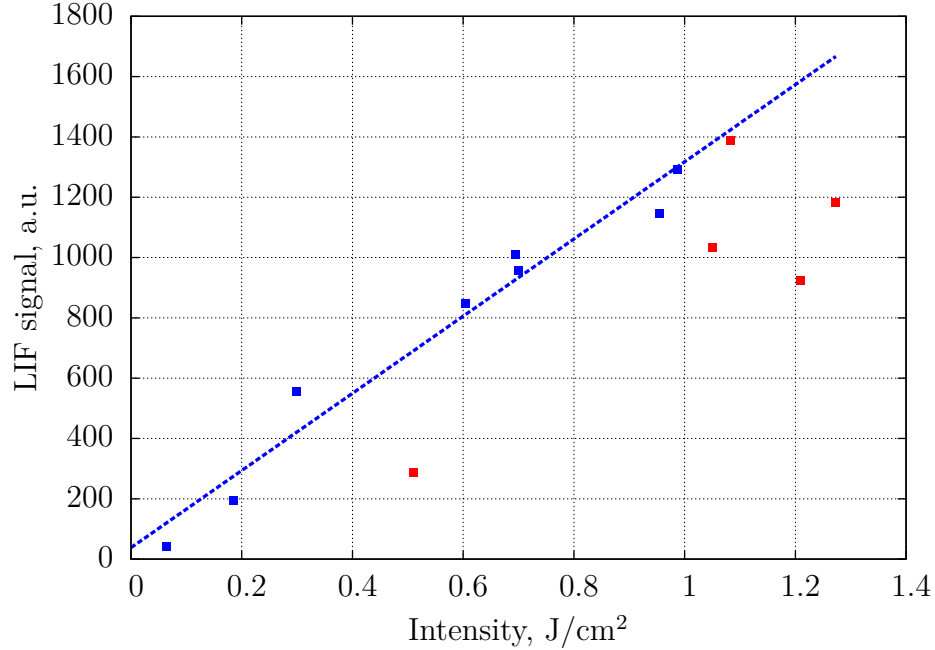
Figure 4.5: *The plot shows the results of the linearity experiment. The LIF signal intensity is measured for a range of input laser energies (expressed here an an intensity). The data points below 1 J/cm² are marked in* blue *and fitted to a linear curve. One outlier (*red*), along with data points at high laser intensities are not included in the linear fit.*

pulsewidth of the beam. Instead, beam intensity attenuators—quartz disks and blocks of varying thickness—are introduced into the beam to produce an intensity loss, while preserving all other characteristics of the beam. The quartz elements decrease the intensity of the laser beam through reflection, scattering and absorption. The stray reflections and scattering from the quartz elements are kept from contaminating the flame image by using a screen. In this manner, the laser power is varied from 10 mJ/pulse to 0.5 mJ/pulse and back.

The acquired images are background-corrected and the intensity is conditionally averaged over pixels with a non-zero intensity in the region where the fluorescence occurs. The average fluorescence intensity values thus obtained are plotted against the corresponding laser intensity and shown in Figure 4.5.

The LIF signal is observed to increase monotonically with increasing laser intensity. At the lower intensities, the variation is very nearly linear, with marginal scatter

and only one significant outlier. At intensities above 1 J/cm^2 however, there is significant scatter in the data and any linear trends from the low intensity cases cannot be reliably extended over this region. Figure 4.5 shows a linear fit over the low intensity points that indicates that as long as the intensity of the laser sheet is kept below 1 J/cm^2, the assumption of operating in the linear regime is clearly valid. As the intensity required to saturate the LIF signal increases with pressure, linearity is also assured for higher operating pressures. All CH PLIF images that were acquired for this study were acquired at laser intensities below the 1 J/cm^2 level.

4.1.3 LIF Emission Spectrum

The CH LIF emission spectrum was also recorded. This serves two purposes. First, by verifying that the recorded spectrum matches the calculated one from LIFBASE, we can be reasonably sure of the source of the emission. Second, other sources of emission of comparable or greater intensity, if any, can be located on the spectrum. If such sources are discovered, they would need to be blocked with filters to ensure accurate flame zone location images.

The experiment is again performed on the laminar flame set up, operating a methane-air flame at an equivalence ratio slightly richer than stoichiometry. The CH layer in the laminar flame is excited by an unrefracted beam from the alexandrite laser. The resulting emissions are collected using a fiber optic cable. No filter is used to block any wavelengths for this experiment. The fiber optic cable is aligned with a 100 μm wide slit of a 0.3 m, f/4 SpectraPro 300i spectrometer which separates the light into its spectrum using a 600 lines/mm grating. The spectrum is imaged using the PI-MAX 512×512 camera and accumulated over 1000 gates of 300 ns each. The flame chemiluminescence background collected using identical gates is found to be negligible.

A portion of the measured spectrum is shown in Figure 4.6. The simulated spec-
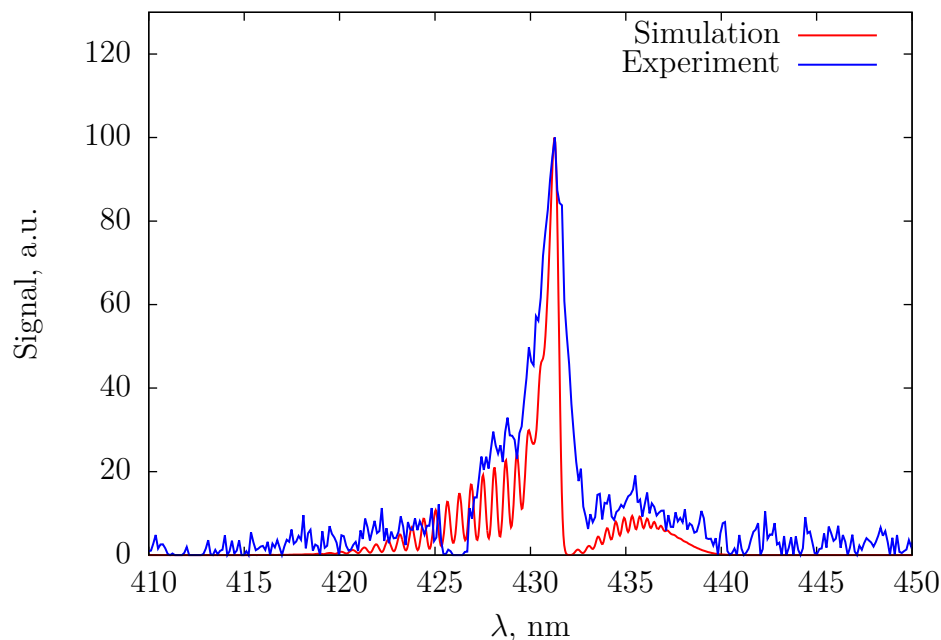
Figure 4.6: *The plot shows the experimentally measured spectrum of the LIF emission (blue) from a Bunsen flame averaged over 1000 accumulations. This is compared to a simulated LIF emission spectrum (red) generated by LIFBASE.*

trum is from LIFBASE for a 1 atm, thermalized CH system at 1800 K. The resolution of the simulation is set to match the calculated resolution of the spectrometer (about 0.3 nm), based solely on the number of pixels. The actual spectrometer resolution should be degraded due to diffraction effects and imperfections of the grating. The peaks agree quite well with the simulated result. Further, no other emissions of comparable intensity are found up to 520 nm, the maximum wavelength detected. Therefore, it can be concluded that in lean hydrocarbon flames (at least at atmospheric pressure), the laser-induced signal in the detection range 410-520 nm should be due primarily to CH LIF.

4.2 Fluorescence Signal Modeling

Chapter 2 presented analysis of LIF signal calculation as a function of thermodynamic conditions and the local composition in a flame. Expressions derived using a

Table 4.1: *The coefficients of spontaneous emission for transitions in the CH system are provided.*

Transition	Symbol	A $\times 10^6$ s^{-1}
$B^2\Sigma^- \to X^2\Pi(0,0)$	A_{20}	2.963
$A^2\Delta \to X^2\Pi(1,1)$	A_{10}	1.676
$A^2\Delta \to X^2\Pi(0,0)$	A'_{10}	1.832

basic model (Equation 2.14) and a more complex model (Equation 2.27) were presented. The expressions rely on knowledge of several physical values and specific spectroscopic constants pertaining to the CH system. This section lists several of these constants along with further simplifications that need to be made in order to computationally evaluate the predicted signal through a flame. The flame predictions are then presented in the next section.

4.2.1 Fluorescence Yield

The fluorescence yield expressions in Equations 2.21–2.22 are in terms of the Einstein coefficients of spontaneous emission, A_{ij} and the rates of collisional quenching, Q_{ij}. The values for the Einstein spontaneous emission coefficients used in this study are collated from literature[68, 75] and tabulated in Table 4.1.

The quenching rates between various energy levels are harder to calculate. As shown in Equation 2.9, the rates calculated as a function of the local composition, thermodynamic conditions and the quenching cross-section, σ_i, of the colliding species. CH is a minor species in typical hydrocarbon flames, with its concentration rarely exceeding a few ppm. Consequently, most of its collisions will occur with the major species in the flame. Thus, it is only required to know the quenching cross-sections of major species to estimate the collisional quenching rate within acceptable uncertainty.

Table 4.2: *The functional form of the quenching cross-sections of various species with CH are provided.*

Species	σ Å^2
H_2	$6.1 \exp\left(-686/T\right)$
H	$221 T^{-0.5} \exp\left(-686/T\right)$
O_2	$8.61 \times 10^{-6} T^{1.64} \exp\left(867/T\right)$
OH	$221 T^{-0.5} \exp\left(-686/T\right)$
H_2O	9.6
CH_4	$52.8 T^{-0.5} \exp\left(-84/T\right)$
CO	8.31
CO_2	$8.67 \times 10^{-13} T^{3.8} \exp\left(854/T\right)$
C_2H_6	13.4
N_2	$1.53 \times 10^{-4} T^{1.23} \exp\left(-522.1/T\right)$
C_3H_8	22

Quenching cross-sections are typically functions of temperature, but vary little with pressure. Several researchers have reported experimentally measured collisional cross-sections for many species in hydrocarbon-air flames, modeling their temperature dependence over an increasingly wide range of temperatures[64, 65, 75–94] relevant to combustion. Of these, the current study uses functional forms for several species in methane-air flames from Tamura et al.[92], some of which were updated by Renfro et al.[94]. Quenching cross-sections for higher alkanes are taken from Chen et al.[86, 88, 89] These functional forms are tabulated in Table 4.2.

The fluorescence yield expressions also involve several collisional transfer rates between the energy levels of interest. There have been efforts[66, 95] to measure and/or model these rates, but the energy level models used for these studies are more complicated and cannot be easily reconciled with our model of the CH system. Hence, it is preferable to make some simplifying assumptions so that these collisional transfer rates can be reduced in terms of known quenching rates.

Cool et al.[78] and Garland et al.[64] report that excited CH molecules in the $B^2\Sigma^-$

electronic state are about 30% more likely to be quenched than molecules in the $A^2\Delta$ states. The researchers observe that the quenching rates do not vary appreciably over the vibrational manifold. This observation lets us make the following assumptions eliminating Q'_{10} and Q_{20} in terms of Q_{10}.

$$Q'_{10} = Q_{10} = Q$$

$$Q_{20} = 1.3Q \tag{4.1}$$

Next, Garland et al.[64] and later, Luque et al.[65] report that the rate of transfer following the $B^2\Sigma^- \to A^2\Delta$ (0,1) transition accounts for almost 24% of the collisional removal of CH from the upper electronic state. This allows us to formulate one more equation as shown below.

$$\frac{Q_{21} + Q'_{21} - Q_{12}}{Q_{20} + Q_{21} + Q'_{21} - Q_{12}} = 0.24$$

$$\therefore \frac{Q_{21} + Q'_{21} - Q_{12}}{Q} = 0.4105 \tag{4.2}$$

The same authors also report that the collisional transfer from $B^2\Sigma^-$, $v = 1$ populates the $A^2\Delta$, $v = 1$ level four times faster than the $A^2\Delta$, $v = 0$ level.

$$\frac{Q_{21} - Q_{12}}{Q'_{21}} = 4 \tag{4.3}$$

Finally, Garland et al.[64] note that the rate of forward transfer in the $B^2\Sigma \to A^2\Delta$ (0,1) transition is about 60% faster than the reverse process.

$$\frac{Q_{21}}{Q_{12}} = 1.6 \tag{4.4}$$

Garland et al.'s observations in particular are made from experimental data in an atmospheric pressure, methane-air flame in which they estimate the flame temperature to be 2000 K. This value is representative of the flame temperatures in most of our cases and hence we assume that we can treat these ratios as constants for our application.

Equations 4.2–4.4 form a closed set of linear equations that can be written out in matrix form and solved. Equation 4.5 presents this solution, eliminating Q_{21}, Q'_{21} and Q_{12} in terms of Q.

$$\begin{bmatrix} Q_{21} \\ Q'_{21} \\ Q_{12} \end{bmatrix} = \begin{bmatrix} 0.8758 \\ 0.0821 \\ 0.5474 \end{bmatrix} Q \qquad (4.5)$$

Substituting Equations 4.1 and 4.5 into Equations 2.21–2.22 leads to simplified expressions for the two fluorescence yields as shown in Equations 4.6–4.7. More importantly, they are now functionally dependent on only the Einstein coefficients and the rates of collisional quenching from $A^2\Delta \to X^2\Pi$, which are known.

$$Y_1 = \frac{0.8758 A_{10} Q}{(A_{10} + 1.5474Q)(A_{20} + 2.2579Q) - 0.4794Q^2} \qquad (4.6)$$

$$Y'_1 = \frac{0.0821(A_{10} + 1.5474Q) A'_{10} Q}{\left(A'_{10} + Q\right)\left((A_{10} + 1.5474Q)(A_{20} + 2.2579Q) - 0.4794Q^2\right)} \qquad (4.7)$$

The final unknowns are the number densities of the major species in the flame zone. The profile of the local mole fraction of the various species through a 1-D, freely propagating, laminar flame can be obtained from Chemkin calculations using the Flame-Speed Calculator reactor model. Results presented in this chapter cover laminar flames burning a range of reactant mixtures at various inlet conditions. Additional results are presented for strained, laminar, methane-air flames which are

calculated using the Opposed flow flame reactor model.

The Chemkin results provide mole fractions and thermodynamic conditions, which can be used to solve for the number density using the following equation.

$$n_i = \frac{pN_AX_i}{\bar{R}T} \tag{4.8}$$

In Equation 4.8, N_A is Avogadro's number, X_i is the mole fraction of species i, $\bar{R}$ is the universal gas constant and p, T are the local pressure and temperature in the flame.

4.2.2 Absorption Integral

The absorption term in Equation 2.27 requires us to calculate the Boltzmann fractions for the energy levels involved and the absorption integral over each transition line being excited by the laser. First, we focus on the Boltzmann fraction expression from Equation 2.24. The vibration energy expression from Equation 2.25 needs the spectroscopic constants ω_e, $\omega_e x_e$, $\omega_e y_e$ and $\omega_e z_e$. Simultaneously, the expression for the rotational energy in Equation 2.26 requires knowing B_e, α_e, D_e and β_e values for the levels being excited. Accurate values of these constants for the $X^2\Pi$ state are tabulated in Zachwieja's[96] paper. These are tabulated in Table 4.3.

Next, we discuss the calculation of the absorption integral, which requires the following;

- line positions in the $B^2\Sigma^- \leftarrow X^2\Pi$ (0,0) transition that are being excited by the laser,

- Einstein coefficients for stimulated absorption for these transitions,

- Laser center wavelength,

- Laser lineshape, and

Table 4.3: *Spectroscopic constants for the CH $X^2\Pi$ state are presented.*

Constant	Value cm^{-1}
ω_e	2860.7508
$\omega_e x_e$	64.4387
$\omega_e y_e$	0.36345
$\omega_e z_e$	-1.5378×10^{-2}
B_e	14.459883
α_e	0.536541
D_e	1.47436×10^{-3}
β_e	-2.530×10^{-5}

- Absorption lineshapes for each of the excited transitions

The line positions in the R-branch of the $B^2\Sigma^- \leftarrow X^2\Pi$ (0,0) transition along with the respective Einstein B-coefficients are obtained from LIFBASE's database and are tabulated in Table 4.4.

The linewidth of the alexandrite laser is of the order of a few wavenumbers and its lineshape, $\psi(\nu)$, has a Gaussian profile.[13]

$$\psi(\nu) = \frac{1}{\sigma_l\sqrt{2\pi}} \exp\left(-\frac{(\nu - \nu_l)^2}{2\sigma_l^2}\right) \tag{4.9}$$

The center position, ν_l, of the lineshape profile is varied by tuning the center wavelength of the laser. The Full Width at Half Max (FWHM) of the laser, $\Delta\nu_l$, was determined from the laser excitation scan fits, and can be used to calculate the standard deviation of the Gaussian as follows.

$$\sigma_l = \frac{\Delta\nu_l}{2\sqrt{2\ln 2}} \tag{4.10}$$

The lineshape of the absorption line being excited, on the other hand, is primarily dictated by mechanisms associated with gas-phase media—collisional broadening and

Table 4.4: *The line positions and the corresponding Einstein coefficients for stimulated absorption for transitions in the $B^2\Sigma^- \leftarrow X^2\Pi$ (0,0) R branch are presented below.*

N''	J''_1	ν_1 cm^{-1}	B $\times 10^{-9}$ m^{2}J^{-1}s^{-1}	J''_2	ν_2 cm^{-1}	B $\times 10^{-9}$ m^{2}J^{-1}s^{-1}
1	0.5	25756.08	6.511	1.5	25774.03	5.823
2	1.5	25776.42	7.225	2.5	25782.72	6.489
3	2.5	25792.74	7.532	3.5	25797.06	7.174
4	3.5	25805.42	7.671	4.5	25808.75	7.460
5	4.5	25814.47	7.719	5.5	25817.20	7.581
6	5.5	25819.80	7.708	6.5	25822.13	7.610
7	6.5	25821.28	7.652	7.5	25823.32	7.581
8	7.5	25818.72	7.561	8.5	25820.55	7.506
9	8.5	25811.93	7.439	9.5	25813.59	7.396
10	9.5	25800.64	7.288	10.5	25802.17	7.254
11	10.5	25784.57	7.111	11.5	25785.98	7.083
12	11.5	25763.38	6.907	12.5	25764.70	6.884
13	12.5	25736.65	6.676	13.5	25737.88	6.657
14	13.5	25703.90	6.418	14.5	25705.06	6.402
15	14.5	25664.54	6.129	15.5	25665.64	6.116
16	15.5	25617.87	5.815	16.5	25618.92	5.804
17	16.5	25563.03	5.472	17.5	25564.03	5.463
18	17.5	25499.00	5.101	18.5	25499.95	5.094
19	18.5	25424.52	4.624	19.5	25425.42	4.618
20	19.5	25338.08	4.161	20.5	25338.93	4.156
21	20.5	25237.84	3.674	21.5	25238.64	3.670
22	21.5	25121.60	3.183	22.5	25122.36	3.180

Doppler broadening being the most important ones. Collisional broadening is a homogeneous mechanism and produces a Lorentzian broadened lineshape. The FWHM of the Lorentzian profile is related to the thermodynamic conditions by the following empirical formula.

$$\Delta\nu_c = 0.1 \left(\frac{p}{p_0}\right) \left(\frac{T_0}{T}\right)^{0.6} \tag{4.11}$$

In Equation 4.11, p_0 and T_0 represent standard conditions of pressure and temperature (101325 Pa and 300 K) respectively. By contrast, Doppler broadening is an inhomogeneous mechanism that results in a Gaussian lineshape. Its effect depends on the frequency (wavenumber) of the line being broadened, ν_a, and on the molecule's velocity. The FWHM of the resulting broadened lineshape is given by,

$$\Delta\nu_d = \nu_a \frac{\sqrt{\ln 2}}{c} \sqrt{\frac{8kT}{m_{CH}}} \tag{4.12}$$

The combined effect of these two broadening mechanisms can be calculated by convoluting the two broadened lineshapes. In this case, a Lorentzian convoluted with a Gaussian results in a Voigt profile. The computational expense of the convolution that needs to be performed for each absorption line at each point along the flame is high. Further, the absorption integral needs to be evaluated by multiplying the Voigt profile with the Gaussian profile of the laser. In order to simplify this without losing too much accuracy, we replace the collision broadened Lorentzian with a Gaussian of equal FWHM. The convoluted profile is now a Gaussian, too and the product of two Gaussians can be easily integrated to get the absorption integral.

The limits of this assumption leading to replacing the Voigt profile with a Gaussian profile need to be stated. If the dominant broadening mechanism were Doppler broadening, the resulting Voigt profile would approximate a Gaussian much closer. For CH LIF, this is a reasonable assumption in the high temperature regions where

CH exists, at least at pressures below a few bar. However at high pressure, collisional broadening is no longer negligible compared to Doppler broadening. Hence, the resulting Voigt shape will have a reduced peak absorption and relatively more area in the "wings" of the curve. In the absorption integral, this would lead to increased absorption of the laser energy by transitions near the edge of the laser lineshape. Fortunately, when the laser line position is tuned to optimally excite the R-bandhead spanning the lines $N'' = 5$ to $N'' = 9$, the next nearest transition ($N'' = 4$) is far enough away that even with increased absorption, contribution from these lines remains insignificant even at very high pressures.

Returning to the calculation of the absorption integral, we now replace the collision-broadened Lorentzian profile by a Gaussian profile with the same FWHM. Now, the convolution of the collision-broadened and Doppler-broadened lineshapes results in another Gaussian with the same mean and a new FWHM given by,

$$\Delta\nu_a = \sqrt{\Delta\nu_c{}^2 + \Delta\nu_d{}^2} \tag{4.13}$$

Thus, the Gaussian lineshape of the broadened absorption line can be written as,

$$\phi(\nu) = \frac{1}{\sigma_a\sqrt{2\pi}} \exp\left(-\frac{(\nu - \nu_a)^2}{2\sigma_a^2}\right) \tag{4.14}$$

In Equation 4.14, ν_a is the frequency (wavenumber) of the absorption peak being excited. The standard deviation of the lineshape, σ_a, is related to the broadened FWHM, $\Delta\nu_a$, by the following equation.

$$\sigma_a = \frac{\Delta\nu_a}{2\sqrt{2\ln 2}} \tag{4.15}$$

With the above information, the integral in Equation 2.23 can be solved analyti-

cally as follows.

$$\int \psi(\nu)\phi(\nu)d\nu = \frac{1}{\sqrt{2\pi(\sigma_a^2 + \sigma_l^2)}} \exp\left(-\frac{(\nu_l - \nu_a)^2}{2(\sigma_a^2 + \sigma_l^2)}\right) \qquad (4.16)$$

Having discussed the means to calculate the absorption integral in a computationally-efficient manner, it is now possible to calculate the optimal laser location that results in the highest value of the absorption integral for a given temperature and pressure. The resulting value depends on both the pressure and the temperature at the flame. The optimal laser wavelength determined from these calculations is found to steadily increase with pressure. The behavior with temperature is non-monotonic. The optimum wavelength initially decreases, reaching a minimum around 1800 K and then increases again. However, these variations are so small (less than 0.0003 nm) over the range of temperatures and pressures encountered in combustion that we may optimize the wavelength using an atmospheric flame and leave it untouched while imaging flames at pressure and/or with preheat.

4.3 Chemkin modeling

To restate the goals of this exercise, the aim is to predict the intensity of the LIF signal across operating conditions to test the feasibility of using CH PLIF as a technique to visualize the flame sheet in a combustor. While the primary reactant mixture of interest is methane-air, the analysis can be extended to other alkane-air mixtures and even syngase-alkane-air mixtures. The choice of the kinetics model to calculate the species profiles across flames is thus decided by how well it applies to all the reacting mixtures being considered.

GRI Mech is a chemical kinetics mechanism that uses 53 chemical species and 325 reactions to accurately simulate natural gas-air combustion with emphasis on pollutant formation. As CH is a key species in the formation of NO_x, several CH

data sets are used as optimization targets for fine tuning the mechanism. Berg et al.[97] report that the results agree well near stoichiometry, but are too low for lean flames and too high for rich flames. Since GRI Mech is developed to solve methane-air problems, its applicability to higher-order alkanes is not well validated. As a result, only the methane-air case is solved using GRI Mech in this study.

For specialized application to higher-order combustion, USC's C_1-C_3 mechanism builds upon a CO-H_2 chemistry base and seeks to optimize more than 250 parameters to sufficiently cover C_3 chemistry, at the expense of decreased accuracy for C_1 and C_2 cases. On the other hand, their Syngas mechanism extends GRI Mech to cover H_2-CO mixtures, retaining its limitations for C_3-alkane mixtures. USC also publishes the USC Mech version II which is specifically targeted at H_2-CO-C_1–C_4 compounds that draws upon several models including GRI Mech. It uses 111 species and 784 reactions to model the chemistry, making it computationally expensive to use over a large parametric sweep.

USCD's San Diego Mechanism is designed with a more minimalist intent of simulating combustion using the least number of species and reaction rate parameters. Subsequent updates to the mechanism have extended its applicability to an increasing number of combustion and detonation processes. The 2011-11-22 release uses 235 reactions, with additional data available for extending it to cover heptane and even JP10 chemistry. Due to its wide applicability, low computational cost and good accuracy, most of the results presented in this chapter use this mechanism.

4.4 Results

In this section, the CH signal intensity model is used to predict the LIF signal (or relative photon count) emitted by the flame in a few selected reactant mixtures.

4.4.1 Unstrained Laminar Flames

The LIF signal is related to many parameters in a flame. It is directly dependent on the temperature profile through a flame, as well as on the concentrations of all major species. In order to reduce the complexity of relating the signal to too many parameters at once, we restrict our attention to a simple unstrained, laminar flame and study LIF signal variation with reactant composition and inlet conditions.

4.4.1.1 Methane-Air Flames

We begin by validating the predictions from two mechanisms—GRI Mech 3.0 and San Diego—against experimental data acquired from a non-preheated, atmospheric, methane-air Bunsen flame. The laminar flame setup from Section 3.2.3.2 is used for this purpose. The laser beam was formed into a 25 mm tall sheet bisecting the laminar flame and was imaged perpendicularly using the intensified PI-MAX 512×512 camera with a 50 mm f/1.4 lens. The sheet thickness was about 250 μm and the laser power averaged about 14 mJ per pulse during the course of the experiment. The images are background-corrected and averaged over a window encompassing the PLIF signal from the flame sheet. The experiment was repeated over an initial range of equivalence ratios between 1.55 on the rich side and 0.90 on the lean side. By reducing the reactant flow rate, the range was further extended to 0.82 on the lean side. Below this equivalence ratio, the unpiloted Bunsen flame could no longer be stabilized.

The results are compared to the modeled signal intensity from the GRI Mech and San Diego results for a 1-D, freely propagating laminar flame. The predicted CH PLIF signals are based on a spatial integral across the CH layer thickness. The three profiles are normalized and plotted in Figure 4.7.

The equivalence ratio producing the maximum signal predicted by both mechanisms agrees with the experimental value, about $\phi = 1.25$. Further, both methods predict similar decreases in the LIF signal as the equivalence ratio is varied from the
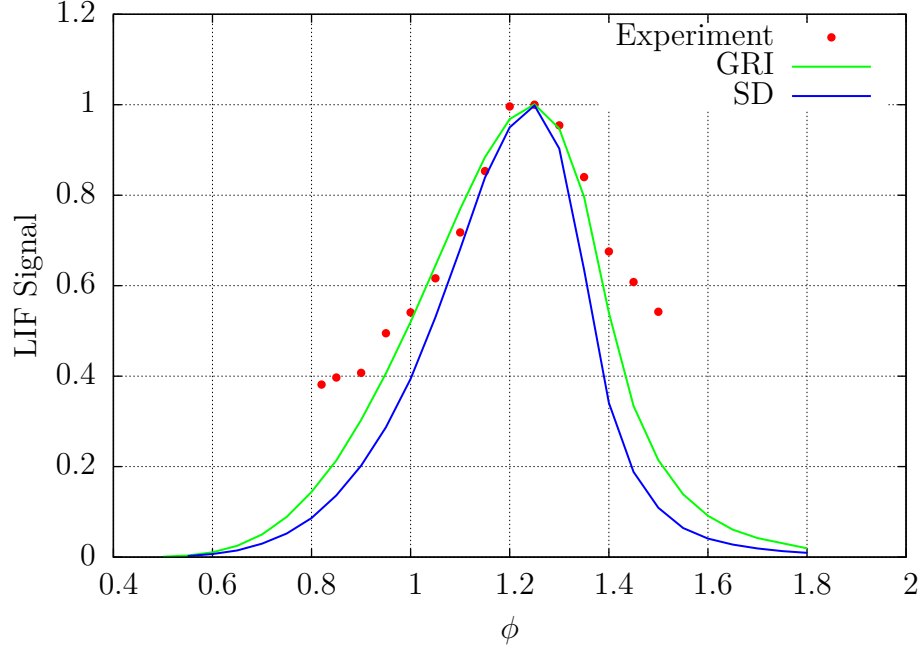
Figure 4.7: *The plot compares the experimentally measured LIF signal to the values predicted by the signal model. The experiment is conducted at 1 atm, 300 K on a laminar Bunsen flame burning a methane-air mixture. Two reaction mechanisms (GRI Mech 3.0 and San Diego) are used to generate the relevant data used by the signal model. All three datasets are normalized at the peak value.*

peak, which are also in reasonably good agreement with the experimental results. However, at the lower signal levels encountered at both the leanest and richest conditions at which the flame was imaged, the experimental results are seen to diverge from the model predictions. At these conditions, the models predict a more rapid drop in the signal compared to the experimental results. One possible reason for this difference is insufficient background-correction on the PLIF images, causing the background signal to be relatively high when compared to LIF signals at their lowest values. Further, for the leanest cases imaged, the flame is also much shorter and the LIF signal may be affected by tip stretch effects absent in the longer flames at other equivalence ratios. Nevertheless, the experimental profile agrees reasonably well with the model predictions.

Next, we can compare the predictions from the GRI Mech 3.0 and San Diego mech-

anisms for an unstrained, freely propagating, 1-D, methane-air laminar flame against each other. Figure 4.8a shows the calculated CH profile across a stoichiometric flame at atmospheric pressure and three preheat temperatures. At these conditions, the San Diego mechanism predicts almost 50% less CH concentration compared to the GRI Mech 3.0 mechanism. Both mechanisms predict the increased CH concentration at higher preheat conditions, along with the thinning of the flame zone. Figure 4.8b shows the flame thickness predicted by the two mechanisms which agree quite well, diverging only at rich equivalence ratios. The predicted laminar flame speeds and flame temperatures are shown in Figures 4.8c and 4.8d respectively and the differences between the two mechanisms are again quite minimal. The results of this investigation indicate that other than the nearly consistent discrepancy of about 50% in the predicted CH concentration, the results from the two mechanisms scale identically. Since we are not concerned with the accurate prediction of the CH concentration, but merely the relative variation across conditions, this discrepancy will not affect our conclusions. Hence, the San Diego mechanism is used for the remainder of the results.

Next, we explore the predicted CH LIF signal intensity variation with pressure. Figure 4.9 shows the predicted signal intensities as a function of equivalence ratio for a range of pressures with non-preheated reactants. Since this is the condition at which the laminar flame was imaged, the data from the validation experiment is appropriately scaled and plotted as well. Two immediate conclusions can be drawn from this plot. First, increasing pressure causes the LIF signal to drop rapidly. This can be attributed to several causes. The Chemkin results show that the mole fraction of CH in the flame is significantly lower at higher pressures. The CH number density also decreases, but not as much due to the higher density increase at higher pressure. Pressure, on the other hand, also sharply reduces the thickness of the CH layer. The combined influence of the above is to lower the total number of CH molecules available
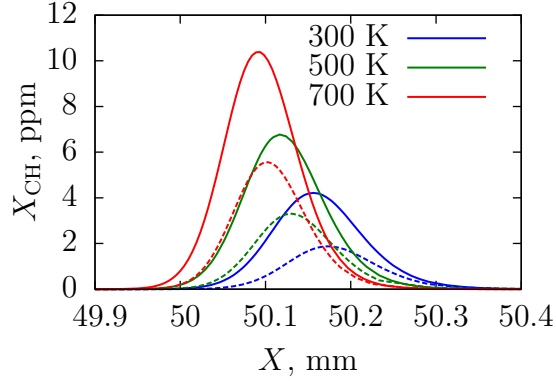
(a) *CH concentration*
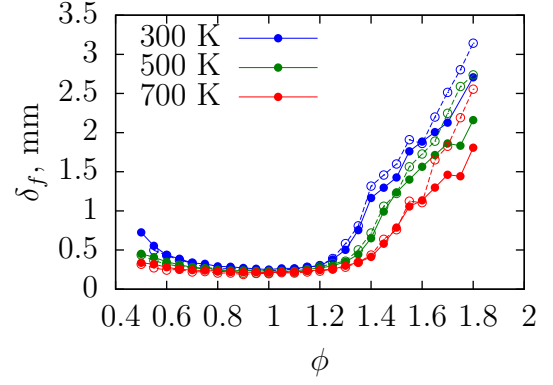
(b) *Flame thickness*
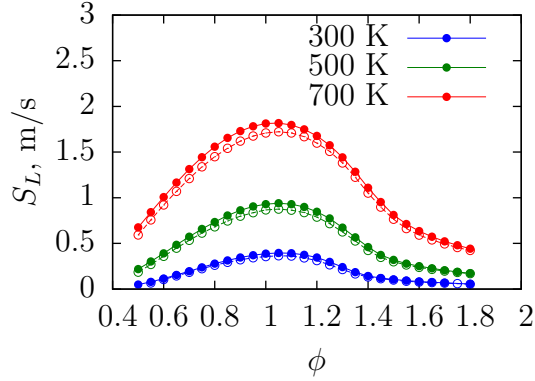
(c) *Laminar flame speed*
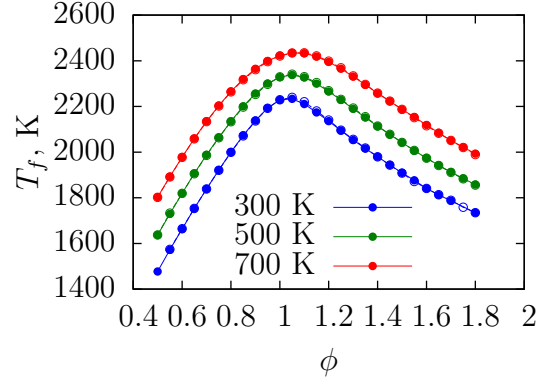
(d) *Flame temperature*

Figure 4.8: *The plots above compare various predicted parameters of an atmospheric pressure, laminar methane-air flame at three preheat temperatures from GRI Mech 3.0 and San Diego mechanisms. The results from GRI Mech 3.0 are plotted in solid lines, while those from the San Diego mechanism are plotted in dashed lines.*
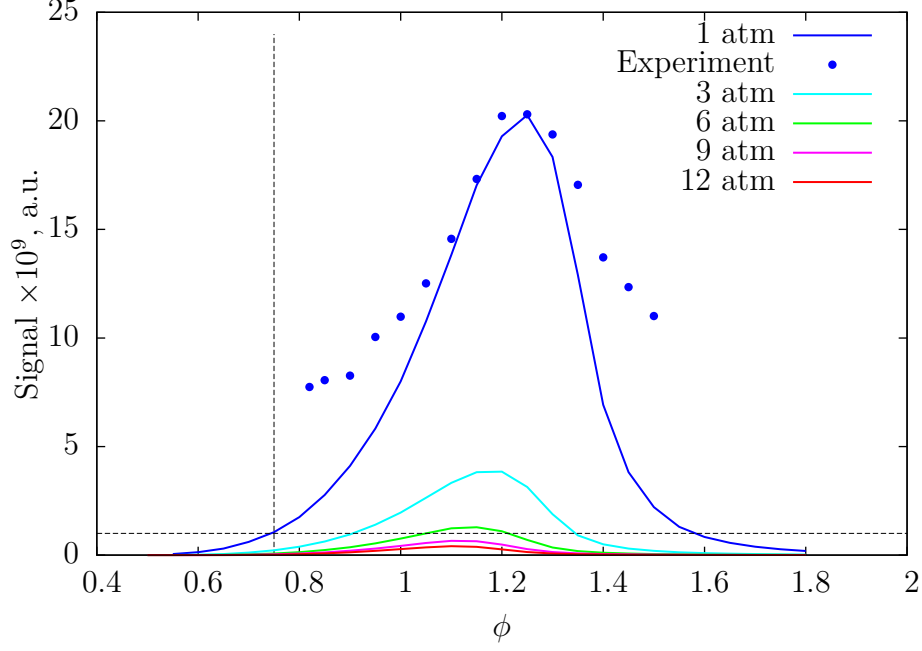
Figure 4.9: *The plot shows the calculated LIF signal for non-preheated (300 K) methane-air mixtures over a range of equivalence ratios and pressures. Results from an atmospheric pressure experiment are appropriately scaled and included.*

for excitation at high pressure, and hence, the LIF signal. The signal loss is further exacerbated by the quenching rate, which increases with pressure. Second, we can establish a threshold level for a detectable signal based on the validation experiment. The signal level for the lowest equivalence ratio case imaged serves as a good, if conservative, estimate of the minimum signal level needed. At $\phi = 0.8$, the predicted signal count works out to be 1.75×10^9. Based on this, we set the threshold at a value of 1×10^9. This threshold is indicated on the figure by dashed lines. Below this threshold, CH PLIF flame imaging will produce a poor signal-to-noise ratio that will make post-processing quite difficult.

In practice, the threshold could be lowered even further due to two reasons. First, even at the lowest equivalence ratio case tested in the laminar flame, the signal-to-noise ratio is more than sufficient to discern the flame sheet in instantaneous images. Second, the laser intensity used for this experiment (about 0.2 J/cm^2) could be increased by a factor of five, while still remaining in the linear LIF regime (though with

a concurrent decrease in size of the imaged region). Thus the threshold level used here (1×10^9) is a conservative estimate, which might reasonably be lowered by an order of magnitude (0.1×10^9). While this would extend the range of applicability described below, it does not qualitatively affect the conclusions in this section.

Using this minimum signal threshold, we can reinterpret Figure 4.9. When the pressure is increased to 3 atm, the flame cannot be imaged unless the equivalence ratio is between 0.9–1.3. At 6 atm, the range is even narrower and restricts the feasibility of this experiment to between 1.1–1.2. With no preheat, the flame cannot be imaged at 9 atm and above.

Increasing the preheat temperature to 500 K and plotting using a log scale, Figure 4.10 shows the effect of preheat is beneficial to CH PLIF. Raising the preheat temperature increases the CH LIF signal. At atmospheric pressure, the peak signal is nearly 50% higher. The range of equivalence ratios at which the flame can be imaged is now broader at all pressures. Lean flames at less than 0.7 can now be imaged at atmospheric pressure. Going up in pressure, near-stoichiometric rich flames at 9 atm can now be imaged.

Figure 4.11 shows this plot for a preheat temperature of 700 K. At this high preheat, ultra lean flames with equivalence ratios of 0.6 can be imaged at atmospheric pressure. Beyond 6 atm, the range of applicability of CH PLIF remains poor and is confined to near stochiometric and moderately rich flames.

4.4.1.2 Higher-Order Alkane Flames

Now, we turn our attention to higher-order alkane-air flames. Our interest in these fuels is motivated by two reasons. First, these are important fuels in their own right and are used in a number of combustion applications. Since the combustion reactions in these flames also follow a CH pathway, these flames could be imaged using CH PLIF. In addition, we want to explore the possibility of using small quantities of these
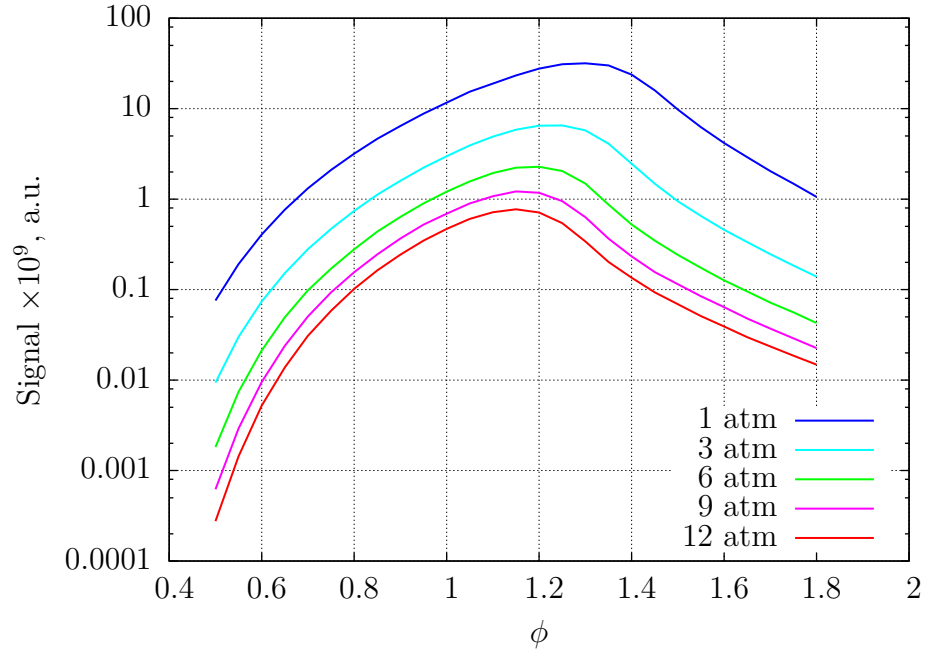
Figure 4.10: *The plot shows the calculated signal intensities for a methane-air flame with a preheat of 500 K. The ordinate 1×10^9 serves as a minimum threshold to get images with usable signal-to-noise ratios.*
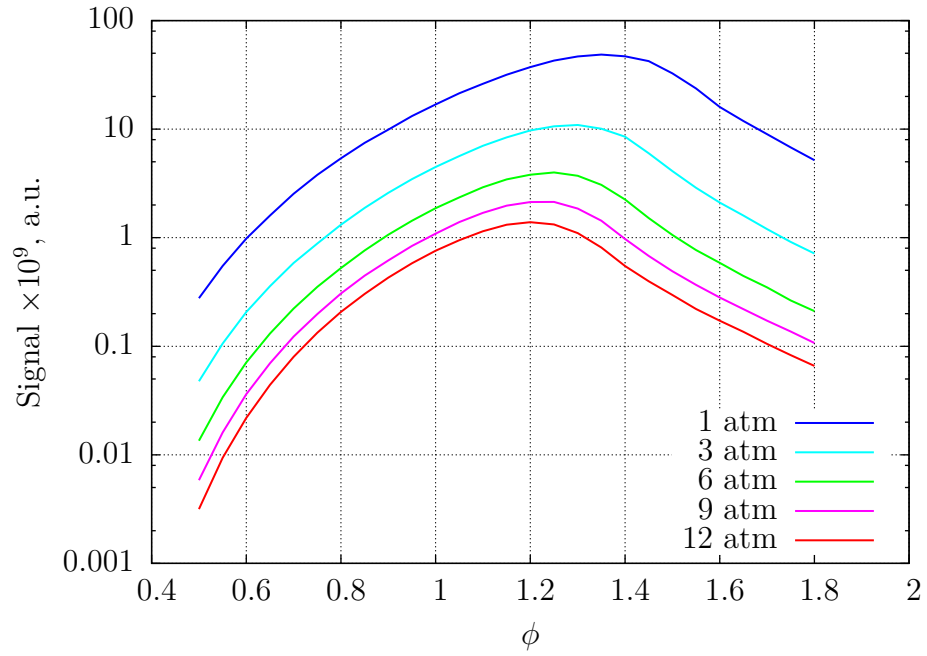
Figure 4.11: *This plot shows the calculated signal intensities for methane-air flames with a preheat of 700 K.*

fuels to mix with methane in order to boost the CH LIF signal. This could allow acquisition of flame images at leaner equivalence ratios at high pressure conditions.

We begin by considering the CH LIF signal from pure alkane-air mixtures burning at atmospheric conditions without preheat. Figure 4.12 shows the variation of the LIF signal with equivalence ratio for these mixtures. Again a signal level of 1×10^9 serves as a threshold for the feasibility of acquiring CH PLIF images of these flames. We can draw several conclusions from this plot. First, the range of equivalence ratios above the signal threshold is indeed wider for the higher alkanes (compared to methane), but not by much. Particularly, the differences between the three alkanes at the lean equivalence ratios is minimal. Most of the widening occurs at very rich equivalence ratios. Second, while the peak CH signal did increase when going from methane to ethane, a similar increase is not seen when going from ethane to propane. In fact, the San Diego mechanism actually predicts a slight fall in the peak signal. This lack of increase in the CH signal can be traced to the adiabatic flame temperature. Figure 4.13 plots the adiabatic flame temperature for these mixtures and shows that the increase in the flame temperature going from ethane to propane is minimal. While the CH signal does not correlate with the flame temperature at all conditions, it is strongly affected by it. Hence, the CH signal does not vary appreciably between the higher alkanes.

Since the CH signal in ethane- and propane-air flames are not much different from methane-air flames, adding small amounts of these alkanes should not have a very significant effect on the signal. This is borne out by Figure 4.14, which shows the signal variation for a 700 K preheat, atmospheric flame with and without higher-order alkane doping.
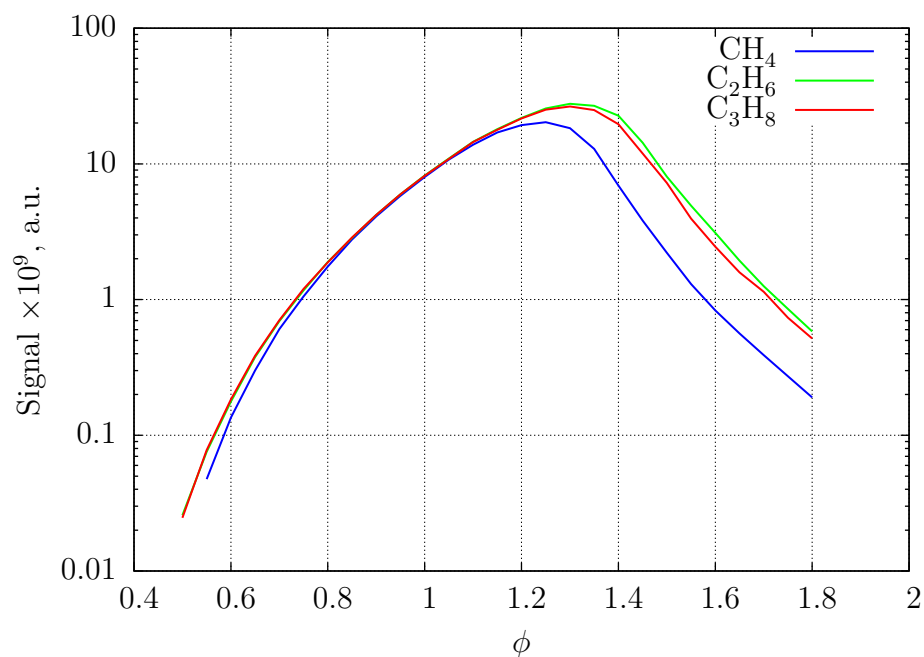
Figure 4.12: *The plot shows the calculated signal intensity from alkane-air flames burning at atmospheric pressure, without preheat (300 K). The signal levels at lean conditions are very similar. The ordinate 1×10^9 serves as the lower threshold for images with usable signal-to-noise ratios.*
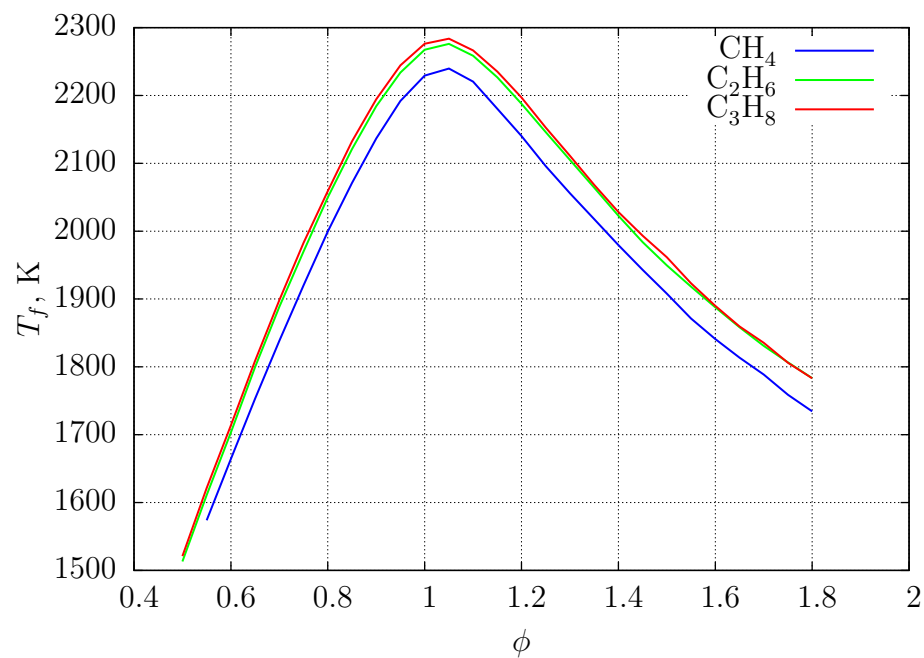
Figure 4.13: *The adiabatic flame temperature of alkane-air flames burning at 1 atm, with no preheat (300 K) is plotted against the equivalence ratio of the reactant mixture.*
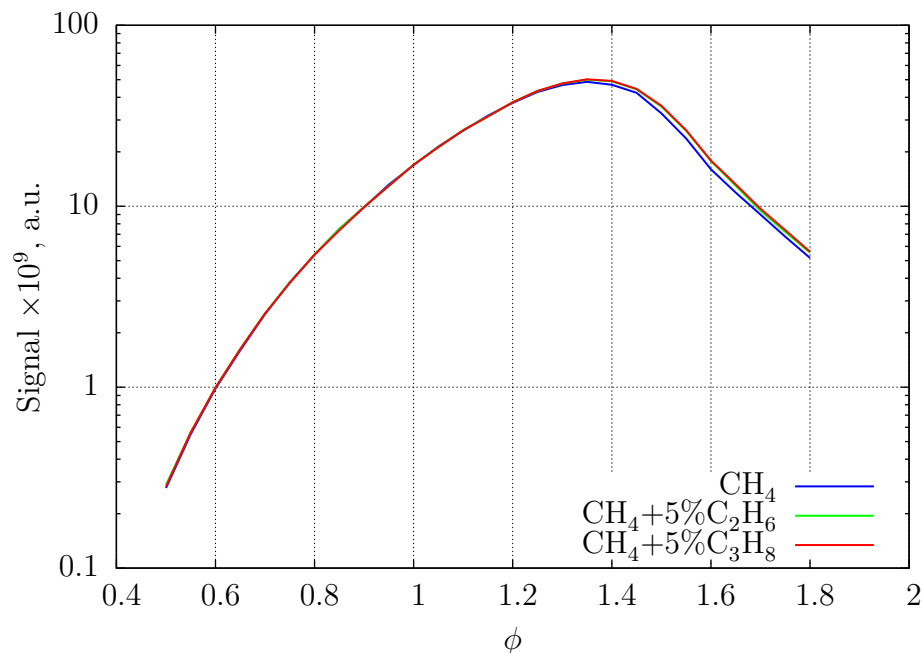
Figure 4.14: *The plot shows the effect of adding a small quantity of a higher-order alkane to a methane-air mixture at atmospheric pressure with a preheat of 700 K. The resultant boost to the CH LIF signal, particularly at lean equivalence ratios, is negligible.*

4.4.1.3 Syngas Flames

Syngas (mixtures of CO and H_2) does not follow a CH pathway when oxidized in air and hence is unsuitable for investigating with CH PLIF. As a result, most syngas flames are investigated using OH PLIF, rather than CH PLIF. However, since syngases are an important emerging class of fuels, it would be interesting to test the feasibility of using CH PLIF if they are doped with a small amount of alkanes to provide a CH pathway. In addition, some applications being investigated by industry include mixing syngas and methane fuels.

Figure 4.15 shows the signal levels in various non-preheated, atmospheric pressure syngas mixtures doped with 5% methane. The results are quite promising as they indicate that with a high enough H_2 concentration, syngas flames as lean as 0.8 can be imaged above our signal threshold. Increasing the preheat temperature to 700 K, Figure 4.16 extends this range to an equivalence ratio of 0.6. Using a higher order
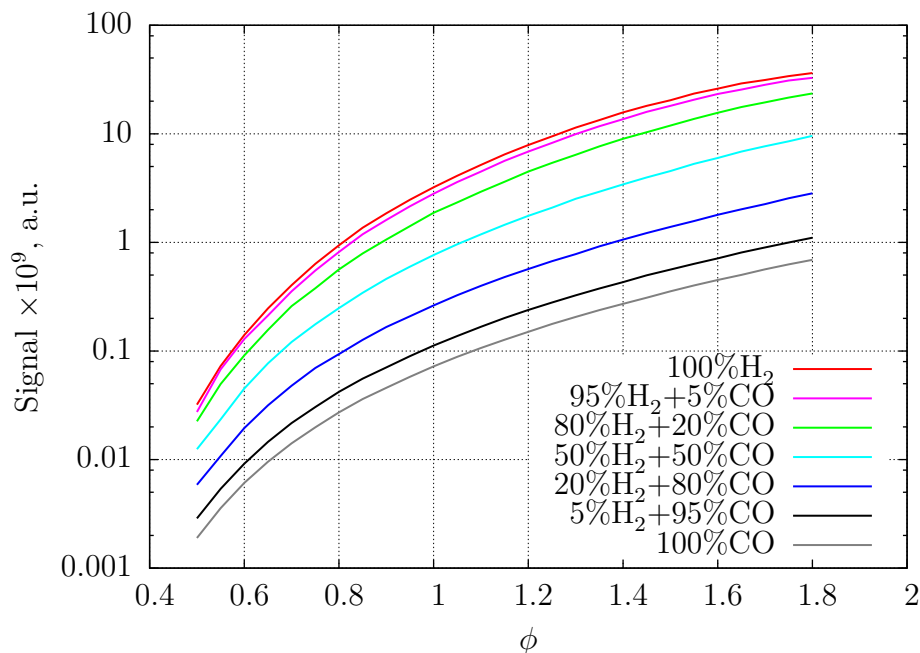
Figure 4.15: *The plot shows the effect of doping various syngas mixtures at atmospheric pressure and no preheat (300 K) with a small amount (5%) of methane. The ordinate 1×10^9 serves as the lower threshold for the signal.*

alkane in place of methane lowers this value further, but not significantly.

Consider the predicted values for the CH LIF signal from a H_2-CH_4-air mixture ("100% H_2") in Figure 4.16 in comparison to the LIF signals from a pure methane-air mixture. It is clear that the addition of a small quantity of methane to hydrogen results in a disproportionate increase in the CH LIF signal. To investigate this further, the percentage of methane used to dope a H_2-air reactant mixture was varied from 0% (pure H_2) to 100% (pure CH_4). The predicted signal levels for these mixtures are shown in Figure 4.17.

The CH LIF signal increases rapidly with methane addition, reaching a maximum near 20% CH_4 addition. It is interesting to note that this maximum signal is higher than the signal from pure CH_4. The rapid increase may be due to the presence of H_2 species in the reacting environment enhancing the CH4 reaction pathways that produce CH compared to other pathways. At higher proportions of CH_4, the signal gradually diminishes due to the more efficient quenching of the LIF signal by CH_4
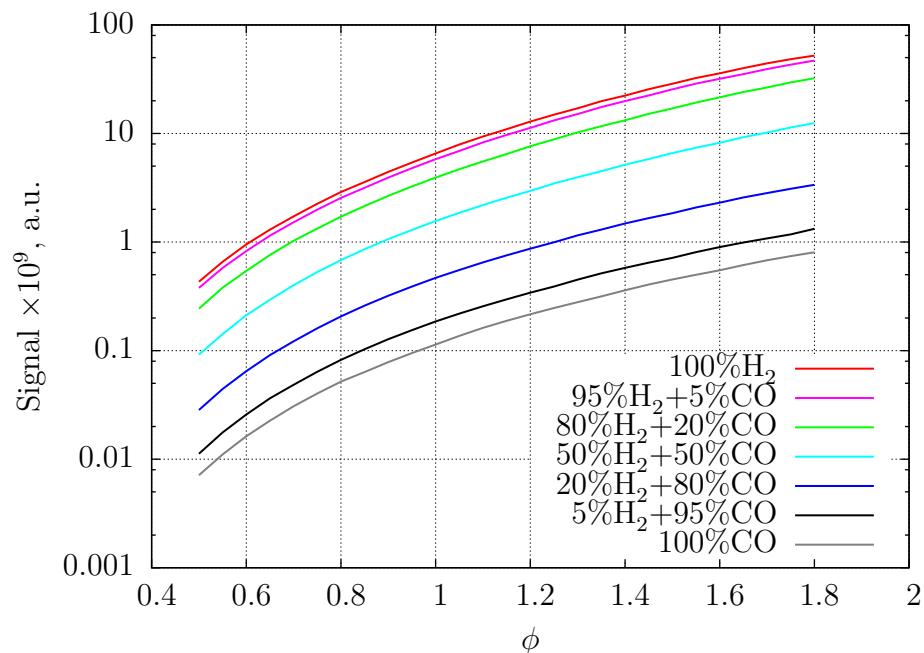
Figure 4.16: *The plot shows the calculated CH LIF signal from various syngas mixtures that have been doped with 5% methane at atmospheric pressure. The reactants have been preheated to 700 K.*
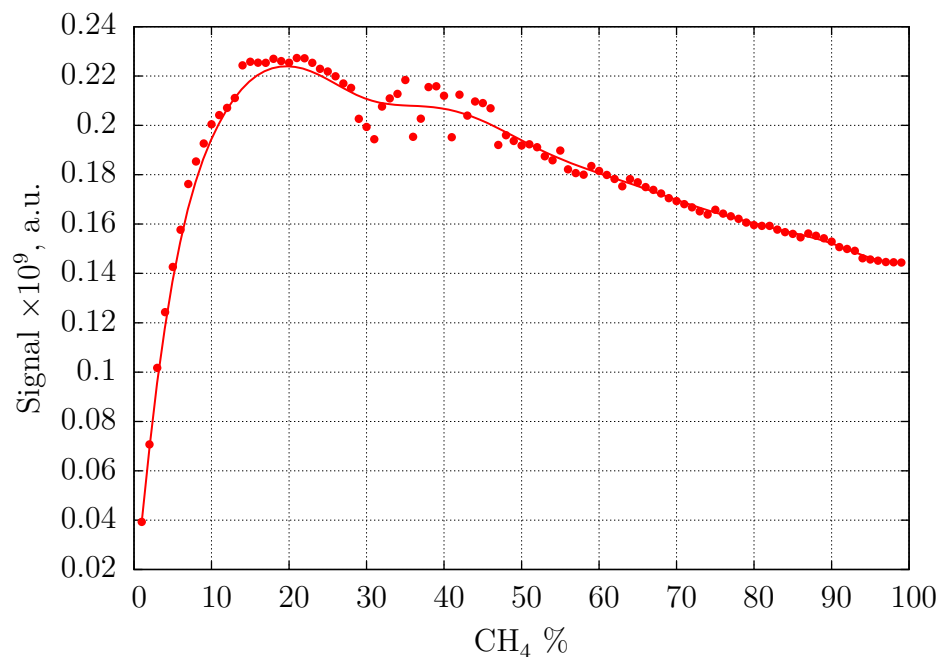
Figure 4.17: *The LIF signal from a pure H_2-air reactant mixture is shown as a function of increasing CH_4 percentage. The reactants are initially at 300 K and 1 atm. The equivalence ratio of the reactant mixture is held fixed at 0.6 for all cases. The slight scatter in the data points in the 30–50% CH_4 range is attributed to convergence issues in Chemkin.*

oxidation products like CO_2 and CO.

While these results indicate the feasibility of using a spatially precise flame imaging technique like CH PLIF to study syngas flames, the addition of a small quantity of alkane can substantially change the properties of the flame. While the adiabatic flame temperature for a pure hydrogen fuel only decreases by 40 K due to the methane addition, peak flame speeds are reduced by almost 20%. This may limit the applicability of CH PLIF to study these flames.

4.4.2 Strained Flames

In order to study the effect of strain rate on the LIF signal, a non-preheated, atmospheric pressure, laminar methane-air flame is simulated in an opposed flow configuration. The flow rate is slowly increased until extinction occurs. The separation between the two flow inlets in the simulation is 2 cm. The system is solved using the Opposed flow flame reactor model in Chemkin. The simulation is carried out for two equivalence ratios and the results are plotted in Figure 4.18.

The LIF signal increases with stretch, by about 10%, until close to the extinction strain. Very close to extinction, the CH LIF signals decreases slightly. This behavior mirrors the variation of the flame temperature for $Le < 1$ flows where increasing stretch results in an elevated flame temperature. Though not indicated in the figure, the signal would decrease precipitously (to zero on a steady-state basis) beyond the extinction limit. These results suggest that stretch should have little effect on the (spatially integrated) CH LIF signal until very close to the point where extinction begins to occur.

4.4.3 Flame Temperature Correlation

A possible correlation between LIF signal and flame temperature was suggested in Section 4.4.1.2, where it was pointed out that the marginal increase in the LIF signal
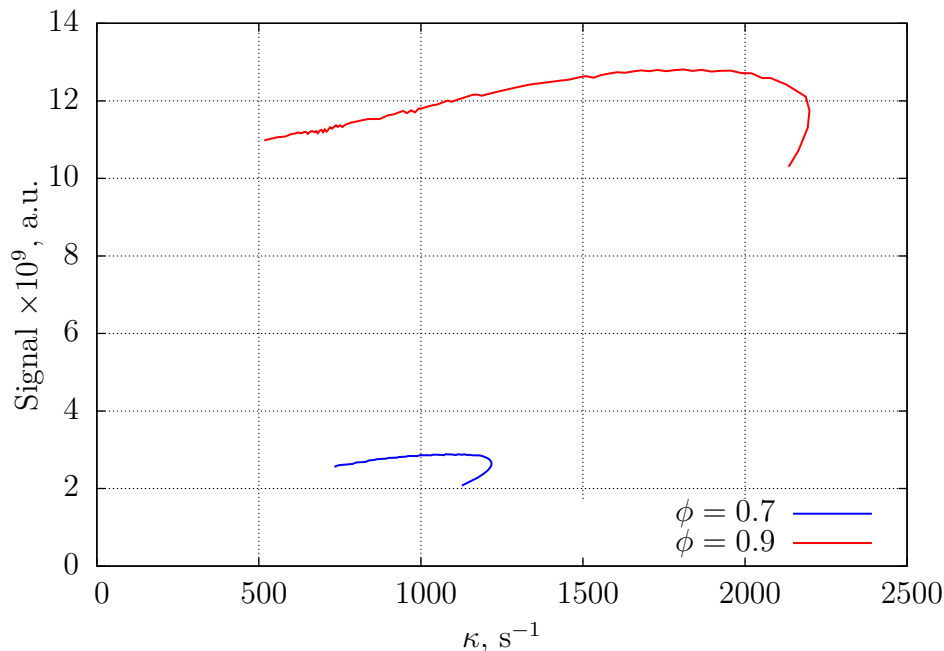
Figure 4.18: *The plot shows the calculated CH LIF signal from a strained, laminar, methane-air flame at atmospheric pressure. The signal is calculated from Chemkin simulations using the Opposed flow flame reactor model.*

between methane and the higher order alkanes mirrored the change in flame temperature. In this section, we examine this correlation in greater detail.

Figure 4.19 shows the LIF signal values predicted for data sets simulated at atmospheric pressure conditions. The LIF signals are plotted against the adiabatic flame temperature for unstrained, laminar, methane-air flames at three preheat temperatures. In each case, the signal increases exponentially with flame temperature for lean conditions. The flame temperature peaks at near-stoichiometric conditions, but the signal levels continue to rise, forming a second "upper" branch for rich mixtures. After the CH signal peaks, both the flame temperature and the LIF signal decrease for the rich cases.

So for lean mixtures in the unstrained cases, the signal is primarily a function of flame temperature. The CH signal is nearly the same whether the mixture is lean with some level of preheat or even leaner with more preheating, as long as both have the same adiabatic flame temperature. A similar behavior holds for the rich
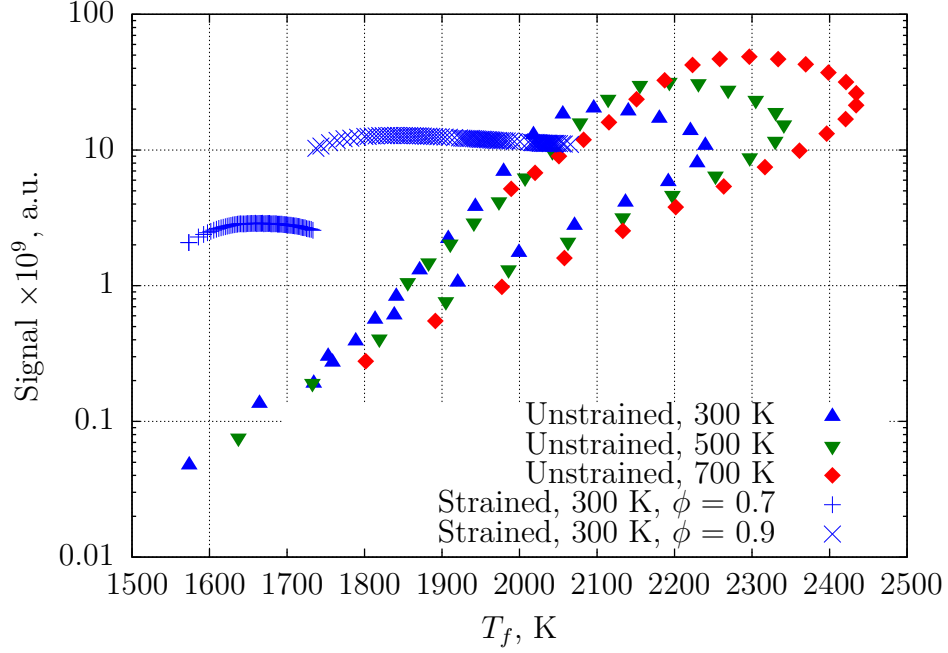
Figure 4.19: *The LIF signal levels for several data sets at 1 atm are plotted against the respective flame temperatures. In case of strained flames, the maximum flame temperature is used.*

branch, except for near-stoichiometric mixtures. For near stoichiometric mixtures, the correlation is rather poor between the peak flame temperature ($\phi \approx 1.0$) and the peak LIF signal ($\phi \approx 1.2$).

The flame temperature can also be varied by changing the strain on the flame. Therefore Figure 4.19 also includes LIF signals from the strained (opposed flow) flame cases discussed earlier. For these cases, the flame need not be adiabatic along a streamline. As a result, the signals are plotted against the maximum flame temperature achieved in the calculation. Although the maximum flame temperature decreases as the strain rate is increased, the signal levels remain relatively constant. Notably, when the $\phi = 0.9$ flame is strained close to extinction ($T \approx 1800$ K), the signal levels are not comparable to the lesser strained $\phi = 0.9$ flame with nearly the same maximum flame temperature.

Based on these data sets, it may be concluded that while the LIF signal can be expected to increase with higher flame temperatures as a *rule-of-thumb*, the correlation

is not perfect and does not extend to strained flames.

4.5 Summary of Results

The following is a summary of the key results from this chapter.

1. The optimal excitation tuning of the CH PLIF imaging system was determined and demonstrated on a simple, laminar Bunsen flame.

2. Details of simplifications to the signal intensity model from Chapter 2 based on reported experimental observations were outlined.

3. The experimental results from a laminar methane-air Bunsen flame at atmospheric pressure were compared to modeling results, which behave in much the same manner with equivalence ratio.

4. The model was used to study the variation of the LIF signal with pressure, temperature and equivalence ratio for a host of reactant mixtures.

5. In general, increasing the flame temperature enhances the CH LIF signal, while increasing the combustor pressure decreases it.

6. Hydrogen-rich syngas flames can be imaged with CH PLIF if the reactants are doped with a small amount of an alkane. However, this also causes noticeable changes in the flame speed of the reactant mixture.

7. Strained flames produce a slightly higher LIF signal as long as the strain rate is not close to extinction.

8. The LIF signal for unstrained flames is a strong function of flame temperature, nearly exponential, though it is not correlated to temperature alone.

CHAPTER 5

LSB FLAME CHARACTERISTICS

Chapter 2 introduced the salient features of the LSB flow field and discussed the mechanisms that enable the LSB to stabilize a flame. Four flow parameters were introduced that sufficiently describe an operating condition of the LSB—the combustor pressure, p, the preheat temperature, T, the reference velocity, U_0, and the equivalence ratio of the premixed reactants, ϕ. The angle of the swirler vanes, α—a geometric parameter—was also identified as a variable of interest. The effect of varying these parameters on the flame characteristics constitutes the subject of this chapter. The LSB flame was characterized by its location, its shape and its structure. The first two of these are quantified by the flame standoff distance, X_f, and the flame cone angle, θ_f respectively.

In the same chapter, the existing theories explaining LSB operation were outlined. These theories were developed based on observations of the LSB flame and flow field in experiments conducted at atmospheric pressure, with low velocity, non-preheated reactants. Restating one objective of this thesis, the goal is to reexamine the validity of these theories at conditions closer to those at which gas turbines operate.

Finally, Chapter 2 examined key parameters that affect each of the flame characteristics, illustrated by the case of varying reference velocity. The flame location and shape were seen to be controlled by factors affecting the axial velocity profile and the turbulent flame speed. A Borghi diagram based on turbulence and laminar flame properties was introduced to designate the regime of premixed turbulent combustion that best describes the flame structure.

The following sections examine the results of experimental investigation of the flame characteristics conducted at high preheat and high pressure conditions.

5.1 Effect of Reference Velocity

Section 2.1.4.1 explored how changing the reference velocity is not expected to affect the flame location or the flame shape as the balance between the local reactant velocity and the turbulent flame speed remains unaffected. This was further borne out by Equation 2.4 which outlines a simple model for the turbulent flame speed as a linear function of u and hence, U_0. Combined with the self-similar velocity field in the LSB, this predicted that the flame shape and location will be constant over a wide range of operating conditions. Cheng et al.[34] reported no significant deviation from this model over the range of conditions at which they tested the LSB design. It is worth repeating that these experiments were confined to low flow velocities at atmospheric pressure, non-preheated conditions.

In typical gas turbine applications, the reference velocity is not generally variable with engine loading. Hence, the motivation for studying its effect on the flame characteristics arises from the fact that the reference velocity is a design parameter and its effect on the flame has implications for the design of future LSB-based gas turbine engines. If the atmospheric pressure model holds at high pressure conditions and the reference velocity has no discernible effect on the flame shape and location, such behavior is desirable from the point of view of a gas turbine designer as it would simplify models for heat transfer and combustor length.

In order to verify the validity of this model at high pressure conditions in the presence of substantial preheat, the LSB was operated at a pressure of 6 atm and the reference velocity was varied from 10 to 40 m/s. For these tests, the $S_{37°}$ swirler was used. In a parallel series of tests, the $S_{45°}$ swirler was tested at a pressure of 3 atm at reference velocities of 40 and 80 m/s. The preheat temperature for these tests was about 500 K. The measured and calculated flow parameters for these conditions are presented in Table 5.1. The location of the flame was measured from

Table 5.1: *The following table presents the cases at which the LSB configurations were tested to study the effects of reference velocity. Chemiluminescence experiments were conducted on Configuration A, while CH PLIF experiments were conducted on Configuration B.*

Experiment	p	T	ϕ	U_0
	atm	K		m/s
Chemiluminescence				
	6.04	525	0.57 ± 0.02	37.3
	6.03	534	0.55 ± 0.07	20.1
	6.19	524	0.55 ± 0.07	18.9
	6.19	493	0.51 ± 0.16	11.7
	3.01	485	0.57 ± 0.04	36.7
	3.02	523	0.57 ± 0.02	79.5
CH PLIF				
	1.0	315	0.90	21
	1.0	443	0.90	40

CH* chemiluminescence images and the results are presented in Figure 5.1.

There is essentially no systematic variation in the flame standoff distance or the flame angle for the low velocity, $S_{37°}$ tests. This is in line with Equation 2.5's prediction and confirms its applicability even at elevated pressure and preheat conditions.

When the $S_{45°}$ swirler was tested at higher reference velocities, however, the flame location shifted downstream sharply. This indicates potential limitations to the simple flame stabilization model that may not predict the behavior of the LSB flame at elevated pressures and temperatures, particularly at high reference velocities.

A possible explanation for this observation can be gleaned from considering the effect that increasing the reference velocity has on the turbulent combustion regime in which the LSB combustor operates. Previous studies have operated the LSB in regimes where Equation 2.4 predicts the variation of the turbulent flame speed with u with reasonably fidelity. The arguments behind the formulation of Equation 2.4 assume that a turbulent flame can be treated as a distorted/wrinkled laminar flame in
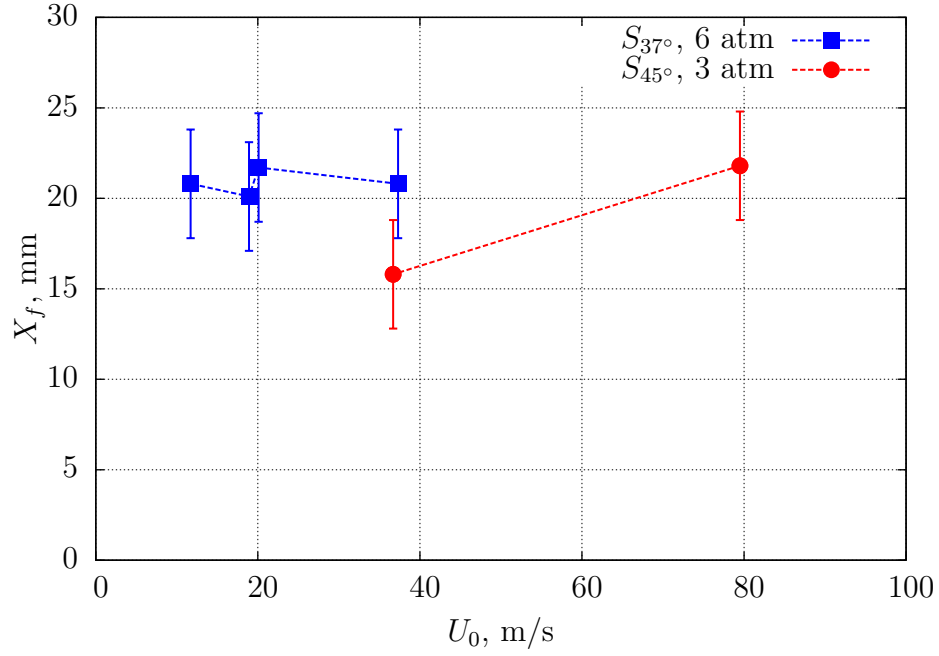
(a) *Flame standoff distance as a function of the reference velocity*
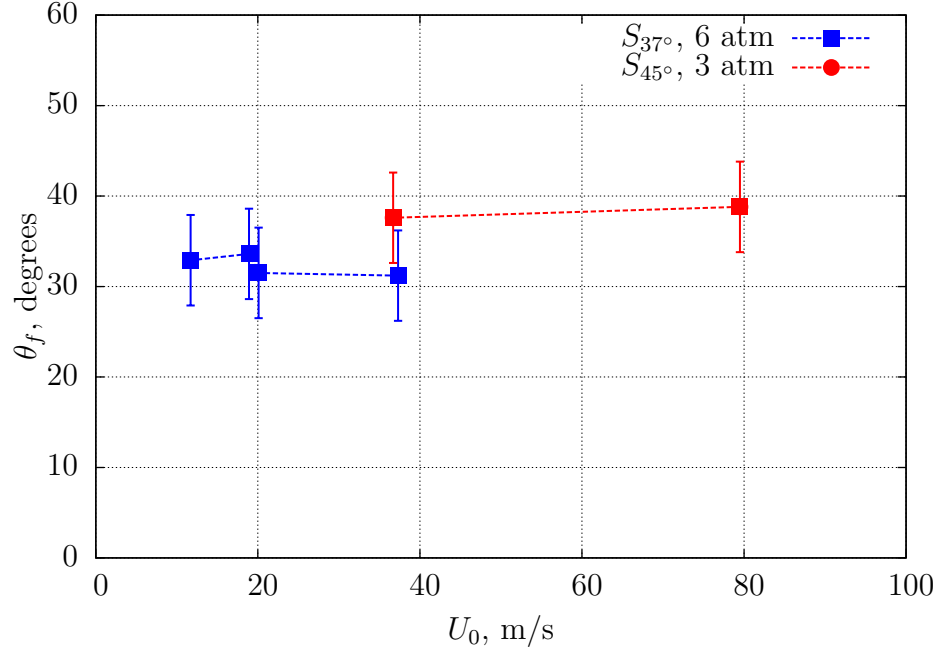
(b) *Flame cone angle as a function of the reference velocity*

Figure 5.1: *The plots show the effect of changing the reference velocity on the flame location and flame shape. The blue curves are from tests conducted using the $S_{37°}$ swirler at 6 atm, while the red curves are from tests using the $S_{45°}$ swirler at 3 atm. An uncertainty of ± 3 mm and $\pm 5°$ are estimated for standoff distance and flame angle calculations respectively.*

the presence of large scale, low intensity turbulence. This assumption is largely true in the wrinkled flame regime and may even be extended apply to a mildly corrugated flame. However, as we approach large $\dfrac{u}{S_L}$ values and operate in the thin reaction zone—where most gas turbine combustors operate—the flame bears little resemblance to a wrinkled laminar sheet. Since increasing the reference velocity (and thus u) traverses the operating point along the vertical axis of the Borghi diagram, it can cause the turbulent combustion regime to change at high values of $\dfrac{u}{S_L}$, resulting in the "bending effect" in the $\dfrac{S_T}{S_L}$ vs $\dfrac{u}{S_L}$ diagram.[98, 99]

One way to ascertain the regimes in which the LSB is operated is to image the flame sheet and observe the flame structure. To that end, the LSB (Configuration B) was tested at atmospheric pressure with preheat temperatures ranging from 300 to 440 K. Two of these conditions are at temperatures relevant to this discussion and their operating parameters are presented in Table 5.1. In order to prevent flame blow off, the equivalence ratio had to be increased to 0.9. The resulting flame illuminated by an 80 mm tall, 250 μm thick laser sheet from the alexandrite laser and imaged using the PI-MAX 512×512 intensified camera equipped with a 50 mm, f/1.4 lens. The camera was gated to 300 ns centered on the 70 ns laser pulse. The laser was operated at 10 Hz and the pulse energy was measured to be about 14 mJ for the low velocity case and about 17 mJ for the high velocity case. A sample frame from each dataset is shown in Figure 5.2.

Both the low and high velocity cases show an essentially unbroken flame sheet that is characterized by wrinkles. This is consistent with the operating regime being in the wrinkled laminar flame region of the Borghi diagram. The level of wrinkling in the flame sheet is representative of the increase in the flame area and hence the turbulent flame speed. This can be quantified by detecting the edges of intensity in these images and measuring the integrated length along the edges. A simple implementation of this can be done by counting the number of pixels along the intensity edges. The edge

(a) $U_0 = 21$ m/s

(b) $U_0 = 40$ m/s

(c) Intensity edges

(d) Intensity edges

(e) $\mu = 364$; $\sigma = 167$

(f) $\mu = 463$; $\sigma = 187$
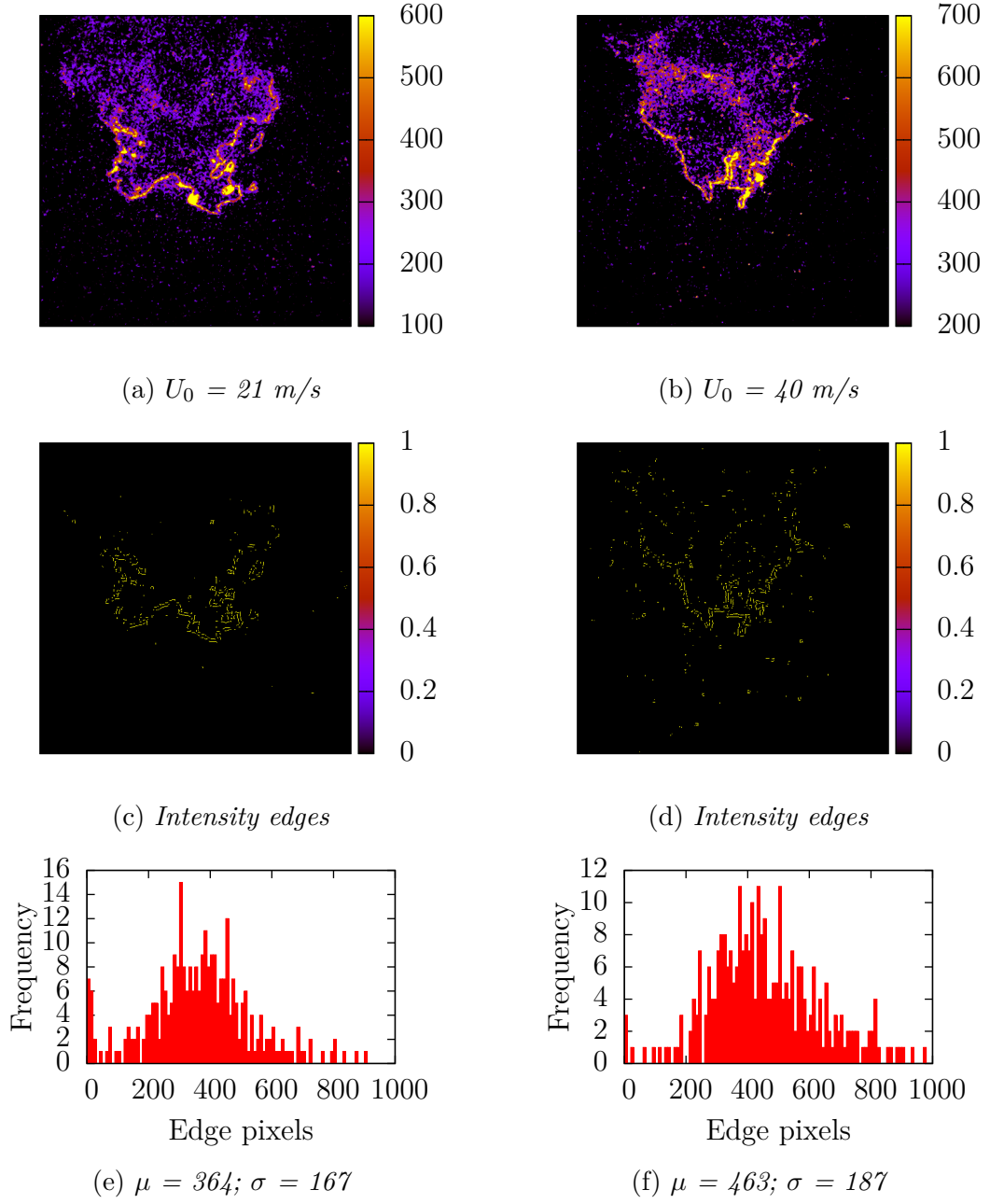
Figure 5.2: *The sequence of images on the left and the right pertain to the low and high velocity cases respectively. Each instantaneous frame of PLIF data is processed to detect edges and the statistics of the edge pixels from 300 such frames in the central quarter of the image are plotted as a histogram.*

detection algorithm detects two sharp intensity gradients along the flame sheet—one on the reactants side and one on the product side. Consequently, the flame sheet get doubly counted but this does not affect the statistics as twice the number of edge pixels are counted from all the frames.

The flame sheet also exhibits up-down movement from frame to frame, in addition to wrinkling. If the statistics are gathered over the entire frame, the up-down motion pollutes the data and the statistics can no longer be attributed to the wrinkling of the flame sheet alone. To overcome this, edge pixels are counted only over a quarter of the image width, centered on the average flame axis. The detected edges and histograms of the edge pixels are also presented in Figure 5.2.

Figure 5.3 shows three consecutive frames each from the low velocity, low preheat case and the high velocity, high preheat case. The level of wrinkling is predictably higher for the high velocity, high preheat case. The instances of disjoint packets of flame are also higher for this case. This can also be seen in the histogram in Figure 5.2 where the average number of detected edges in the region of interest is higher by more than 25% for the high velocity case. The higher instances of finding disjoint packets of flame in high velocity, high preheat case, in particular indicates that the operating point is approaching the boundary between the laminar wrinkled flame regime and the corrugated flame regime.

While the two tested LSB configurations A and B are somewhat different geometries, the mechanisms affecting the flame structure at the stabilization point are very similar. Further, the size of the largest eddies in the flow—the integral length scale—should be dominated by the geometry of the swirler which is very similar for both configurations. As a result, we may even place the operating conditions on the same Borghi diagram and apply what we learnt from the CH PLIF imaging tests to the chemiluminescence cases. In spite of the leaner equivalence ratio, the effect of the elevated combustor pressure is expected to diminish both the flame speed, S_L, and

(a) *Frame #0*

(b) *Frame #0*

(c) *Frame #1*

(d) *Frame #1*

(e) *Frame #2*

(f) *Frame #2*
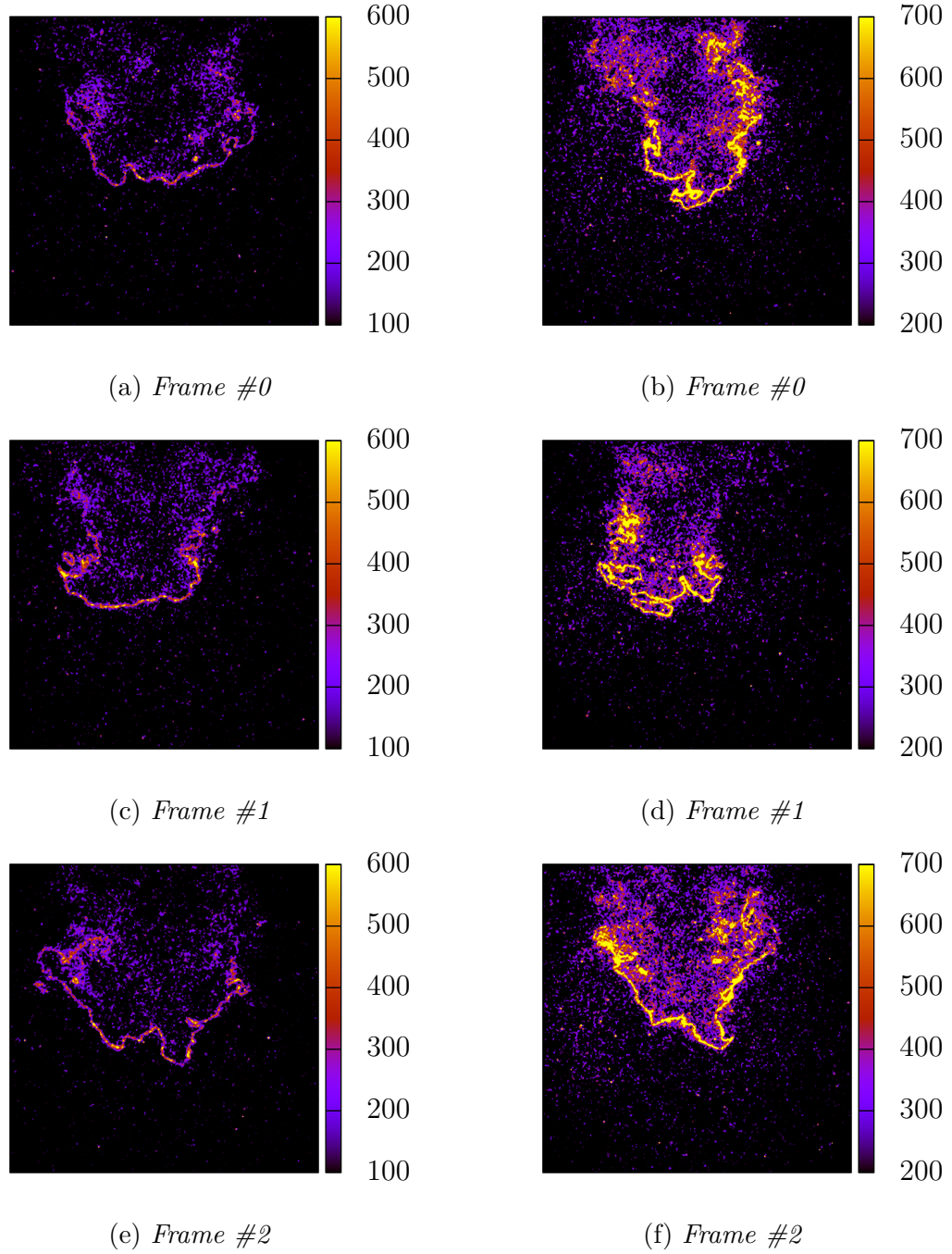
Figure 5.3: *The sequence of instantaneous images on the left are taken at 21 m/s at 315 K. The images on the right are acquired at 40 m/s with a preheat of 443 K. The flame sheet on the right is noticeably more wrinkled.*

the flame thickness, δ_f, placing the operating regime higher (and to the right) on the Borghi diagram. At a sufficiently large reference velocity, the operating point can transition from the corrugated flame regime into the broken flamelets regime. Such a transition would not have been possible for a similar increase in reference velocity at atmospheric pressure conditions as the corresponding $\dfrac{u}{S_L}$ values would have been too low. Transitioning into the broken flamelets regime would cause S_T to increase at a reduced rate with u and U_0, resulting in the observed downstream shift of the high pressure LSB flame at high reference velocities.

5.2 Effect of Preheat Temperature

In order to explore the effect of increasing the preheat temperature on the flame location, shape and structure, we begin by mapping the velocity field of the combustor using Laser Doppler Velocimetry (LDV). The conditions were chosen to study the effect of increasing the preheat temperature on both reacting and non-reacting LSB flow fields. Further, the study includes both low and high reference velocity cases. The relevant flow parameters relating to these tests are presented in Table 5.2. The test cases are named CN (Cold, Non-reacting), HN (Hot, Non-reacting) and HR (Hot, Reacting) based on their preheat and presence of a flame. All LDV tests were limited to atmospheric pressure conditions. Implementing the LDV technique at elevated pressures proved difficult due to beam steering issues, coupled with impractical turnaround times between the successive runs that would be required to obtain sufficient LDV data points for analysis.

The normalized centerline mean axial velocity profiles for the three cases are presented in Figure 5.4. The abscissa represents the distance from the virtual origin as defined in Section 2.1.2.

The results show that increasing the preheat temperature causes the normalized velocity slope to increase. As noted in Chapter 2, Cheng et al.[34] reported that this

Table 5.2: *The following table lists the conditions at which the LSB flow field was mapped using LDV. These experiments were performed on Configuration A.*

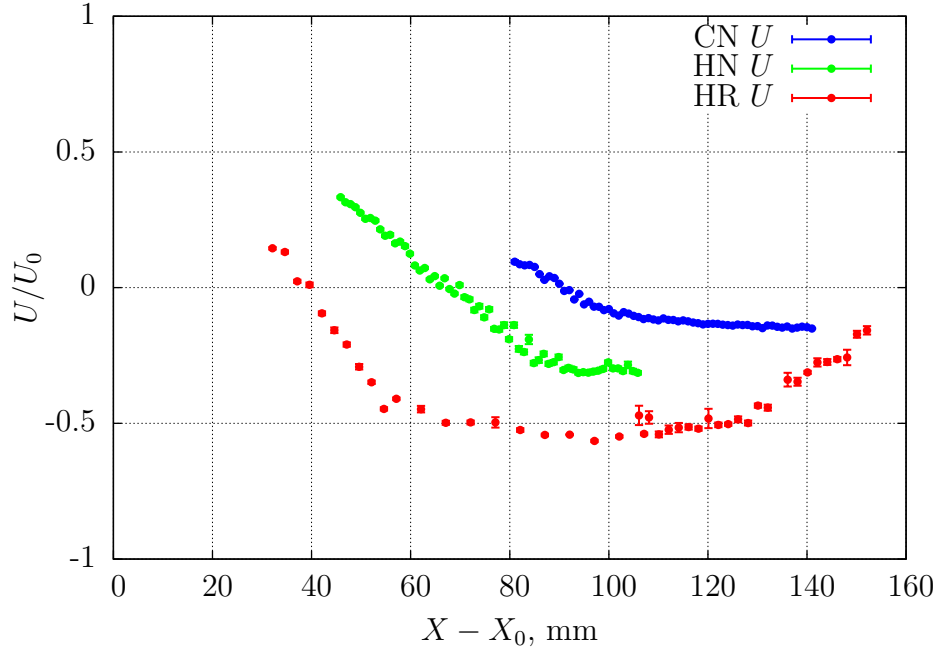| Case | T | ϕ | U_0 | Re |
	K		m/s	
Cold, Non-reacting (CN)	300	-	30	72700
Hot, Non-reacting (HN)	500	-	75	75200
Hot, Reacting (HR)	465	0.55	30	39500

Figure 5.4: *The plot shows results from LDV mapping of the flow field in the LSB. Mean axial velocity profiles are shown for* cold, hot, *and* reacting *flow fields. The velocities are normalized by the reference velocity, while the abscissa is shifted to align the virtual origins of the profiles.*

slope is unaffected by the Reynolds number, Re, of the operating condition. The results in Figure 5.4 however, show that even though the cases CN and HN have similar Re, their mean velocity profiles have very different slopes. This indicates that the mean axial stretch in the near field of the LSB flow field is a stronger function of the preheat temperature than Re.

The preheat temperature impacts the reacting flow field in the LSB in two ways. First, a higher preheat temperature increases the kinematic viscosity of the flow. The mechanism that transports the axial momentum in the radial direction and causes the flow to diverge is driven by viscous effects. Enhanced viscous effects will result in a steeper decrease in the axial velocity. Simultaneously, this causes an increased production of turbulent kinetic energy. Second, global reaction rates increase with temperature, causing the laminar flame speed to increase. The net result of the increased turbulence and laminar flame speed is that the turbulent flame propagates faster. As a result of the steeper velocity decay and the increased turbulent flame speed, the flame will be expected to stabilize closer to the inlet of the LSB.

Even assuming that S_T is constant, these results suggest that at higher preheat temperatures, the flame would stabilize closer to the dump plane because of the faster reactant velocity decay. In fact, the faster velocity decay produces a higher u and would increase S_T, further causing the flame standoff location to shift upstream. This affects the stability of the flame in two ways. First, the flame is closer to the inlet, resulting in more effective heat transfer from the flame zone into the reactants. Second, the steeper profiles of U and S_T limit any movement of the flame in response to perturbations in the local flow field. These two characteristics of the preheated flame lead to an intuitive result—the LSB flame behaves more stably at high preheat conditions.

Next, we consider how the flame cone angle is affected by increasing the preheat temperature of the incoming reactants. None of the data sets cover two otherwise
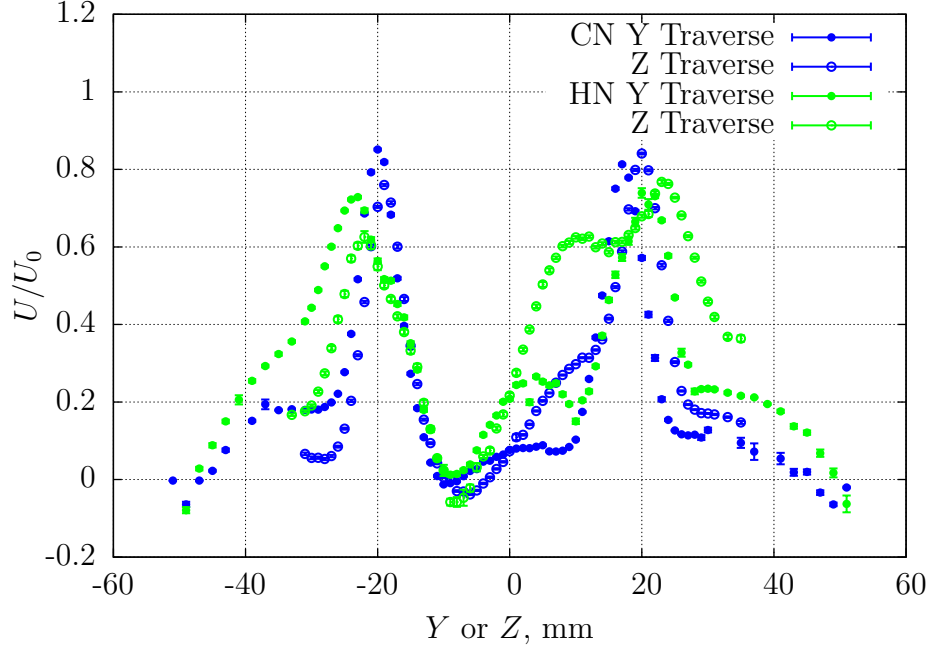
Figure 5.5: *The plot shows LDV data from two orthogonal traverses (along Y and Z axes) performed across the LSB combustor. Mean axial velocity is presented for cold and hot cases (both non-reacting) to highlight the effect of preheat on the mean axial velocity profile through the shear layer. The traverses are performed 15 mm downstream of the inlet and use the $S_{45°}$ swirler in Configuration A.*

identical operating conditions, but at different preheat temperatures. As a result, the effect must be postulated using data showing the combined effect of increasing reference velocity and preheat temperature. Figure 5.5 shows the profiles of mean axial velocity measured 15 mm downstream of the inlet using LDV. These measurements are taken from two orthogonal traverses across the flow field and show the profiles for the CN and HN cases. The results show that the peak mean axial velocity across the shear layer remains the same regardless of velocity or temperature. However, the thickness of the shear layer has increased.

The angle of the flame cone is decided by the ratio of the mean velocity in the shear layer and the local turbulent speed of the flame. We can use this relation and explore the propagation of a change in the parameters as follows.

$$U \sin \theta_f = S_T$$

$$\therefore \frac{\delta \sin \theta_f}{\sin \theta_f} = \frac{\delta S_T}{S_T} - \frac{\delta U}{U} \qquad (5.1)$$

This shows the competing effects of the S_T and U in the shear layer. Since our LDV data indicates that the peak mean axial velocity actually decreases slightly, while the turbulent flame speed would continue to increase with preheat temperature. The net result of increasing the preheat temperature would thus cause the flame angle to increase.

Finally, we return to the Borghi diagram to consider the effect of a higher preheat temperature on the flame structure. On the Y-axis, the exponential dependence of S_L on temperature will decrease the ordinate of the operating point, while on the X-axis, a slight decrease in the flame thickness will move the point to the right. Figure 5.6 illustrates the direction of movement of such an operating point. The down-and-right movement of the operating point drives the flame regime away from broken flamelets and closer towards wrinkled/laminar flames.

5.3 Effect of Swirl

As described in Chapter 2, the amount of swirl in the LSB flow field is quantified by a swirl number as defined in Equation 2.1. Even though there is no tangential momentum in the core of the LSB flow field where the flame is stabilized, the swirl still exerts influence on the flame characteristics.

The LSB utilizes swirl to enhance the divergence of the flow near the inlet. Consequently, an increased swirl number results in a sharper deceleration of the reactants and a more upstream stabilization point for the turbulent flame. This is corroborated by past research[19,100] which reporter shorter, wider (higher flame cone angle) flames
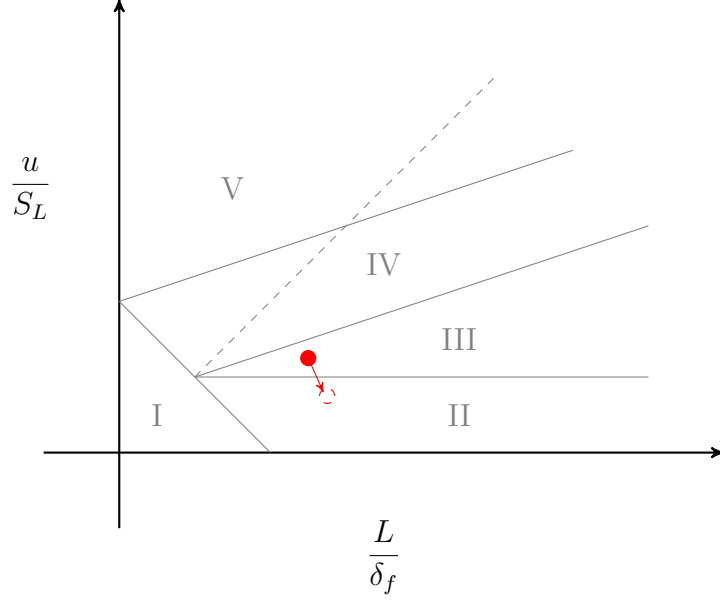
Figure 5.6: *The schematic is a reproduction of the Borghi diagram from Figure 2.4. The response of an operating point to increasing preheat temperature is schematically illustrated. If the initial operating point was in the corrugated flame regime, it would tend towards the laminar flame regime as the flame speed increases and the flame thickness slightly decreases.*

when the amount of swirl in a combustor was increased.

The results from this investigation are in agreement with this observation. The higher flame angle and shorter flame standoff may be seen in results like those presented in Figure 5.1 (or Figure 5.11 from a subsequent section), for example. Operated at identical inlet conditions, the $S_{45°}$ swirler always stabilizes a flame closer to the inlet and with a larger flame angle compared to the $S_{37°}$ swirler.

This highlights an interesting trade-off for the designers of LSB-based gas turbine engines. The $S_{45°}$ flame is located in a sharply decelerating flow field and as we discussed in Section 5.2, this results in a more stable flame, resistant to perturbations in the flow field. Simultaneously, the presence of the concentrated heat release near the inlet increases the strength of the toroidal recirculation zone present there. As we shall see in Section 5.4, this recirculation zone can become powerful enough to even cause the flame to attach itself to the lip of the inlet. Such a strong recirculation zone entrains hot products and retains them longer near the zone of heat release.

Table 5.3: *The following table lists the conditions at which CH PLIF images were acquired of a low and high swirl case at atmospheric pressure. These experiments were performed on Configuration B.*

| Case | T | ϕ | U_0 | S |
	K		m/s	
Low Swirl	443	0.90	40	0.57
High Swirl	434	0.91	40	0.62

This is a recipe for the production of thermal NO_x. While no emission measurements were made as part of this study, it may be reasonably anticipated that the NO_x performance of the $S_{45°}$ swirler will be degraded compared to the $S_{37°}$ swirler. The trade-off for gas turbine engine designers is thus between flame stability and emissions performance.

In Configuration A, the theoretical swirl number of the flow field is varied by switching out the swirlers. The mass flow split of each swirler is estimated from the blockage of the perforated plates covering the central portion of the swirler. On the other hand, Configuration B not only allows precise knowledge of this mass flow split, but also allows one to vary it in operation. This offers an alternate way to study the effect of swirl by changing the mass flow split. Figure 5.7 shows CH PLIF images of the flame sheet for a low and high swirl case. Also shown are the corresponding histograms measuring the statistics of the edge pixels in the central one-fourth of the flame. The test conditions for these two cases are presented in Table 5.3.

These results show that the flame position is strongly affected by changing the swirl number in this manner. The reduced flow of reactants through the central portion, coupled with the enhanced divergence induced by the increased swirl flow causes the flame to shift much further upstream. The reduction in the local reactant velocity also decreases the local turbulence level and accounts for a less convoluted flame sheet.

(a) $S = 0.57$

(b) $S = 0.62$

(c) $\mu = 463$; $\sigma = 187$
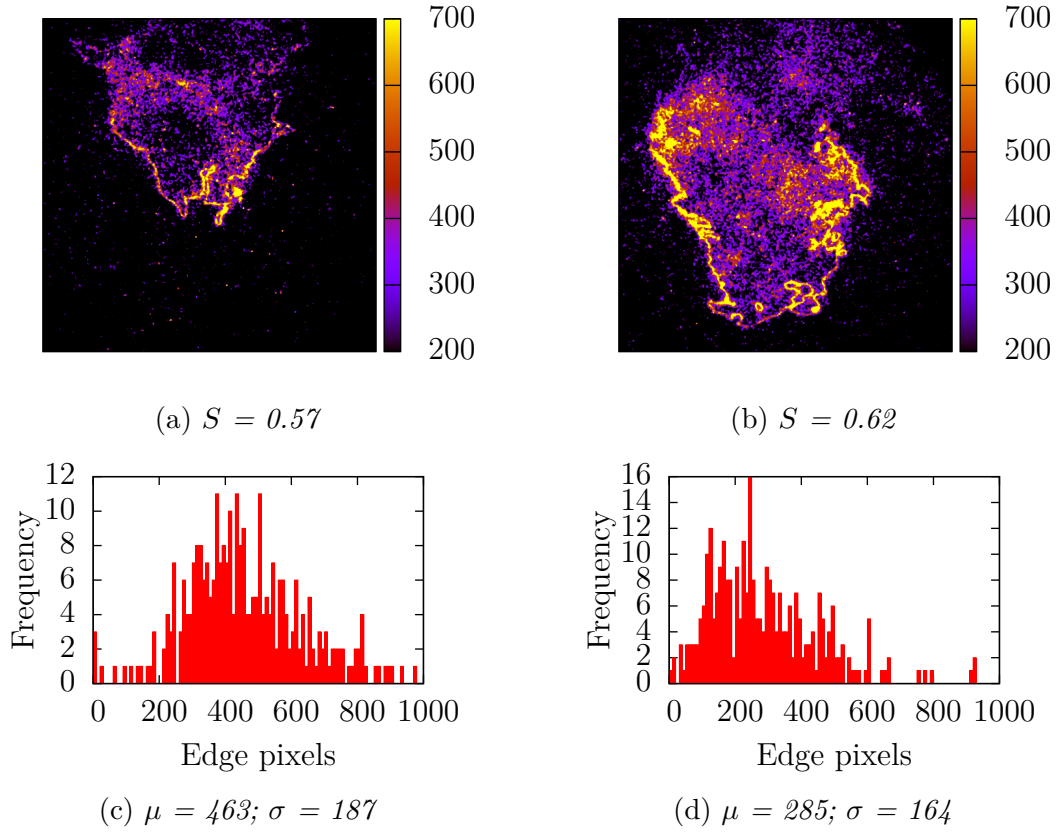
(d) $\mu = 285$; $\sigma = 164$

Figure 5.7: *The images above show a low and high swirl flame imaged by CH PLIF. These experiments are performed on Configuration B under preheated, atmospheric pressure conditions.*

Table 5.4: *The following table lists the conditions at which the equivalence ratio was varied to study its effects on the flame characteristics. The chemiluminescence experiments were performed on Configuration A, while the CH PLIF experiments were performed on Configuration B.*

Experiment	p atm	T K	ϕ	U_0 m/s
Chemiluminescence				
	12.4	570	0.53 ± 0.01	39.42
	12.6	583	0.58 ± 0.01	39.42
CH PLIF				
	1.0	443	0.90	40
	1.0	438	1.05	40

To conclude, the characteristics of the *Low*-Swirl Burner and its flame are the product of its *low* swirl numbers. Changing the amount of swirl tends to decrease the flame standoff distance and widen the flame cone angle. In the limit, when the core flow velocity is too low, the flame can flash back through the swirler.

5.4 Effect of Equivalence Ratio

The LSB is primarily intended for fuel-lean operation in order to utilize its low NO_x emission performance. As a result, most of the high pressure testing was done as close as possible to a target ϕ of 0.56. Limited testing was carried out at 12 atm for two off-target conditions: a slightly richer ($\phi \approx 0.58$) and a slightly leaner ($\phi \approx 0.53$) mixture, in order to explore the sensitivity of the LSB flame to limited changes in equivalence ratio. The $S_{45°}$ swirler was used for these tests. The conditions are presented in Table 5.4, while the corresponding averaged and Abel-deconvoluted flame images are presented in Figure 5.8.

Two characteristics of the flame are immediately obvious from these images. First, the zone of heat release, marked by the region from which CH* chemiluminescence

109
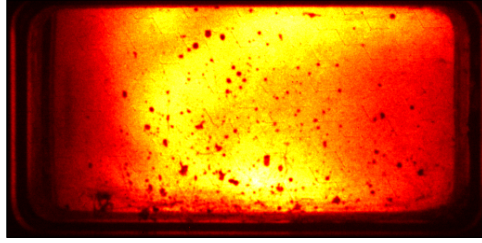
(a) $\phi = 0.53$
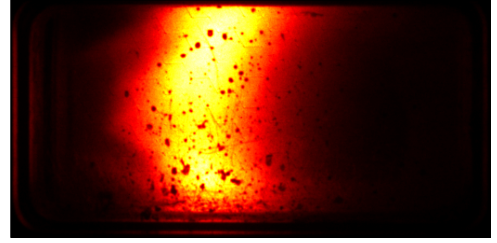
(b) $\phi = 0.58$
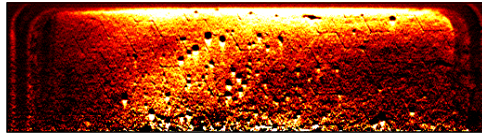
(c) *Abel-deconvoluted image*
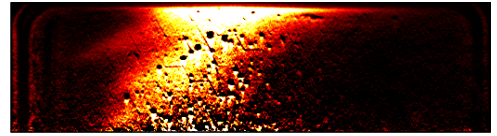
(d) *Abel-deconvoluted image*

Figure 5.8: *Figures 5.8a–5.8b show mean CH* chemiluminescence images of the LSB flame taken at high pressure for two equivalence ratios. Figures 5.8c–5.8d show the Abel-deconvolution of the average image highlighting the flame brush. The centerline of the combustor is along the lower edge of the Abel half-images.*

is observed, becomes increasingly compact at fuel-rich conditions. Virtually all other flame images acquired at leaner conditions show a long flame like in Figure 5.8a, with the heat release distributed over the entire visible area of the combustor. As discussed in the previous section, a compact heat release zone near the inlet results in strong recirculation features and potentially poor NO_x performance, e.g., an even higher NO_x increase than would be attributed to just the increase in temperature associated with the higher equivalence ratio.

Second, the flame brush for the richer flame in Figure 5.8b can be observed to wrap around and anchor itself on the dump plane. This is particularly observable in the Abel-deconvoluted image of the same flame in Figure 5.8d. The attached region is not as bright as the rest of the flame brush, indicating that the flame may be attaching itself only intermittently. This intermittent behavior can be confirmed from the instantaneous images where it is visible on some of the acquired images, but not others. This is seen from the sequence of images shown in Figure 5.9. This behavior was alluded to in Section 5.3 as being the result of the enhanced toroidal recirculation zone produced by this swirler. Thus, the intermittent attachment of the flame to the inlet indicates the increased importance of the toroidal recirculation zone in stabilizing the rich flame.

It should be noted that the reliance on a toroidal recirculation zone to anchor the flame to the inlet is one of the primary flame stabilization mechanisms used by traditional swirl combustors. Thus, LSB swirlers with high vane angles tend to behave like traditional swirl combustors at fuel-rich conditions at high pressure.

In order to explore the flame structure of a richer flame, LSB Configuration B was operated at ϕ values of 0.90 and 1.05 and imaged using CH PLIF. The conditions are listed in Table 5.4 and the sample instantaneous images from the dataset are presented in Figure 5.10. The accompanying histograms show statistics of the number of pixels detected on intensity edges. The average length (or number of edge pixels) of the
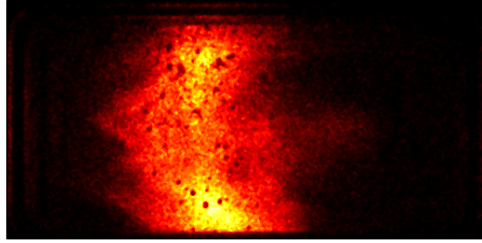
(a) *Frame #90*
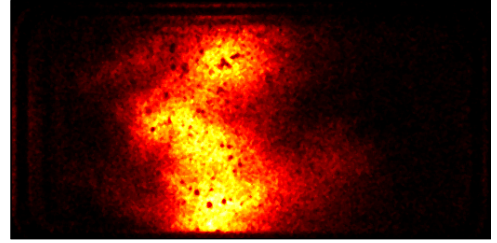
(b) *Frame #91*
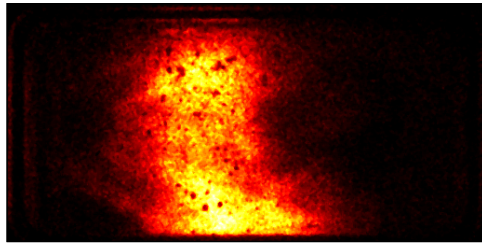
(c) *Frame #92*
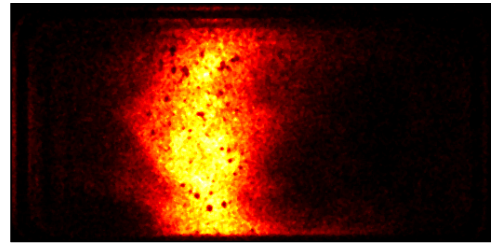
(d) *Frame #93*
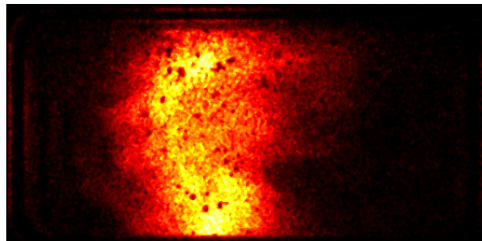
(e) *Frame #94*
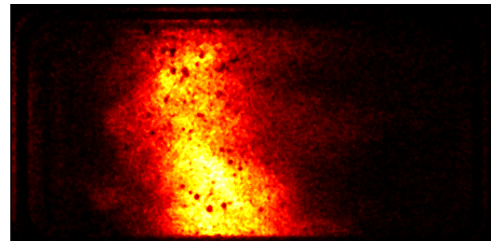
(f) *Frame #95*

Figure 5.9: *The sequence of frames above is taken from the high equivalence ratio data set and shows the flame intermittently attaching to the lip of the inlet.*

(a) $\phi = 0.90$

(b) $\phi = 1.05$

(c) $\mu = 463; \sigma = 187$

(d) $\mu = 353; \sigma = 127$
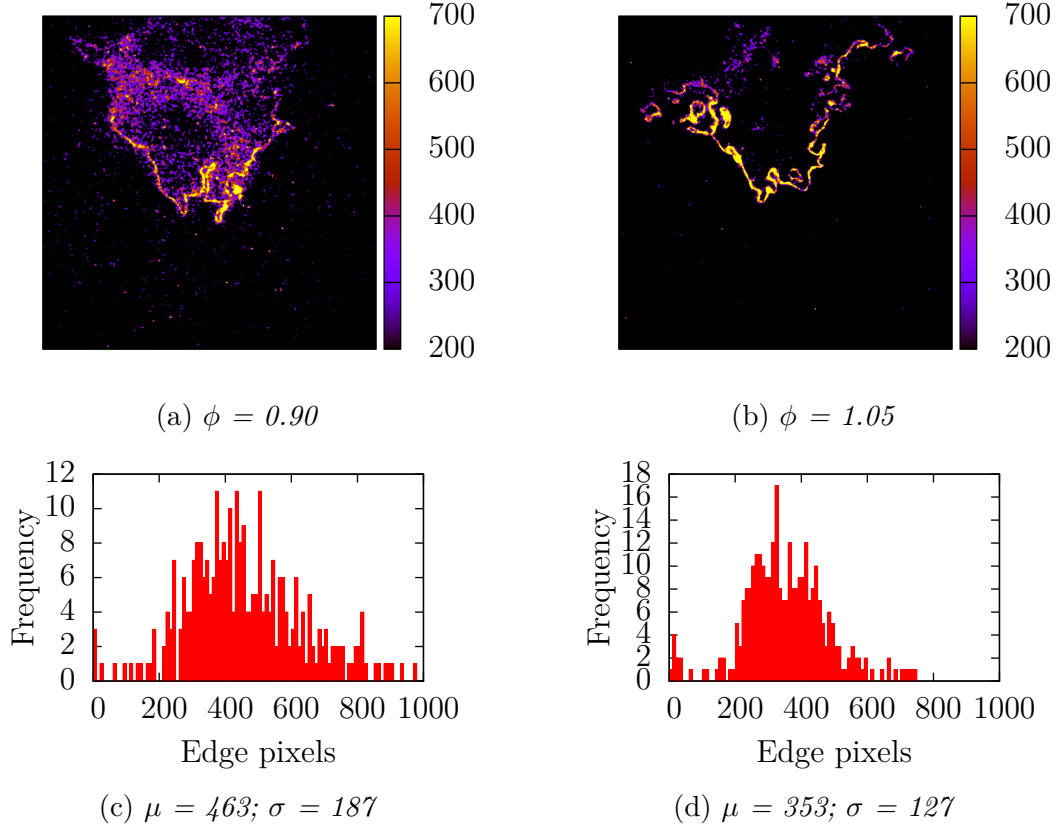
Figure 5.10: *Instantaneous CH PLIF images of a relatively lean and rich flame at preheated, atmospheric pressure conditions are shown. The histograms show the statistics of the number of detected intensity edges over 300 such frames. These experiments are conducted on Configuration B.*

flame sheet is lower at the higher equivalence ratio. This implies that the richer flame is less convoluted in the vicinity of the flame stabilization point.

On the Borghi diagram, increasing the equivalence ratio increases the laminar flame speed, and decreases the flame thickness. Neglecting any associated changes in the velocity field, this causes the operating point to move down and to the right on the diagram, much like in Figure 5.6. This change will move the point closer to the wrinkled laminar flame regime, reducing the amount of wrinkling and hence, the length of the flame sheet as demonstrated by the histogram in Figure 5.10

5.5 Effect of Combustor Pressure

In many gas turbine engines, the combustor pressure varies directly with the loading of the engine. Like the preheat temperature, the combustor pressure affects the LSB flame both through the fluid mechanics of the flow (by decreasing the kinematic viscosity) and the flame's chemical kinetics and scalar diffusion (affecting the laminar flame speed and flame thickness).

There is some confusion over how to study this effect and what to attribute it to. Pressure effects are often tracked using the Reynolds number. However, as noted in Section 5.2, it might not be the right parameter to use in the near field of the inlet. According to the turbulent flame speed model from Equation 2.4, at high pressures, the S_L term is insignificant compared to u and thus, the turbulent flame speed should see minimal pressure effects. Indeed, Kobayashi et al.[101, 102] have observed precisely this—the turbulent flame speed appears to be independent of the combustor pressure in their Bunsen burner setup. While Cheng et al. highlight the diminishing role of S_L, Griebel et al.[103] attribute this behavior to the fact that the decrease in laminar flame speed at high pressure is compensated for by the broadening of the turbulence spectrum. This results in finer turbulent structures in the flow as pressure increases—an observation also made by Kobayashi[104]—that cause a higher turbulent flame surface area and keep the turbulent flame speed nearly constant. Griebel et al. further note that theoretically, a slight drop in the turbulent flame speed with pressure may be expected.

In order to resolve the uncertainties regarding how the LSB flame responds to combustor pressure, the flame was imaged over a range of operating conditions from 3 to 12 atm. For these tests, the reference velocity and the equivalence ratio were held constant. However, the temperature of the reactants increased somewhat with pressure. The reason for this was discussed in Chapter 3 and is because of the reduced

Table 5.5: *The following are the test conditions at which pressure sweeps were performed to study its effects on the flame characteristics. The experiments were conducted on Configuration A and the swirler used for the pressure sweeps is noted.*

Experiment	p atm	T K	ϕ	U_0 m/s
$S_{37°}$				
	3.06	506	0.57 ± 0.04	37.8
	6.04	525	0.57 ± 0.02	37.3
	9.08	544	0.56 ± 0.02	37.2
	12.1	559	0.56 ± 0.01	37.4
$S_{45°}$				
	3.01	485	0.57 ± 0.04	36.7
	6.01	516	0.58 ± 0.02	38.2
	9.05	553	0.58 ± 0.01	39.2
	12.0	582	0.56 ± 0.01	40.9

heat losses in the supply lines at the high flow rates required to pressurize the LSB. The experimental conditions are presented in Table 5.5 The flame location and cone angle inferred from the flame images are presented in Figure 5.11.

At low to moderate pressures, the flame location is nearly invariant for $S_{37°}$, but moves upstream for the $S_{45°}$ cases. This behavior can be explained as follows. The flame stabilization location for the $S_{45°}$ swirler is closer to the dump plane compared to the $S_{37°}$ swirler. Since the heat transfer back to the reactants is more efficient, the increasing reactant temperature through our test cases dominate pressure effects and moves the $S_{45°}$ flame upstream. The $S_{37°}$ flame is less affected by these processes.

At high pressures, however, both flames are observed to move downstream, despite the increasing preheat temperatures. The apparent decrease in the turbulent flame speed at these conditions is an unexpected result, and Equation 2.4 is insufficient in accounting for this observation. Figure 5.11 also shows that the flame angle for both cases decreases slightly with pressure. This suggests that the turbulent flame speed
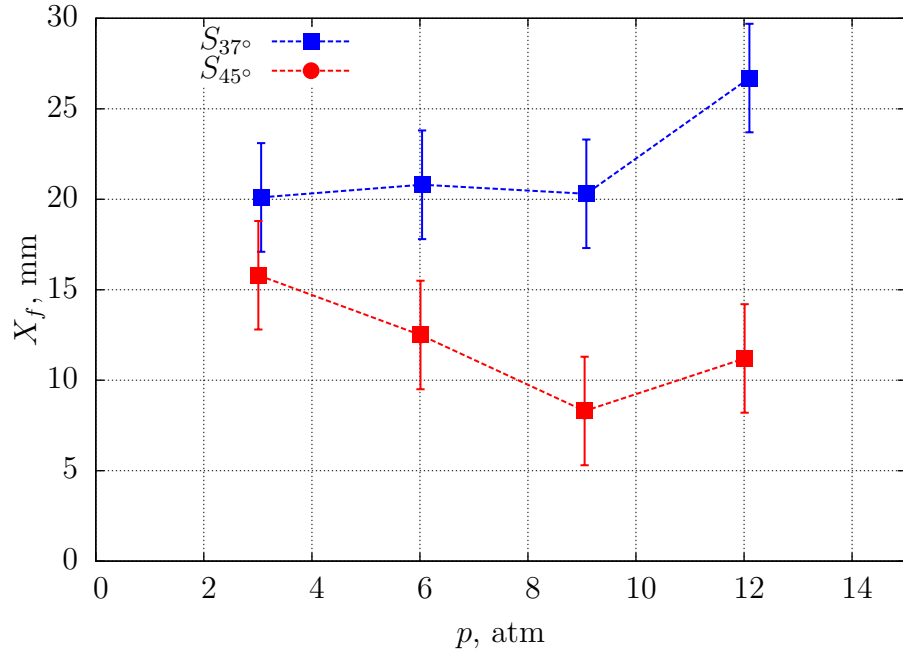
(a) *Flame standoff distance as a function of the combustor pressure*
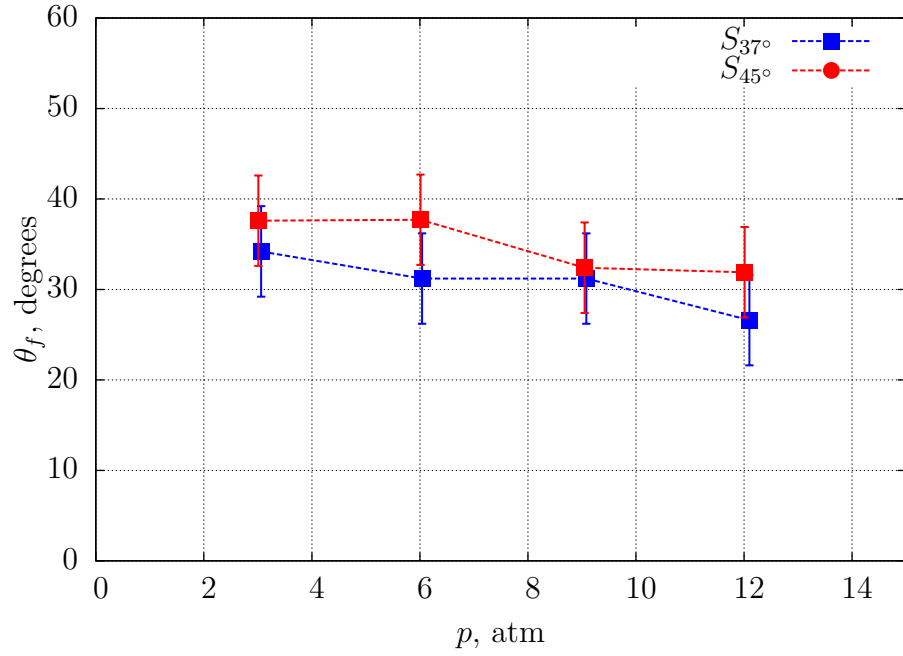
(b) *Flame cone angle as a function of the combustor pressure*

Figure 5.11: *The plots above show the effect of varying the combustor pressure on the flame location and flame cone angle. The blue curves represent data points from the $S_{37°}$ swirler tests, while the red curves represent data from the $S_{45°}$ swirler tests. An uncertainty of ± 3 mm and $\pm 5°$ are estimated for the standoff distance and flame angle calculations respectively.*

was consistently and slowly decreasing with pressure as predicted by Griebel et al. In light of this, the nearly constant location of the $S_{37°}$ flame could be attributed to the effects of increasing combustor pressure and preheat temperature nearly canceling each other out at the lower pressures.

This has repercussions for the gas turbine designers as a flame stabilized further away from the inlet is likelier to be blown off due to perturbations. Increasing the preheat of the reactants could offset this behavior, as can increasing the swirl in the flow field. In practice, these may be non-trivial to implement in a gas turbine engine. Adding hydrogen to the reactants may be a simpler way to stabilize the high pressure flames.

Finally, it is interesting to consider this on a Borghi diagram to deduce any changes in the flame structure that might result from high pressure operation. Kobayashi et al.[104] report that the increasing pressure causes a weak drop in u, reaching a minimum around 10 atm. However, the $\dfrac{u}{S_L}$ factor would be dominated by the precipitous fall in the laminar flame speed, causing it to in fact increase with pressure. On the X-axis, the integral length scale is very nearly unaffected by the pressure change, but the flame thickness decreases rapidly. Thus, pressure causes the operating point to move up and to the right on the diagram. This motion is unlikely to cause the turbulent combustion regime to change. Unfortunately, due to the absence of spatially-resolved, high pressure flame structure images, it may only be surmised at this stage that the observable effect of increasing the combustor pressure would be limited to an increase in the fine structure of the wrinkles in the flame sheet.

5.6 Summary of Results

The effect of various flow parameters on the LSB flame characteristics have been examined using both CH* chemiluminescence imaging and CH PLIF. The key results from this investigation are as follows:

1. Low to moderate reference velocities do not affect the flame at high pressure. High reference velocities cause the flame to shift downstream. The flame becomes more wrinkled due to increased turbulence.

2. Preheating the reactants causes the flame to move upstream, but may also strengthen recirculation zones in the combustor. The flame structure is expected to become more wrinkled.

3. Swirl—controlled either through the vane angle or through the mass flow split—causes the flame to anchor closer to the inlet and have a larger cone angle. The decreased flow rate through the core reduces wrinkling in the flame structure.

4. Richer flames at high pressure and high swirl can change flame shape and behave like attached flames. Equivalence ratio also results in strong combustion and a less wrinkled flame.

5. At high pressures, the LSB flame moves downstream. In order to preserve flame stability, this should be countered by increasing the preheat or changing the swirl number, if possible.

CHAPTER 6

CONCLUSIONS

The results presented in this thesis cover two areas—development of a CH PLIF system for flame zone imaging and improved understanding of the Low Swirl Burner. The following sections summarize the major accomplishments of this thesis relating to each field.

6.1 Summary of CH PLIF Results

The development and implementation of a CH PLIF imaging system were detailed. The results from preliminary work designed to evaluate and study the laser were presented. The optimal laser wavelength for exciting CH radicals was determined through an excitation scan, and shown to be essentially the same over a wide range of operating conditions. The scaling of the LIF signal with the operating laser intensity was measured to confirm our operation in the linear LIF regime.

Simultaneously, a four-level model was developed that reflected the physical process of CH LIF with higher fidelity than a simple two-level model. The model is intended to be a semi-quantitative prediction of the LIF signal levels in hydrocarbon flames with a range of initial conditions and accounts for collisional quenching of excited CH molecules. Results from a laminar methane-air Bunsen flame were used to validate the qualitative behavior of the LIF signal predicted by the model. Chemkin simulations of a 1-D, freely propagating laminar flame were used to provide the species concentrations and temperature through the flame.

The model was subsequently extended to predict the signal variation across pressures and preheat temperatures for a laminar, unstrained methane-air flame. The

results demonstrate that the CH LIF signal is enhanced by preheat temperature, but diminished by pressure. The signal mostly scales with the flame temperature, although the correlation is not perfect. By establishing a signal threshold based on the atmospheric pressure Bunsen flame data, it was shown that high signal-to-noise ratio imaging of ultra-lean (e.g., equivalence ratios below 0.75) methane flames at high pressures is not likely to be possible with the current CH PLIF imaging system, even with the typically high preheat levels found in gas turbine combustors.

Going beyond methane-air flames, the signal levels were calculated for ethane-air and propane-air mixtures. The increase in signal levels was found to be minor, with the results for ethane-air and propane-air mixtures being almost the same. The hypothesis of boosting CH LIF signals in a methane-air flame by doping the reactants with a small quantity of ethane or propane was examined. The resulting increase in CH LIF signals from methane-air flames due to higher-order alkane addition was found to be insignificant at lean operating conditions.

Next, syngas flames with alkane-addition were considered as possible candidates for CH LIF studies. The CH LIF signal was once again seen to increase with the flame temperature, with high-hydrogen content syngases responding better to these experiments by producing high CH LIF signals. The choice of alkane—methane, ethane or propane—that was used to produce the CH signal was found to be immaterial, with all producing very similar signal levels.

Finally, the effect of straining the 1-D, laminar flame was examined by simulating an opposed flow flame over a range of strain rates. The results generally followed the behavior of the maximum flame temperature in such flames, increasing slightly with low strain rates, but dropping as it approached extinction.

In all, over 15,000 cases were simulated for this work, spanning several fuels (methane, ethane, propane, CO-H_2 syngas mixtures), reactant composition ($\phi = 0.5$–1.8), and initial conditions ($p = 1$–12 atm, $T = 300$–700 K).

6.2 Summary of LSB Results

Regarding the Low Swirl Burner, this thesis provides results over a wide range of operating conditions, including high preheat and high pressure tests. The flame and flow fields were characterized by a combination of CH* chemiluminescence imaging, LDV and CH PLIF. Based on the CH* imaging, the flames were characterized by their standoff distance from the inlet, their cone angles and their structure. While the structure of the flames was nearly impossible to study with a line-of-sight integrated technique like flame chemiluminescence imaging, the variation of the standoff distance and flame angle were measured at different operating conditions. The applicability of earlier models to explain LSB flame stabilization behavior was found to hold for low and moderate velocity conditions at elevated pressures. However, at very high velocities, the flame location was observed to move downstream. This deviation from earlier models was attributed to the bending effect in the $\frac{S_T}{S_L}$ versus $\frac{u}{S_L}$ diagram, which predicts a slower rate of increase in the turbulent flame speed at high levels of turbulence. Preheat temperature was shown to have a stabilizing effect on the flame, causing the flame standoff distance to decrease and reducing its responses to perturbations. Varying the amount of swirl in the combustor also stabilized the flame closer to the inlet by reducing the local axial velocity along the centerline. The flame shape was shown to be sensitive to equivalence ratio at elevated pressures. High pressure flames operated at less lean conditions tended to partially anchor the flame to the inlet lip. Finally, very high pressures were shown to cause the flame to move downstream due to reduced turbulent flame speeds. Hydrogen-addition to enhance the flame speed was suggested as one option to mitigate this behavior. The results highlight interesting challenges for gas turbine combustor designers in implementing the LSB in current and future gas turbine engines.

Supplementing the chemiluminescence results, spatially-resolved CH PLIF data

acquired at atmospheric pressure demonstrates the effect of several flow parameters on the flame structure. Increasing preheat temperature or the reactant mixture's equivalence ratio is shown to cause the flame sheet to be less wrinkled, while increasing the reference velocity caused the opposite effect. The swirl in the flow field was shown to strongly affect the flame position and wrinkling due to its direct influence on the core flow velocity profile. Increasing the swirl, by reducing the core flow in these studies, caused the flame to rapidly move upstream, while the reduced turbulence caused the flame sheet to be less wrinkled.

6.3 Recommendations for Future Work

There is room for improvement in developing a sensitive technique that can be used to image the flame sheet at very high pressure conditions. The results in this thesis demonstrate the limitations of CH PLIF when used to image lean flames at high pressure conditions. Some of these limitations are caused by the inherently low CH concentration, as well as the high rates of collisional quenching at these conditions which produce a weak fluorescence signal. On the other hand, a higher power excitation beam (while keeping the intensity low enough to avoid breakdown or saturation) or more sensitive optics could definitely extend the range of equivalence ratios at which CH PLIF can be feasibly applied.

The CH LIF signal could be further strengthened by using a multi-pass cell or light traps that cause the incident radiation to make several passes through the measurement volume. Since the incident radiation is provided by a pulsed laser, the optics used will need to have high damage thresholds. Further, at high pressure conditions, beam steering issues could make it difficult to restrict the laser sheet to a single plane.

The CH LIF model developed for this thesis needs to be validated against experimental data at more conditions, particularly at lean conditions which are of interest to the combustion community.

A technique like HCO PLIF improves upon some of these limitations by being relatively insensitive to equivalence ratio, but it would still suffer from signal loss at high pressure due to collisional quenching. A solution to this problem can be found by resorting to saturated LIF. By operating the laser output at high intensity, the output signal is no longer affected by the quenching rate. If the laser intensity is too high, there is danger of inducing breakdown in medium (which is more likely at higher pressures) or causing damage to windows or optics. If the saturation intensity for HCO PLIF is above the breakdown threshold, some relief could be obtained by pulse stretching or by multimode excitation—the same techniques that gave the current implementation of CH PLIF its edge.

Most of the outstanding questions regarding the LSB flame stabilization boil down to relating the effect the velocity field and the heat release from the flame have on each other. An elegant way to answer these questions is to simultaneously image both the velocity field and the reaction zone at moderate or even high pressure conditions. PIV is an excellent diagnostic technique to measure the velocity field, and several reasons have been provided in the current thesis as to why PLIF is an ideal technique to image flame fronts. A simultaneous PIV/PLIF map of the combustor would provide enough data to bring out local effects of eddy-flame interactions and lead to the development of better models for relating turbulent flame speed to other measurables in the flow field. More specific to the LSB, these results could pinpoint the cause of the observed drop in turbulent flame speed at high pressure or high velocity conditions.

This thesis has focused only on the static stability of the LSB combustor, eschewing discussion on the dynamics of the combustor. No reproducible dynamic instabilities were encountered during the operation of the LSB combustor during the experiments conducted in this study. Nevertheless, gas turbine combustor designers intending to use the LSB will benefit from a more thorough investigation of the combustor, particularly at high pressure, high preheat conditions.

APPENDIX A

SEEDER DESIGN

A new seeder was designed for use in high pressure implementations of diagnostic techniques like Laser Doppler Velocimetry (LDV), Particle Image Velocimetry (PIV), etc.

The previous design, as shown in Figure A.1, was a fluidized bed seeding generator. Seeding particles in a cylindrical vessel are fluidized by an air-turbine vibrator. Air is introduced into the vessel in the form of two opposing jets directed tangentially to produce a small amount of swirl in the flow field. Particles are picked up by the air flow and the swirl aids in separating the heavy/coagulated clumps of seeding particles by centrifugal acceleration.

This design had several shortcomings. First, it is observed that the seeding density of the seeded flow generally decreases over time, even if the seeding particles have not been depleted. The seeding particles tend to coagulate over time, due to the buildup of moisture, static charge, etc. In such cases, the vibrator can no longer effectively fluidize the particles. Further, the tangential introduction of the air flow preferentially depletes particles near the walls of the container, leaving the center relatively undisturbed. The cumulative effect of these phenomena diminishes the effectiveness of the seeder.

Second, the fluidized bed requires a minimum amount of seeding particles to function effectively. This requires the seeder to be refilled even before all the seeding particles are consumed.

Third, when designed for high pressure applications, the seeder will become quite heavy due to flanges and other fittings. Such a setup cannot be easily fluidized using a reasonable-sized air-turbine vibrator.
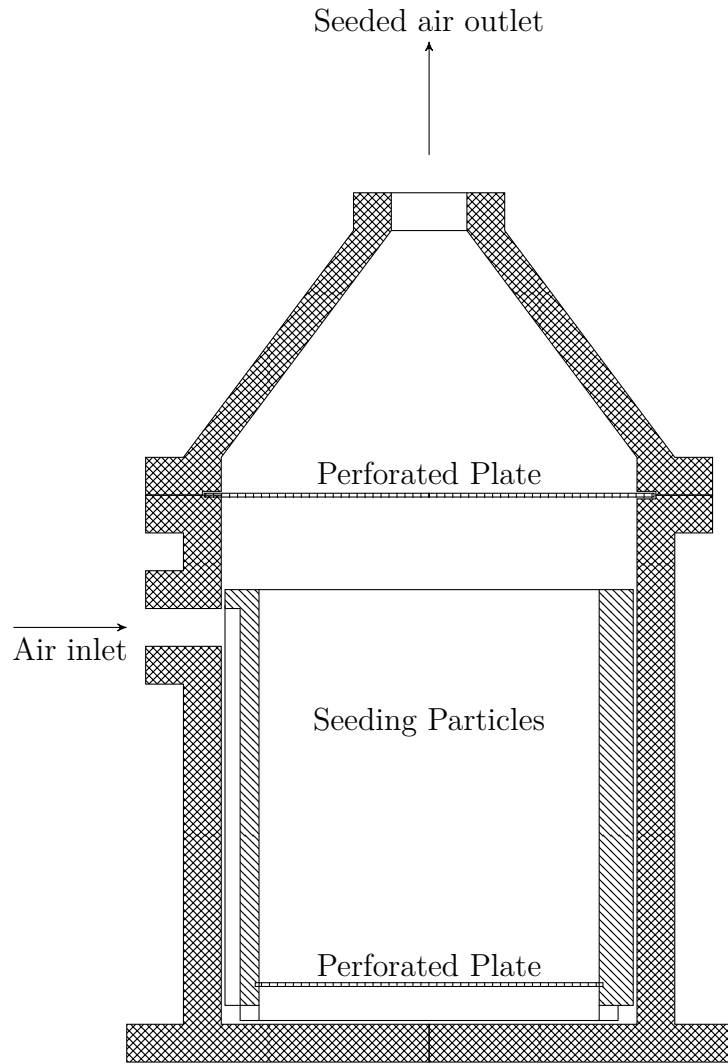
Figure A.1: *A schematic of the old fluidized bed seeder is presented. The air enters the seeder through a groove along the inner vessel and is injected with a tangential velocity at the base of the seeder. The whole assembly is vibrated (vibrator not shown) to keep the particle bed fluidized. The seeded air flow exits through the outlet on the top.*

Seeded air outlet

Perforated Plate

Seeding Particles

Air inlet
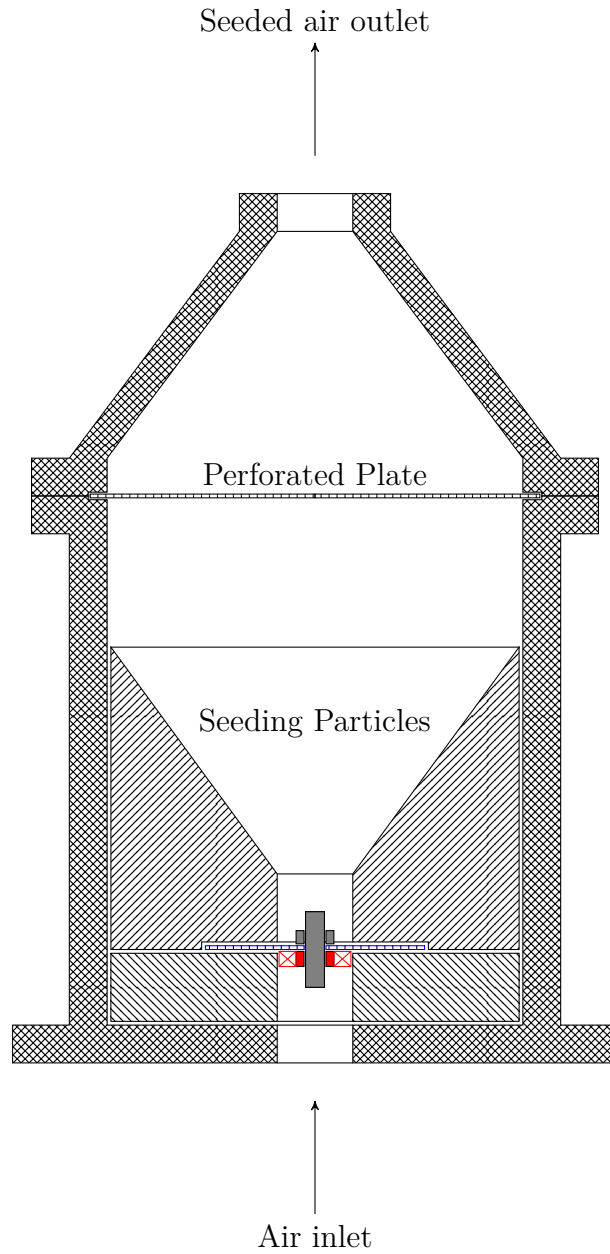
Figure A.2: *The improved design of the seeder is shown here in schematic form. The air enters the assembly from the inlet at the bottom, passes through the swirler (shown in* red*) and enters the seeder. The perforated plate at the bottom (shown in* blue*) keeps the seeding particles within the seeder. The swirler hub is threaded, allowing it to be secured to the perforated plate by a short steel bolt (shown in* gray*). After picking up the particles, a second perforated plate prevents large clumped seeding particles from passing through. The seeded air flow exits through the outlet at the top.*

The new seeder design is shown in Figure A.2, and resembles a funnel with a swirler located halfway up the stem. A perforated base plate holds the swirler and the seeding particles in the conical section of the swirler. Due to the steep angle of the sides of the conical section, the seeding particles continuously collapse into the central section. This negates any need for vibrating the system. Air is introduced from the bottom of the seeder and enters the vessel by passing through the swirler. Since all the air enters this way, there is a considerable amount of swirl in the resulting flow field, Heavy/coagulated seeding particles are flung outward, while lighter particles are carried with the air. After a sufficient distance to allow for the cyclonic separation to be effective, the seeded air passes through another perforated plate which further limits the presence of large clumps of particles. The exiting air is now spatially and temporally uniformly seeded.

REFERENCES

[1] I. Glassman, *Combustion*. Academic Press, 1996.

[2] N. Syred and J. M. Beér, "Combustion in Swirling Flows: A Review," *Combustion and Flame*, vol. 23, no. 2, pp. 143–201, 1974.

[3] D. G. Lilley, "Swirl Flows in Combustion: A Review," *AIAA Journal*, vol. 15, no. 8, pp. 1063–1078, 1977.

[4] B. Bédat and R. K. Cheng, "Experimental Study of Premixed Flames in Intense Isotropic Turbulence," *Combustion and Flame*, vol. 100, no. 3, pp. 485–494, 1995.

[5] R. S. Barlow, R. W. Dibble, J. Y. Chen, and R. P. Lucht, "Effect of Damköhler Number on Superequilibrium OH Concentration in Turbulent Nonpremixed Jet Flames," *Combustion and Flame*, vol. 82, no. 3-4, pp. 235–251, 1990.

[6] C. F. Kaminski, J. Hult, and M. Aldén, "High repetition rate planar laser induced fluorescence of OH in a turbulent non-premixed flame," *Applied Physics B: Lasers and Optics*, vol. 68, no. 4, pp. 757–760, 1999.

[7] J. Hult, U. Meier, W. Meier, A. Harvey, and C. F. Kaminski, "Experimental analysis of local flame extinction in a turbulent jet diffusion flame by high repetition 2-D laser techniques and multi-scalar measurements," in *Proceedings of the Combustion Institute*, vol. 30, pp. 701–709, 2005.

[8] H. Malm, G. Sparr, J. Hult, and C. F. Kaminski, "Nonlinear diffusion filtering of images obtained by planar laser-induced fluorescence spectroscopy," *Journal of The Optical Society of America A: Optics, image science, and vision*, vol. 17, no. 12, pp. 2148–2156, 2000.

[9] R. Abu-Gharbieh, G. Hamarneh, T. Gustavsson, and C. F. Kaminski, "Flame front tracking by laser induced fluorescence spectroscopy and advanced image analysis," *Optics Express*, vol. 8, no. 5, pp. 278–287, 2001.

[10] C. M. Vagelopoulos and J. H. Frank, "An experimental and numerical study on the adequacy of CH as a flame marker in premixed methane flames," in *Proceedings of the Combustion Institute*, vol. 30, pp. 241–249, 2005.

[11] M. Köhler, A. Brockhinke, M. Braun-Unkhoff, and K. Kohse-Höinghaus, "Quantitative Laser Diagnostic and Modeling Study of C_2 and CH Chemistry in Combustion," *The Journal of Physical Chemistry A*, vol. 114, no. 14, pp. 4719–4734, 2010.

[12] C. P. Fenimore, "Formation of nitric oxide in premixed hydrocarbon flames," in *Symposium (International) on Combustion*, vol. 13, pp. 373–380, 1971.

[13] Z. S. Li, J. Kiefer, J. Zetterberg, M. Linvin, A. Leipertz, X. S. Bai, and M. Aldén, "Development of improved PLIF CH detection using an Alexandrite laser for single-shot investigation of turbulent and lean flames," in *Proceedings of the Combustion Institute*, vol. 31, pp. 727–735, 2007.

[14] H. N. Najm, P. H. Paul, C. J. Mueller, and P. S. Wyckoff, "On the Adequacy of Certain Experimental Observables as Measurements of Flame Burning Rate," *Combustion and Flame*, vol. 113, no. 3, pp. 312–332, 1998.

[15] J. Kiefer, Z. S. Li, J. Zetterberg, X. S. Bai, and M. Aldén, "Investigation of local flame structures and statistics in partially premixed turbulent jet flames using simultaneous single-shot CH and OH planar laser-induced fluorescence imaging," *Combustion and Flame*, vol. 154, no. 4, pp. 802–818, 2008.

[16] P. H. Paul and H. N. Najm, "Planar laser-induced fluorescence imaging of flame heat release rate," in *Symposium (International) on Combustion*, vol. 27, pp. 43–50, 1998.

[17] B. O. Ayoola, R. Balachandran, J. H. Frank, E. Mastorakos, and C. F. Kaminski, "Spatially resolved heat release rate measurements in turbulent premixed flames," *Combustion and Flame*, vol. 144, no. 1, pp. 1–16, 2006.

[18] J. Kiefer, Z. S. Li, T. Seeger, A. Leipertz, and M. Aldén, "Planar laser-induced fluorescence of HCO for instantaneous flame front imaging in hydrocarbon flames," in *Proceedings of the Combustion Institute*, vol. 32, pp. 921–928, 2009.

[19] C. K. Chan, K. S. Lau, W. K. Chin, and R. K. Cheng, "Freely propagating open premixed turbulent flames stabilized by swirl," in *Symposium (International) on Combustion*, vol. 24, pp. 511–518, 1992.

[20] R. K. Cheng, "Velocity and Scalar Characteristics of Premixed Turbulent Flames Stabilized by Weak Swirl," *Combustion and Flame*, vol. 101, no. 1-2, pp. 1–14, 1995.

[21] T. Plessing, C. Kortschik, N. Peters, M. S. Mansour, and R. K. Cheng, "Measurements of the turbulent burning velocity and the structure of premixed flames on a low-swirl burner," in *Proceedings of the Combustion Institute*, vol. 28, pp. 359–366, 2000.

[22] I. G. Shepherd and R. K. Cheng, "The Burning Rate of Premixed Flames in Moderate and Intense Turbulence," *Combustion and Flame*, vol. 127, no. 3, pp. 2066–2075, 2001.

[23] R. K. Cheng, I. G. Shepherd, B. Bédat, and L. Talbot, "Premixed turbulent flame structures in moderate and intense isotropic turbulence," *Combustion Science and Technology*, vol. 174, no. 1, pp. 29–59, 2002.

[24] I. G. Shepherd, R. K. Cheng, T. Plessing, C. Kortschik, and N. Peters, "Premixed flame front structure in intense turbulence," in *Proceedings of the Combustion Institute*, vol. 29, pp. 1833–1840, 2002.

[25] C. Kortschik, T. Plessing, and N. Peters, "Laser optical investigation of turbulent transport of temperature ahead of the preheat zone in a premixed flame," *Combustion and Flame*, vol. 136, no. 1-2, pp. 43–50, 2004.

[26] L. P. H. de Goey, T. Plessing, R. T. E. Hermanns, and N. Peters, "Analysis of the flame thickness of turbulent flamelets in the thin reaction zones regime," in *Proceedings of the Combustion Institute*, vol. 30, pp. 859–866, 2005.

[27] J. B. Bell, R. K. Cheng, M. S. Day, and I. G. Shepherd, "Numerical simulation of Lewis number effects on lean premixed turbulent flames," in *Proceedings of the Combustion Institute*, vol. 31, pp. 1309–1317, 2007.

[28] D. T. Yegian and R. K. Cheng, "Development of a lean premixed low-swirl burner for low NO_x practical applications," *Combustion Science and Technology*, vol. 139, no. 1, pp. 207–227, 1998.

[29] R. K. Cheng, D. T. Yegian, M. M. Miyasato, G. S. Samuelsen, C. E. Benson, R. Pellizzari, and P. Loftus, "Scaling and development of low-swirl burners for low-emission furnaces and boilers," in *Proceedings of the Combustion Institute*, vol. 28, pp. 1305–1313, 2000.

[30] D. Littlejohn, A. J. Majeski, S. Tonse, C. Castaldini, and R. K. Cheng, "Laboratory investigation of an ultralow NO_x premixed combustion concept for industrial boilers," in *Proceedings of the Combustion Institute*, vol. 29, pp. 1115–1121, 2002.

[31] M. R. Johnson, D. Littlejohn, W. A. Nazeer, K. O. Smith, and R. K. Cheng, "A comparison of the flowfields and emissions of high-swirl injectors and low-swirl

injectors for lean premixed gas turbines," in *Proceedings of the Combustion Institute*, vol. 30, pp. 2867–2874, 2005.

[32] W. A. Nazeer, K. O. Smith, P. Sheppard, R. K. Cheng, and D. Littlejohn, "Full scale testing of a low swirl fuel injector concept for ultra-low NO_x gas turbine combustion systems," in *Proceedings of ASME Turbo Expo GT2006-90150*, 2006.

[33] R. K. Cheng, D. Littlejohn, W. A. Nazeer, and K. O. Smith, "Laboratory studies of the flow field characteristics of low-swirl injectors for adaptation to fuel-flexible turbines," in *Proceedings of ASME Turbo Expo GT2006-90878*, 2006.

[34] R. K. Cheng, D. Littlejohn, W. A. Nazeer, and K. O. Smith, "Laboratory Studies of the Flow Field Characteristics of Low-Swirl Injectors for Adaptation to Fuel-Flexible Turbines," *Journal of Engineering for Gas Turbines and Power*, vol. 130, p. 021501, 2008.

[35] R. K. Cheng and D. Littlejohn, "Effects of combustor geometry on the flowfields and flame properties of a low-swirl injector," in *Proceedings of ASME Turbo Expo GT2008-50504*, 2008.

[36] R. K. Cheng and D. Littlejohn, "Laboratory Study of Premixed H_2-Air and H_2-N_2-Air Flames in a Low-Swirl Injector for Ultralow Emissions Gas Turbines," *Journal of Engineering for Gas Turbines and Power*, vol. 130, p. 031503, 2008.

[37] D. Littlejohn and R. K. Cheng, "Fuel effects on a low-swirl injector for lean premixed gas turbines," in *Proceedings of the Combustion Institute*, vol. 31, pp. 3155–3162, 2007.

[38] R. K. Cheng, D. Littlejohn, P. A. Strakey, and T. Sidwell, "Laboratory investigations of a low-swirl injector with H_2 and CH_4 at gas turbine conditions," in *Proceedings of the Combustion Institute*, vol. 32, pp. 3001–3009, 2009.

[39] D. Littlejohn, R. K. Cheng, D. R. Noble, and T. Lieuwen, "Laboratory Investigations of Low-Swirl Injectors Operating With Syngases," *Journal of Engineering for Gas Turbines and Power*, vol. 132, p. 011502, 2010.

[40] P. Petersson, J. Olofsson, C. Brackman, H. Seyfried, J. Zetterberg, M. Richter, M. Aldén, M. A. Linne, R. K. Cheng, A. Nauert, D. Geyer, and A. Dreizler, "Simultaneous PIV/OH-PLIF, Rayleigh thermometry/OH-PLIF and stereo PIV measurements in a low-swirl flame," *Applied Optics*, vol. 46, no. 19, pp. 3928–3936, 2007.

[41] R. H. Barnes, C. E. Moeller, J. F. Kircher, and C. M. Verber, "Dye-Laser Excited CH Flame Fluorescence," *Applied Optics*, vol. 12, no. 11, pp. 2531–2532, 1973.

[42] J. F. Verdieck and P. A. Bonczyk, "Laser-induced saturated fluorescence investigations of CH, CN and NO in flames," in *Symposium (International) on Combustion*, vol. 18, pp. 1559–1566, 1981.

[43] M. G. Allen, R. D. Howe, and R. K. Hanson, "Digital imaging of reaction zones in hydrocarbon-air flames using planar laser-induced fluorescence of CH and C_2," *Optics Letters*, vol. 11, no. 3, pp. 126–128, 1986.

[44] M. Namazian, R. L. Schmitt, and M. B. Long, "Two-wavelength single laser CH and CH_4 imaging in a lifted turbulent diffusion flame," *Applied Optics*, vol. 27, no. 17, pp. 3597–3600, 1986.

[45] R. W. Schefer, M. Namazian, and J. Kelly, "Stabilization of lifted turbulent-jet flames," *Combustion and Flame*, vol. 99, no. 1, pp. 75–86, 1994.

[46] P. H. Paul and J. E. Dec, "Imaging of reaction zones in hydrocarbon-air flames by use of planar laser-induced fluorescence of CH," *Optics Letters*, vol. 19, no. 13, pp. 998–1000, 1994.

[47] C. D. Carter, J. M. Donbar, and J. F. Driscoll, "Simultaneous CH planar laser-induced fluorescence and particle imaging velocimetry in turbulent nonpremixed flames," *Applied Physics B: Lasers and Optics*, vol. 66, no. 1, pp. 129–132, 1998.

[48] K. A. Watson, K. M. Lyons, J. M. Donbar, and C. D. Carter, "Observations on the Leading Edge in Lifted Flame Stabilization," *Combustion and Flame*, vol. 119, no. 1-2, pp. 199–202, 1999.

[49] K. A. Watson, K. M. Lyons, J. M. Donbar, and C. D. Carter, "Simultaneous Rayleigh Imaging and CH-PLIF Measurements in a Lifted Jet Diffusion Flame," *Combustion and Flame*, vol. 123, no. 1–2, pp. 252–265, 2000.

[50] J. M. Donbar, J. F. Driscoll, and C. D. Carter, "Reaction Zone Structure in Turbulent Nonpremixed Jet Flames—From CH-OH PLIF Images," *Combustion and Flame*, vol. 122, no. 1-2, pp. 1–19, 2000.

[51] D. Han and M. G. Mungal, "Simultaneous measurement of velocity and CH layer distribution in turbulent non-premixed flames," in *Proceedings of the Combustion Institute*, vol. 28, pp. 261–267, 2000.

[52] P. S. Kothnur, M. S. Tsurikov, N. T. Clemens, J. M. Donbar, and C. D. Carter, "Planar imaging of CH, OH, and velocity in turbulent non-premixed jet flames," in *Proceedings of teh Combustion Institute*, vol. 29, pp. 1921–1927, 2002.

[53] D. Han and M. G. Mungal, "Simultaneous measurements of velocity and CH distributions. Part 1: jet flames in co-flow," *Combustion and Flame*, vol. 132, no. 3, pp. 565–590, 2003.

[54] D. Han and M. G. Mungal, "Simultaneous measurements of velocity and CH distributions. Part II: deflected jet flames," *Combustion and Flame*, vol. 133, no. 1–2, pp. 1–17, 2003.

[55] J. A. Sutton and J. F. Driscoll, "Optimization of CH fluorescence diagnostics in flames: range of applicability and improvements with hydrogen addition," *Applied Optics*, vol. 42, no. 15, pp. 2819–2828, 2003.

[56] Z. S. Li, J. Zetterberg, M. Linvin, M. Aldén, J. Kiefer, T. Seeger, and A. Leipertz, "Planar laser-induced fluorescence of combustion intermediates in turbulent methane/air flames stabilized on a co-axial jet flame burner," in *Proceedings of the European Combustion Meeting, ECM2007, Chania, Crete, Greece*, vol. 3, pp. 5–12–1–6, 2007.

[57] J. Kiefer, Z. Li, J. Zetterberg, M. Linvin, and M. Aldén, "Simultaneous laser-induced fluorescence and sub-Doppler polarization spectroscopy of the CH radical," *Optics Communications*, vol. 270, no. 2, pp. 347–352, 2007.

[58] Z. S. Li, M. Afzelius, J. Zetterberg, and M. Aldén, "Applications of a single-longitudinal-mode alexandrite laser for diagnostics of parameters of combustion interest," *Review of Scientific Instruments*, vol. 75, no. 10, pp. 3208–3215, 2004.

[59] G. Damköhler, "Der Einfluss der Turbulenz auf die Flammengeschwindigkeit in Gasgemischen (Influence of turbulence on the velocity of flames in gas mixtures)," *Zeitschrift für Elektrochemie und Angewandte Physikalische Chemie*, vol. 46, no. 11, pp. 601–626, 1940.

[60] R. Borghi, *On the structure and morphology of turbulent premixed flames*, pp. 117–138. Plenum Press, New York, 1985.

[61] A. C. Eckbreth, *Laser diagnostics for combustion temperature and species*. CRC, 1996.

[62] J. W. Daily, "Laser induced fluorescence spectroscopy in flames," *Progress in Energy and Combustion Science*, vol. 23, no. 2, pp. 133–199, 1997.

[63] J. Luque and D. R. Crosley, "Electronic transition moment and rotational transition probabilities in CH. II. $B^2\Sigma^- - X^2\Pi$ system," *Journal of Chemical Physics*, vol. 104, no. 11, pp. 3907–3913, 1996.

[64] N. L. Garland and D. R. Crosley, "Energy transfer processes in CH $A^2\Delta$ and $B^2\Sigma^-$ in an atmospheric pressure flame," *Applied Optics*, vol. 24, no. 23, pp. 4229–4237, 1985.

[65] J. Luque, R. J. H. Klein-Douwel, J. B. Jeffries, and D. R. Crosley, "Collisional processes near the CH $B^2\Sigma^- v' = 0, 1$ predissociation limit in laser-induced fluorescence flame diagnostics," *Applied Physics B: Lasers and Optics*, vol. 71, no. 1, pp. 85–94, 2000.

[66] G. Richmond, M. L. Costen, and K. G. McKendrick, "Collision-Partner Dependence of Energy Transfer between the CH $A^2\Delta$ and $B^2\Sigma^-$ States," *The Journal of Physical Chemistry A*, vol. 109, no. 4, pp. 542–553, 2005.

[67] E. F. van Dischoeck, "Photodissociation processes in the CH molecule," *The Journal of Chemical Physics*, vol. 86, no. 1, pp. 196–214, 1987.

[68] J. Luque and D. R. Crosley, "Electronic transition moment and rotational transition probabilities in CH. I. $A^2\Delta - X^2\Pi$ system," *Journal of Chemical Physics*, vol. 104, no. 6, pp. 2146–2155, 1996.

[69] P. F. Bernath, "The vibration-rotation spectrum of CH($X^2\Pi$)," *The Journal of Chemical Physics*, vol. 86, no. 9, pp. 4838–4842, 1987.

[70] A. Marshall, P. Venkateswaran, D. Noble, J. Seitzman, and T. Lieuwen, "Development and characterization of a variable turbulence generation system," *Experiments in Fluids*, vol. 51, no. 3, pp. 611–620, 2011.

[71] A. Melling, "Tracer particles and seeding for particle image velocimetry," *Measurement Science and Technology*, vol. 8, no. 1, pp. 1406–1416, 1997.

[72] B. Hemmerling, "Beam steering effects in turbulent high-pressure flames," in *Proceedings of SPIE*, vol. 3108, pp. 32–37, 1997.

[73] C. J. Dasch, "One-dimensional tomography: a comparison of abel, onion-peeling, and filtered backprojection methods," *Applied Optics*, vol. 31, no. 8, pp. 1146–1152, 1992.

[74] J. Luque and D. R. Crosley, *LIFBASE: Database and Spectral Simulation Program (Version 1.5)*. SRI International Report MP 99-009, 1999.

[75] N. L. Garland and D. R. Crosley, "Relative transition probability measurements in the $A-X$ and $B-X$ systems of CH," *Journal of Quantitative Spectroscopy and Radiative Transfer*, vol. 33, no. 6, pp. 591–595, 1985.

[76] C. J. Nokes, G. Gilbert, and R. J. Donovan, "Direct kinetic study of CH($A^2\Delta$)," *Chemical Physics Letters*, vol. 99, no. 5-6, pp. 491–493, 1983.

[77] F. L. Tabarés and A. G. U. na, "Electronic quenching of CH($A^2\Delta - X^2\Pi$) and OH($A^2\Sigma^+ - X^2\Pi$) by N_2 and O_2," *Journal of Photochemistry*, vol. 21, no. 4, pp. 281–289, 1983.

[78] T. A. Cool and P. J. H. Tjossem, "Direct observations of chemi-ionization in hydrocarbon flames enhanced by laser excited CH*($A^2\Delta$) and CH*($B^2\Sigma^-$)," *Chemical Physics Letters*, vol. 111, no. 1-2, pp. 82–88, 1984.

[79] C. J. Nokes and R. J. Donovan, "Time-resolved kinetic studies of electronically excited CH radicals. II. Quenching efficiencies for CH($A^2\Delta$)," *Chemical Physics*, vol. 90, no. 1-2, pp. 167–174, 1984.

[80] N. L. Garland and D. R. Crosley, "On the collisional quenching of electronically excited OH, NH and CH in flames," in *Symposium (International) on Combustion*, vol. 21, pp. 1693–1702, 1986.

[81] N. L. Garland and D. R. Crosley, "Collisional quenching of CH $A^2\Delta, v' = 0$ at 1300 K," *Chemical Physics Letters*, vol. 134, no. 2, pp. 189–194, 1987.

[82] P. Heinrich, R. D. Kenner, and F. Stuhl, "Collisional quenching at 300 K: $CH(A^2\Delta)$ by H_2O, NH_3 and other gases and $NH(A^3\Pi)$ by H_2O," *Chemical Physics Letters*, vol. 147, no. 6, pp. 575–580, 1988.

[83] K. J. Rensberger, M. J. Dyer, and R. A. Copeland, "Time-resolved $CH(A^2\Delta$ and $B^2\Sigma^-)$ laser-induced fluorescence in low pressure hydrocarbon flames," *Applied Optics*, vol. 27, no. 17, pp. 3679–3689, 1988.

[84] D. E. Heard, J. B. Jeffries, and D. R. Crosley, "Collisional quenching of $A^2\Sigma^+$ NO and $A^2\Delta$ CH in low pressure flames," *Chemical Physics Letters*, vol. 178, no. 5,6, pp. 533–537, 1991.

[85] R. D. Kenner, S. Pfannenberg, P. Heinrich, and F. Stuhl, "Electronic Quenching of $CH(A^2\Delta)$, $NH(A^3\Pi)$, $NH(c^1\Pi)$, and $PH(A^3\Pi)$ between 240 and 420 K," *The Journal of Physical Chemistry*, vol. 95, no. 17, pp. 6585–6593, 1991.

[86] C. Chen, X. Wang, S. Yu, Q. Lu, and X. Ma, "Collisional quenching of $CH(A^2\Delta)$ at 300 K by O_2, alkane, chloromethane and CS_2 molecules," *Chemical Physics Letters*, vol. 197, no. 3, pp. 286–291, 1992.

[87] J. L. Cooper and J. C. Whitehead, "Collisional Removal Rates for Electronically Excited CH Radicals $B^2\Sigma^-$ and $C^2\Sigma^+$," *Journal of the Chemical Society, Faraday Transactions*, vol. 88, no. 16, pp. 2323–2327, 1992.

[88] C. Chen, Q. Ran, S. Yu, and X. Ma, "Time-resolved kinetic studies on quenching of CH($A^2\Delta$ and $B^2\Sigma^-$) by (CX$_3$)$_2$CO, CF$_3$COOX, and CXCl$_3$ (X=H or D) and alkane molecules," *The Journal of Chemical Physics*, vol. 99, no. 2, pp. 1070–1075, 1993.

[89] C. Chen, Y. Sheng, S. Yu, and X. Ma, "Investigation of the collisional quenching of CH($A^2\Delta$ and $B^2\Sigma^-$) by Ar, O$_2$, CS$_2$, alcohol, and halomethane molecules," *The Journal of Chemical Physics*, vol. 101, no. 7, pp. 5727–5730, 1994.

[90] P. Heinrich and F. Stuhl, "Electronic Quenching of CH($A^2\Delta$) and NH($A^3\Pi$) between 300 and 950 K," *Chemical Physics*, vol. 199, no. 1, pp. 105–118, 1995.

[91] C. Chen, F. Wang, Y. Chen, and X. Ma, "Temperature effect on quenching of CH($A^2\Delta$)," *Chemical Physics*, vol. 230, no. 2–3, pp. 317–325, 1998.

[92] M. Tamura, P. A. Berg, J. E. Harrington, J. Luque, J. B. Jeffries, G. P. Smith, and D. R. Crosley, "Collisional Quenching of CH(A), OH(A), and NO(A) in Low Pressure Hydrocarbon Flames," *Combustion and Flame*, vol. 114, no. 3-4, pp. 502–514, 1998.

[93] C. Cerezo and M. Martin, "Rotational level dependence in the collisional removal of CH/D($A^2\Delta$)," *Journal of Photochemistry and Photobiology A: Chemistry*, vol. 134, no. 1–2, pp. 127–132, 2000.

[94] M. W. Renfro, K. K. Venkatesan, and N. M. Laurendeau, "Cross sections for quenching of CH $A^2\Delta, v' = 0$, by N$_2$ and H$_2$O from 1740 to 2160 K," in *Proceedings of the Combustion Institute*, vol. 29, pp. 2695–2702, 2002.

[95] C. J. Randall, C. Murray, and K. G. McKendrick, "State-specific collisional coupling of the CH $A^2\Delta$ and $B^2\Sigma^-$ states," *Physical Chemistry Chemical Physics*, vol. 2, no. 4, pp. 461–471, 2000.

[96] M. Zachwieja, "New Investigations of the $A^2\Delta - X^2\Pi$ Band System in the CH Radical and a New Reduction of the Vibration-Rotation Spectrum of CH from the ATMOS Spectra," *Journal of Molecular Spectroscopy*, vol. 170, no. 2, pp. 285–309, 1995.

[97] P. A. Berg, D. A. Hill, A. R. Noble, G. P. Smith, J. B. Jeffries, and D. R. Crosley, "Absolute CH Concentration Measurements in Low-Pressure Methane Flames: Comparisons with Model Results," *Combustion and Flame*, vol. 121, no. 1-2, pp. 223–235, 2000.

[98] H. Kobayashi, T. Tamura, K. Maruta, and T. Niioka, "Burning velocity of turbulent premixed flames in a high-pressure environment," in *Symposium (International) on Combustion*, vol. 26, pp. 389–396, 1996.

[99] C. K. Law, *Combustion Physics*. Cambridge University Press, 2006.

[100] S. H. Stårner and R. W. Bilger, "Joint measurements of velocity and scalars in turbulent diffusion flame with moderate swirl," in *Symposium (International) on Combustion*, vol. 21, pp. 1569–1577, 1986.

[101] H. Kobayashi, Y. Kawabata, and K. Maruta, "Experimental study on general correlation of turbulent burning velocity at high pressure," in *Symposium (International) on Combustion*, vol. 27, pp. 941–948, 1998.

[102] H. Kobayashi, "Experimental study of high-pressure turbulent premixed flames," *Experimental Thermal and Fluid Science*, vol. 26, no. 2, pp. 375–387, 2002.

[103] P. Griebel, P. Siewert, and P. Jansohn, "Flame characteristics of turbulent lean premixed methane/air flames at high pressure: Turbulent flame speed and flame brush thickness," in *Proceedings of the Combustion Institute*, vol. 31, pp. 3083–3090, 2007.

[104] H. Kobayashi, T. Nakashima, T. Tamura, K. Maruta, and T. Niioka, "Turbulence Measurements and Observations of Turbulent Premixed Flames at Elevated Pressures up to 3.0 MPa," *Combustion and Flame*, vol. 108, no. 1-2, pp. 104–117, 1997.